MODELING OF CURING PROCESS OF EARLY-AGE CONCRETE TO ASSESS BUILDABILITY OF 3D PRINTED CONCRETE STRUCTURES

A THESIS SUBMITTED TO
THE GRADUATE SCHOOL OF NATURAL AND APPLIED SCIENCES
OF
MIDDLE EAST TECHNICAL UNIVERSITY

BY

AMIRALI HASHEMZADEH

IN PARTIAL FULFILLMENT OF THE REQUIREMENTS
FOR
THE DEGREE OF MASTER OF SCIENCE
IN
MECHANICAL ENGINEERING

JANUARY 2023

Approval of the thesis:

MODELING OF CURING PROCESS OF EARLY-AGE CONCRETE TO ASSESS BUILDABILITY OF 3D PRINTED CONCRETE STRUCTURES

submitted by **AMIRALI HASHEMZADEH** in partial fulfillment of the requirements for the degree of **Master of Science in Mechanical Engineering Department, Middle East Technical University** by,

Prof. Dr. Halil Kalıpçılar
Dean, Graduate School of **Natural and Applied Sciences** _____

Prof. Dr. M. A. Sahir Arıkan
Head of Department, **Mechanical Engineering** _____

Assoc. Prof. Dr. Hüsnü Dal
Supervisor, **Mechanical Engineering, METU** _____

Examining Committee Members:

Assoc. Prof. Dr. Ulaş Yaman
Mechanical Engineering, METU _____

Assoc. Prof. Dr. Hüsnü Dal
Mechanical Engineering, METU _____

Assoc. Prof. Dr. Çağla Meral Akgül
Civil Engineering, METU _____

Assoc. Prof. Dr. Sezer Özerinç
Mechanical Engineering, METU _____

Assoc. Prof. Dr. Bahadır Alyavuz
Civil Engineering, Gazi University _____

Date:20.01.2023

I hereby declare that all information in this document has been obtained and presented in accordance with academic rules and ethical conduct. I also declare that, as required by these rules and conduct, I have fully cited and referenced all material and results that are not original to this work.

Name, Surname: Amirali Hashemzadeh

Signature :

ABSTRACT

MODELING OF CURING PROCESS OF EARLY-AGE CONCRETE TO ASSESS BUILDABILITY OF 3D PRINTED CONCRETE STRUCTURES

Hashemzadeh, Amirali
M.S., Department of Mechanical Engineering
Supervisor: Assoc. Prof. Dr. Hüsnü Dal

January 2023, 95 pages

This work presents a possible mathematical framework for capturing the buildability phenomenon in 3D printed concrete structures. Mathematical frameworks are proposed to describe the curing and hydration kinetics of 3D printed concrete structures in their fresh state. This scheme is subsequently incorporated into three concrete plasticity damage models. In the first model, a microplane-based Drucker-Prager (DP) plasticity damage model is studied and the mathematical formulations of the remaining two models are adopted from published sources. The performance and parameter calibration of age-dependent elasto-plastic-damage schemes are evaluated using experimental stress-strain data gathered from uni-axial unconfined compression tests, performed on concrete specimens of varying ages. In performing numerical simulations, the last optimized early-age scheme is utilized along with a framework, quantitatively incorporating the printing process and its associated components. On the basis of simulation results of 3D printed structures, the self-weight-induced deformations in the principal directions and the impacts of various printing parameters are assessed. Lastly, as a real-life application of the proposed scheme, numerical simulations are repeated on a 3D printed column geometry, performed in the İston Inc.

facility in Istanbul.

Keywords: Early-age concrete, 3D printed concrete, Buildability, Curing, Hydration, Microplane framework, Drucker-Prager plasticity, Damage.

ÖZ

3D BASKILI BETON YAPILARIN İNŞA EDİLEBİLİRLİĞİNİ DEĞERLENDİRMEK İÇİN ERKEN YAŞ BETONUN KÜRLENME SÜRECİNİN MODELLENMESİ

Hashemzadeh, Amirali
Yüksek Lisans, Makina Mühendisliği Bölümü
Tez Yöneticisi: Doç. Dr. Hüsnü Dal

Ocak 2023 , 95 sayfa

Bu çalışma, 3D baskılı beton yapılarda inşa edilebilirlik olgusunu yakalamak için olası bir matematiksel çerçeve sunar. 3D baskılı beton yapıların taze hallerinde kürlenme ve hidrasyon kinetiklerini açıklamak için matematiksel çerçeveler önerilmiştir. Bu şema daha sonra üç beton plastisite hasar modeline dahil edilmiştir. İlk modelde, mikrodüzlem tabanlı Drucker-Prager (DP) plastisite hasar modeli incelenmiş ve kalan iki modelin matematiksel formülasyonları yayınlanmış kaynaklardan uyarlanmıştır. Yaşa bağlı elasto-plastik-hasar şemalarının performansı ve parametre kalibrasyonu, farklı yaşlardaki beton numuneler üzerinde gerçekleştirilen tek eksenli serbest sıkıştırma testlerinden toplanan deneysel gerilim-gerinim verileri kullanılarak değerlendirilir. Sayısal simülasyonların gerçekleştirilmesinde, en son optimize edilmiş erken yaş şeması, baskı sürecini ve ilgili bileşenlerini kantitatif olarak içeren bir çerçeve ile birlikte kullanılır. 3D baskılı yapıların simülasyon sonuçlarına dayanarak, ana yönlerde öz ağırlık kaynaklı deformasyonlar ve çeşitli baskı parametrelerinin etkileri değerlendirilir. Son olarak, önerilen şemanın gerçek hayattaki bir uygulaması

olarak, İstanbul'daki İston Inc. tesisinde gerçekleştirilen 3D baskılı sütun geometrisi üzerinde sayısal simülasyonlar tekrarlanmıştır.

Anahtar Kelimeler: Erken yaş beton, 3D baskılı beton, İnşa edilebilirlik, Kürlenme, Hidrasyon, Mikrodüzlem çerçevesi, Drucker-Prager plastisitesi, Hasar.

To my parents:

Jafar Hashemzadeh, Roghieh Eftekhar.

ACKNOWLEDGMENTS

Initially, I want to appreciate my thesis advisor, Assoc. Prof. Dr. Hüsnü Dal, for providing me the opportunity to work on this research topic.

I would also want to thank the members of my jury panel, Assoc. Prof. Dr. Ulaş Yaman, Assoc. Prof. Dr. Çağla Meral Akgül, Assoc. Prof. Dr. Sezer Özerinç, and Assoc. Prof. Dr. Bahadır Alyavuz for their insightful comments that contributed to the improvement of my work.

I would like to acknowledge Tübitak for providing funding for the 3D concrete printing project (120N990) with special appreciation to the project leader, Assoc. Prof. Dr. Çağla Meral Akgül, who granted me the chance to join the team.

Attempting the research marathon for my master's degree has once again reminded me of the importance of my parents, who have been at my side throughout all stages of my life, and I would like to convey my deepest gratitude for all of their support.

In addition, I would like to express my heartfelt thanks to Suzan Akkad for being the best companion during the happy times, the best listener during the tough times, and the person to have observed the formation of my work from its inception to its conclusion.

Furthermore, I would like to thank Dr. Sepehr Seyyedian for his assistance and guidance throughout this endeavor.

Lastly, I would like to thank all my friends, especially my colleagues in the 3DPC project, for their endorsement during this journey, with special regard to Erman Tunçer for his assistance with the experimental aspects of my work.

TABLE OF CONTENTS

LIST OF TABLES

TABLES

LIST OF FIGURES

FIGURES

LIST OF ABBREVIATIONS

3D	Three Dimensional
AOT	Angle of Twist
CAD	Computer-aided Design
CDI	Clausius–Duhem Inequality
CDM	Continuum Damage Mechanics
CRV	Constant Rotational Velocity
CUCT	Confined Uni-axial Compression Test
DP	Drucker-Prager
GWP	Global Warming Potential
HFE	Helmholtz Free Energy
LVDT	Linear Variable Differential Transformer
N-T	Normal-Tangential
ODE	Ordinary Differential Equation
OPC	Ordinary Portland Cement
PDE	Partial Differential Equation
SBA	Selective Binder Activation
UUCT	Unconfined Uni-axial Compression Test
V-D	Volumetric-Deviatoric
V-D-T	Volumetric-Deviatoric-Tangential

CHAPTER 1

INTRODUCTION

1.1 Motivation and Problem Definition

Due to the extensive use of cement in the construction of various structures, the cement industry has become one of the major contributors to industrial pollution. The scientific community of civil engineers has made efforts on multiple fronts to mitigate the negative effects of cementitious materials, including designing and optimizing composite mixtures with one or more constituents replaced with waste materials, or sustainable alternatives (with similar, and in some cases better mechanical performance than their unsustainable counterparts), and structural optimization to reduce the amount of used materials. In the case of concrete, additive manufacturing has demonstrated that it has the potential to be one of the solutions for the environmental concerns revolving around concrete structures, due to its characteristics, which include accurate material deposition, less amount of waste production, reduced material use, reduced need for human labor, formwork-free nature, and the ability to produce complex shapes.

Structures made from 3D printing should have acceptable performance both in fresh or hardened states. In a hardened state, the mechanical behavior of 3D printed constructions should be adequate under various internal or external loads. However, in order for a printed concrete structure to achieve its hardened phase, it must be capable of sustaining its own weight within acceptable deformation ranges, so that the end product is not excessively deformed and is close enough to the original design. This characteristic of 3D printed concrete structures is referred to as "buildability." Recently, various attempts have been made to capture this trait using mathematical

frameworks involving the rheological properties of the utilized mixtures. However, only a small number of research include rigorous solid mechanical treatment of buildability.

This study seeks to provide a feasible solid mechanical capture of the buildability phenomenon in 3D printed concrete buildings in their fresh form.

1.2 Literature review

The first attempt to use cementitious materials in additive manufacturing procedures was conducted by J. Pegna in 1997 [18]. In recent years, additive manufacturing of concrete has gained widespread attention due to advantages such as reduced labor force and construction time, cost efficiency, and versatile design options [11]. In a study conducted by S. El-Sayegh et al. [4], the advantages of utilizing concrete additive manufacturing technologies are categorized into two main groups: a) constructability and b) sustainability (represented in Figure 1.1). The constructability of 3D printed concrete structures is deemed superior due to lower production expenses, less preparation time, extensive design leeway, fewer supply-chain effects, and greater efficiency. With regards to sustainability, reasons such as lower waste production, better integration of eco-friendly buildings, and lower formwork requirement make additive manufacturing of concrete a suitable candidate for the future of the construction industry.

According to S.A. Khan et al. [19], cement is considered the major key in producing greenhouse gas emissions in ordinary portland cement (OPC) concrete, making sustainable replacements for cement of crucial importance. Compared to traditional concrete, mixtures used in the additive manufacturing of concrete contain higher cement, binder, and fine aggregate contents [20]. Figure 1.2 represents a comparative scheme of typical mixture contents in traditional and 3D printed concrete applications. Hence, it is essential to look for more sustainable mixtures in 3D printing applications for the reasons outlined above.

The sustainability of additively manufactured concrete can be assessed in terms of its costs and environmental effects [21].

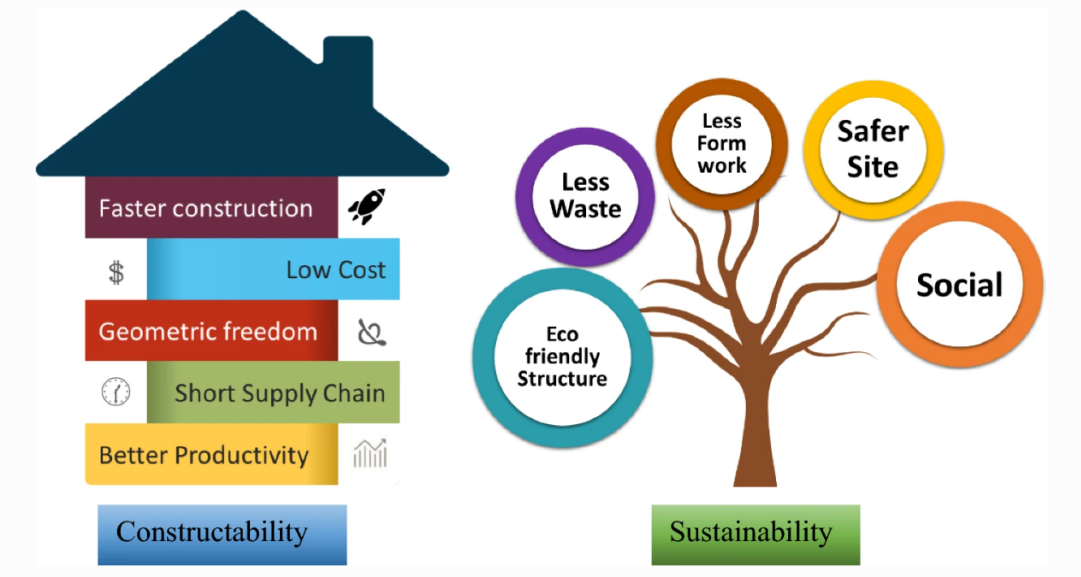

Figure 1.1: Benefits of using additive manufacturing of concrete as categorized in [4].

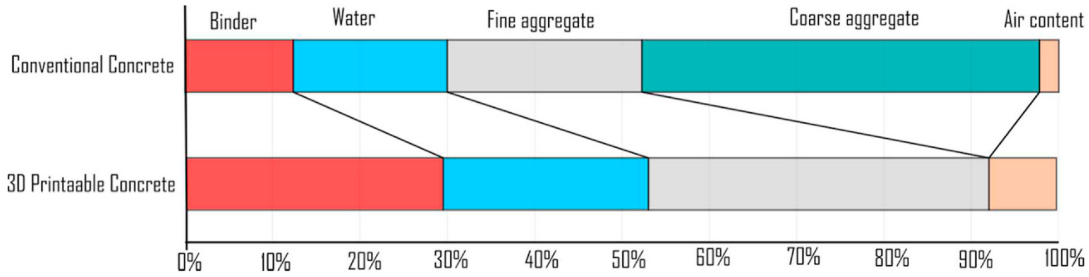

Figure 1.2: A schematic comparison between the composite contents of traditional and 3D-printed concrete [5].

According to research by S. Muthukrishnan et al. [22], material costs resulting from high cement and admixture content and low amounts of aggregates larger than 2 millimeters accounted for 70% of the overall price of 3D printed concrete. Consequently, lowering the cement percentage of 3D printable mixtures is also economically favourable. In a study conducted by M. Valipour et al. [23], the possibility of using zeolite as an environmentally friendly alternative for cement was considered. It was demonstrated that 10%, 20%, and 30% of overall substitution of cement diminished global warming potential by 60.3%, 69.7%, and 64.3%, respectively. Furthermore, for the 10% and 20% zeolite substitution instances, respectively, comparative increases in compressive strength of 10% and 20% were recorded. G. Bai et al. [24]

studied the effect of applying less-used and waste solids as aggregates in the additive manufacturing of concrete. The study found that using recycled aggregates in the mixture improved the adhesion between layers. This was attributed to the interlayer roughening, which caused an increase in the contact area of the adjacent layers. D. Dey et al. [20] conducted a review on the usage of industrial waste material in 3D printing mix design. Within the study, it was concluded that the usage of supplementary cementitious materials renders conventional concrete more sustainable and durable. It was also concluded that the use of industrial waste can greatly affect the rheological characteristics of 3D printed concrete in terms of buildability and extrudability. A.U. Rehman et al. [25] conducted a study on utilizing an incinerated form of municipal solid waste in concrete additive manufacturing. The study reported lower setting time, increased yield stress, improved buildability, and better layer adhesion as some of the beneficial results.

To assess the environmental impacts of additive manufacturing of concrete, M. Mohammad et al. [26] performed a life-cycle study on the environmental impacts of 3D printed concrete with and without reinforcement. It was indicated that 3D printed concrete without reinforcement, in which sand was supplanted with expanded perlite diminished the global warming, acidification, eutrophication, smog formation potentials, and fossil fuel depletion factor. In another study, M.R.M. Saade et al. [6] conducted a life cycle assessment review on 52 papers, in which the vast majority of the studies reached the conclusion that concrete additive manufacturing is more sustainable. However, it was found that 3D printing works best for structures with more complicated designs and needs to be made more energy and emission efficient. Finally, it was demonstrated that the global warming potential for material loads was more significant in additive manufacturing processes of construction-related 3D printed products, than for process loads as shown by the red dots in Figure 1.3. Other studies have also underlined the significance of material-related burdens on the environmental implications of 3D printed structures [21, 27], and the usage of reusable and recyclable components as printing materials has been advised [6]. S. Liu et al. [9] performed a life cycle assessment of the environmental effects of using OPC and geopolymer in traditional casting and 3D printing of concrete. It was determined that, despite incorporating 20% industrial waste due to their higher activator content,

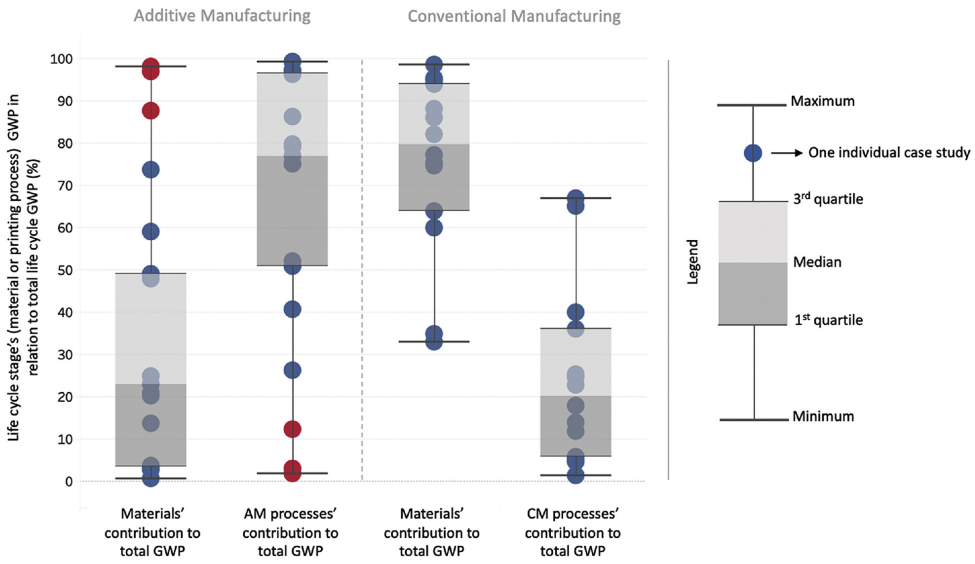

Figure 1.3: Material- and process-related environmental impacts compared to the total life-cycle GWP [6].

geopolymers did not outperform OPC. M. K. Mohan et al. [21] performed an assessment of 3D printable concrete mixtures, using environmental cost/impact indicators, and suggested that the environmental effects of 3D printed structures could be diminished by 1) integrating calcium sulfoaluminate limestone and portland cement blast furnace slag binder systems, or 2) incorporating more natural and reused coarse aggregates (if not compromised by the transportation costs). Other studies have also suggested using recycled coarse aggregates in traditional or additive manufacturing applications. According to C. Knoeri et al. [28], substituting natural concrete with recycled concrete can reduce the environmental impact of concrete by 70%. Y. Han et al. [27] mention that the environmental impact of 3D printing applications is proportional to the cement concentration of the employed mixtures and inversely proportional to the coarse aggregate content. According to a number of studies, caution should be taken while using recycled aggregates. As per S. Marinković et al. [29], not all recycled concretes have the potential to be environmentally friendly, and the amount of cement used, type of concrete, and distance traveled are among the variables that must be examined. Transportation-related environmental concerns should not be neglected, especially when huge volumes are transported [30]. In addition to the effects of the mixture contents, the complexity and volume of manufacturing have

a significant role in determining the environmental impact of 3D printed concrete. In the study performed by Y. Han et al. [27], it was revealed that geometric sophistication had almost negligible influence on the environmental impact of the 3D printing process. Also, I. Agustí-Juan et al. [7] compared the construction of walls using digital and conventional fabrication methods, altering the wall's geometrical complexity; they reported the same finding regarding the minimal effect of geometrical complexity on the environmental implications of 3D printed concrete. The reported results of [7] were used by G. D. Schutter et al. to create Figure 1.4, which clearly shows the advantages of using additive manufacturing over traditional methods in producing geometrically intricate structures.

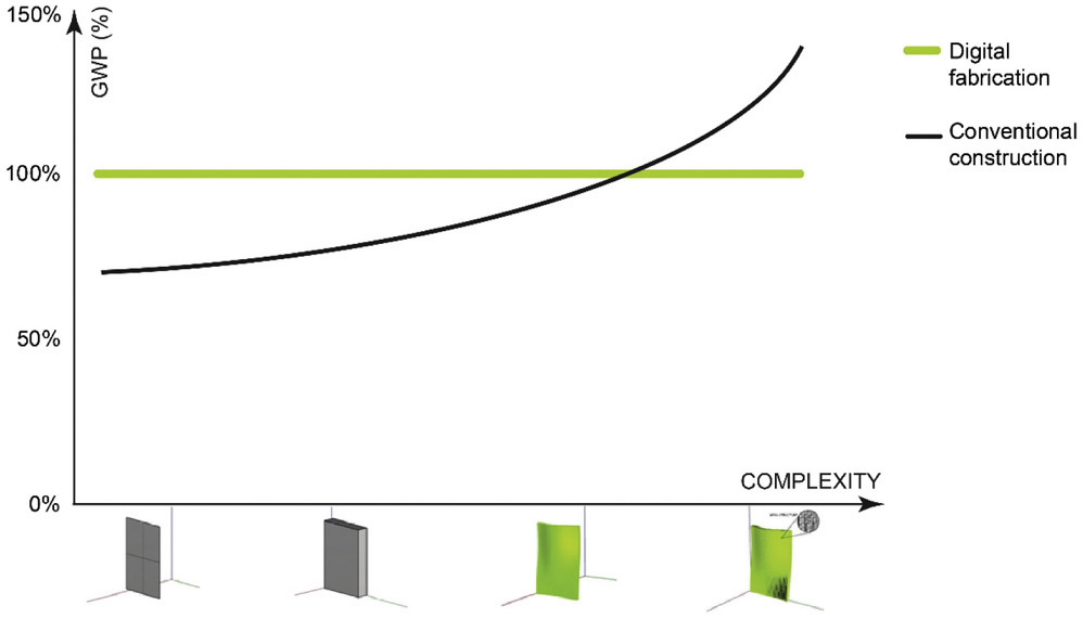

Figure 1.4: Comparing the global warming potential of conventional and digital concrete manufacturing techniques as the geometric complexity of the created structures increases [7, 8].

In the study conducted by S. Liu et al. [9], it was determined that the environmental benefits of 3D printing of concrete can be maximized by employing it to create non-repetitive, free-form, and more intricate constructions and by reusing formworks during the production process. In the same study, Figure 1.5 was proposed as a comparative scheme involving formwork reuse, geometrical complexity, and environmental benefits of 3D printing and casting processes; the Figure also highlights the clear

environmental advantages of additive manufacturing methods in the construction of more complex structures.

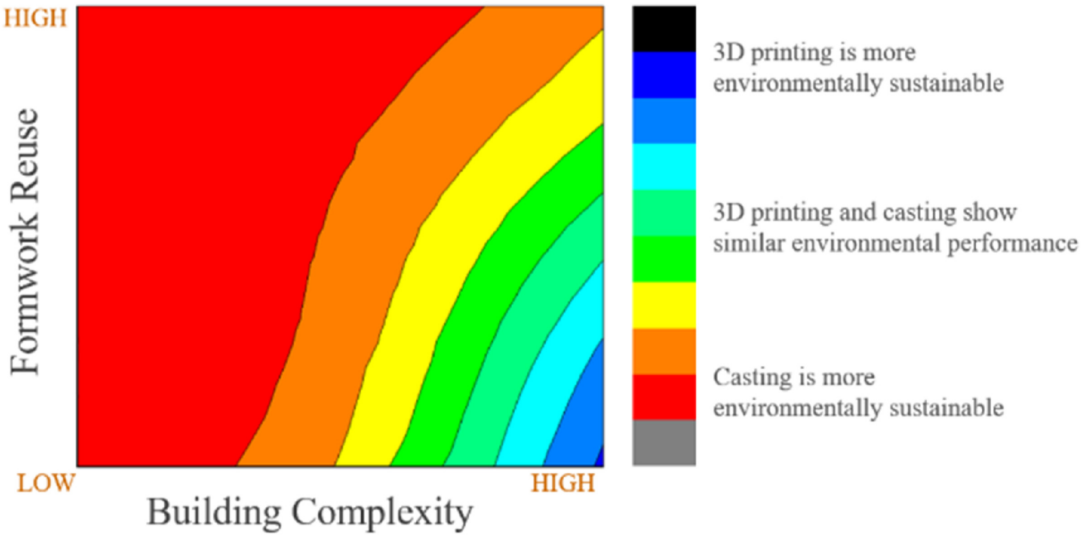

Figure 1.5: A comparison of the environmental benefits of 3D printing versus conventional casting, taking into account form-work reuse and geometrical complexity aspects [9].

According to the studies in literature, additive manufacturing of concrete is a more appropriate approach when the production volume is relatively small. Y. Weng et al. [31] conducted a life cycle analysis on the manufacture of a concrete bathroom using conventional (precast) and 3D printing techniques. The study revealed that the 3D printing production process led to reductions of 25.4%, 85.9%, 87.1%, and 26.2% in total cost, CO_2 emissions, energy usage, and total weight, respectively, and an increase in overall efficiency. When additive/subtractive manufacturing, traditional mold casting techniques were all taken into account in singular and mass production of a 4-meter-long pillar, Muñoz et al. [10] determined that for a single production, 3D printing had a significantly better outcome in terms of environmental assessments. As shown in Figure 1.6, the specified procedures did not significantly differ in the case of mass production.

The energy consumption associated with this technique should also be taken into consideration, even in the small-scale fabrication of 3D printed concrete structures. In the investigations conducted by J. Faludi et al. [32] and F. Cerdas et al. [33], it was

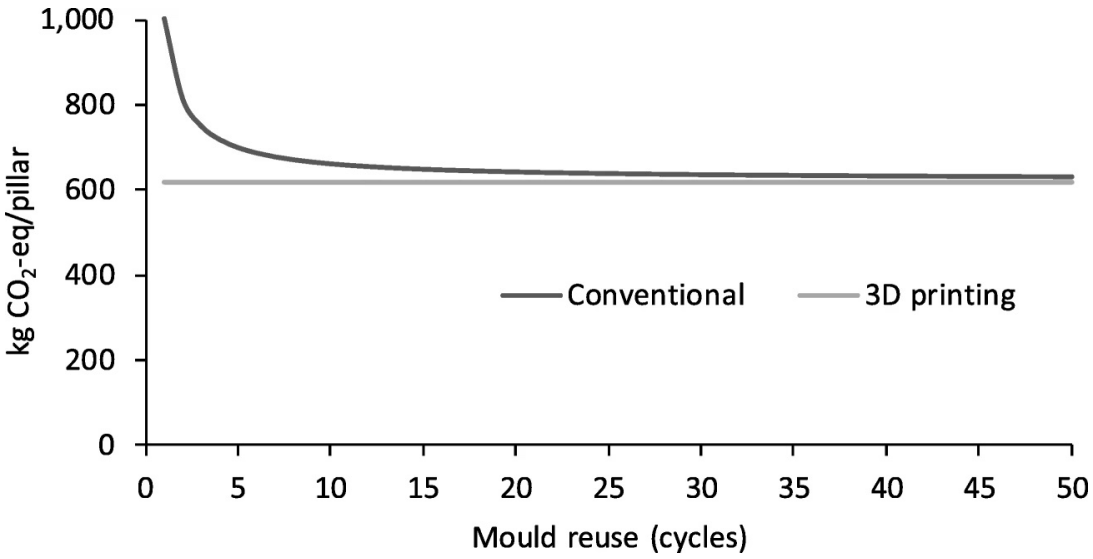

Figure 1.6: Environmental impacts of mold reuse, while making concrete structures using traditional and 3D printing methods [10].

discovered that the energy required for small-scale 3D printing of concrete outweighs the environmental benefits.

Printing accuracy and suitability of concrete additive manufacturing in producing geometrically intricate structures bring additional benefits that are considered in environmental assessments of other studies. For instance, N. Labonatte et al. [34, 35] stated that additive manufacturing of concrete structures has the capability to substantially cut material consumption due to its capacity to construct topologically optimized, geometrically complex, and multifunctional structures. Furthermore, I. Agustí-Juan et al. [7] noted that for larger structural members, additively manufactured parts have a lesser environmental impact when compared to conventional production methods. G. De Schutter et al. [8] came to the conclusion that the best way to adapt 3D concrete printing technology to the environment is to make pieces that use both structural optimization and functional hybridization (Figure 1.7). In addition, the study indicated that the use of high-performance concrete, which reduces the requirement for coarse particles, in conjunction with structural optimization in 3D printing of concrete is an effective environmentally friendly technique. Similar results were also reported in the study conducted by I. Agustí-Juan et al. [36]. They determined that 3D printing of structurally optimized parts decreased environmental

impacts by 50% and advocated integrating the most environmentally costly functionalities (not all) in conventional use into functionally hybridized 3D printed parts for the best environmental benefits.

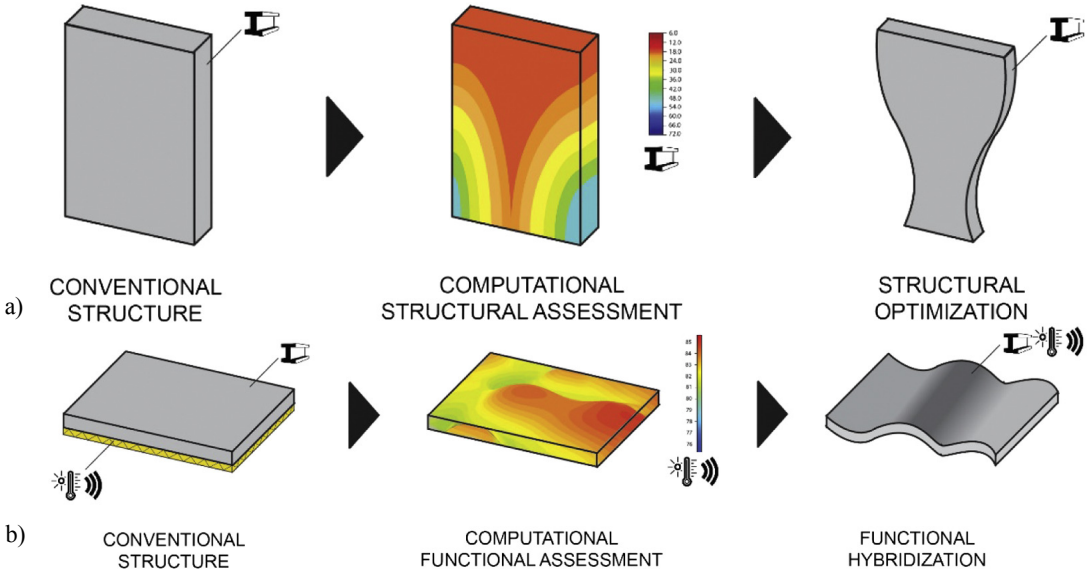

Figure 1.7: a) Structural optimization and b) functional hybridization [8].

Additionally, optimization of the printing path can improve environmental effects. According to the study conducted by K. Kuzmenko et al. [37], optimizing the printing path reduced environmental consequences by 15%. A six-axis robot was employed to complete the printing along the optimized path, highlighting the significance of the means applied in the 3D printing of concrete.

Selective binder activation (SBA), contour crafting, D-Shape methods, concrete printing, and selective paste intrusion are in common use in real-life applications, among various possible additive manufacturing techniques [4].

The contour crafting method is considered the first additive manufacturing approach for onsite tailored building fabrication and was initially developed by B. Khoshnevis et al. in 2006 [38]; this method entails the extrusion of concrete using a gantry system. The shape of the printed concrete layer is corrected using trowels that are connected to the system nozzle [39]. The advantages of contour crafting include a greater surface quality of the end product, a faster production rate, and a broader selection of appropriate materials [40]. Nonetheless, there are disadvantages associated with this

method, such as the fact that only vertical extrusions are possible, production is difficult, layer-wise interactions are weakened, and the mechanical performance of the printed parts is subpar [41]. Figure 1.8 contains a representation of a sample product prepared via the contour crafting additive manufacturing technique, as well as its typical printing set-up.

a) 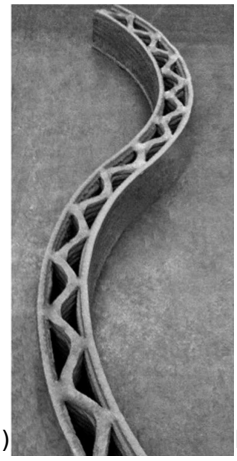 b) 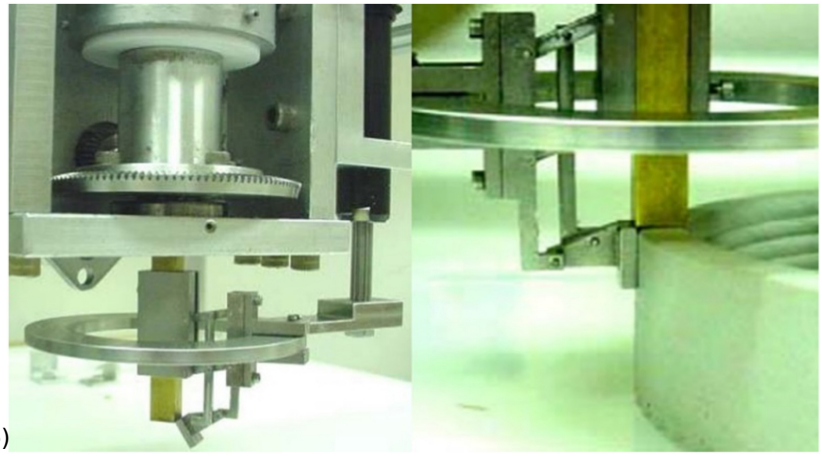

Figure 1.8: a) A structure printed by contour crafting [11] b) A schematic of the apparatus used for contour crafting [12].

D-shape printing is a sub-type of the SBA method for particle-bed 3D printing [13]. In the SBA method, fine aggregates are mixed with a binder (usually cement) to form the particle bed. In the second step, the water-admixture solution is sprayed on the particle bed yielding local activation of cement. [13, 42]. Figure 1.9 contains a representation of a sample product produced via the D-shape additive manufacturing technique, as well as its typical printing set-up.

a)  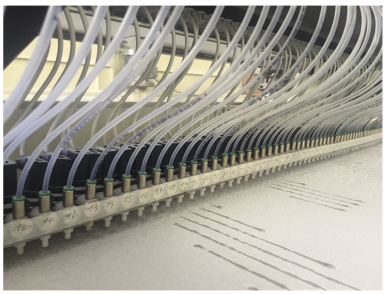 b) 

Figure 1.9: a) A schematic of the apparatus used for D-shape printing [13] b) A structure printed by D-shape printing [13].

Unlike the D-shape method, which is a dry printing process, concrete printing is a wet printing procedure, in which a high-performance-type concrete, in the form of mortar, is utilized as the printing material [4, 11]. In this method the accuracy of the printed material is smaller compared to the D-shape printing, however, it brings more leeway in the designing of interior and exterior components. The cleaning and maintenance requirements attributed to the pumping and extrusions systems in contour-crafting and concrete printing techniques are considered as drawbacks for these techniques [11]. Also, the strength of the printed result in the concrete printing method is comparatively higher than those produced by the contour crafting method [11]. Pumpability and buildability are two determining factors in the concrete printing additive manufacturing technique and they are directly affected by the rheological characteristics of the used mix, and the advancement of its elastic properties with time [14]. The mix design of the used material in concrete printing should render sufficient interlayer bonding so that the printing of further layers is possible without unacceptable deformation and simultaneously, it should be extrudable enough for it to be possible to be printed [15]. Figure 1.10 depicts the utilization of two mobile robotic arms in the concrete printing mehtod. Also exhibited are two printed results for a structural component and a full-scale villa suit.

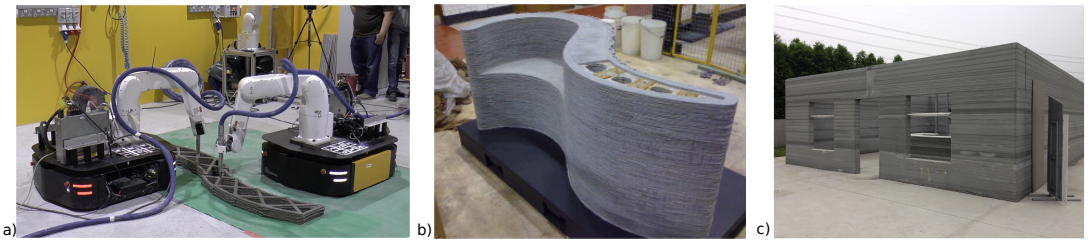

Figure 1.10: a) The use of two mobile robots in construction of a 3D printed concrete structure [14] b) A structural component built entirely via concrete printing in [11] c) A villa suit printed by WinSun through concrete printing additive manufacturing [15].

Among various introduced additive manufacturing approaches [43], layered-wise extrusion of concrete has proven to be the most feasible method in large-scale housing constructions [44], which does not require any formwork. The prominent feature of formwork-free layered concrete extrusion is the fresh-state concrete printability.

Printability of concrete is considered in respect of its buildability, and extrudability [45]. Extrudability refers to the capability of fresh-state concrete to flow continuously from a hopper to the nozzle of the printing head [45, 46]. While the extrusion procedure is in process, homogeneity of concrete flow and absence of cracks, blockage, or segregation is crucial [45, 47]. Buildability is the property of early-age state concrete which concerns the ability of fresh concrete to uphold self-weight loads [48, 49], the weight of the layers to be further printed [44], or induced loads during the printing process [50]. Direct and indirect methods are in common use in analyzing the buildability property of concrete [44]. Direct methods entail printing a predetermined geometry (usually a hollow cylinder [1] or a straight wall [51]). The printed structure can then be studied using one of two methods: 1) the total number of printed layers is predetermined and the total deformation is measured, or 2) the printing process continues until failure and the total number of printed layers is then counted [44]. In the indirect methods, either the rheological properties of the mix or solid mechanical modeling results are the basis for analyzing the buildability of concrete at early-age state [52]. The minimum necessary shear stress for the material to flow is defined as the static yield stress and its time-evolution is considered in the indirect methods of buildability modeling [52]. In considering the rheological characteristics, early-age concrete is assumed to be a non-Newtonian fluid of Bingham plastic-type [52, 51], where the time-evolution of the initial yield stress is based on the particularly chosen model. N. Roussel [53] considered a linear time evolution law for the development of initial yield stress, based on the results from rheometry tests, conducted over the resting time of the sample. The proportionality constant was named "structuration rate," which refers to the rate of increase of the initial yield stress over the resting period of an early-age sample [45, 53]. A. Perrot et al. [54] proposed formulations to calculate the structuration rate and the yield stress evolution of concrete and mortar mixes, with or without fibers, in terms of their corresponding values in cement paste state, volume dense packing fraction (ϕ_s), and random packing fraction (ϕ_{RLP}). In a later study, A. Perrot et al. [55] suggested an exponential formulation for the time evolution of the initial yield stress, asymptotically approaching the linear model of [53] as its limiting case. There have been few studies on the solid mechanical modeling of the early-age concrete that aimed at capturing its elastoplastic behavior [52], in which the material failure was categorized as either due to elastic buckling or plastic collapse [44, 56, 52].

A.S.J. Suiker [56] considered the sensitivity of the failure modes regarding the free, simply-supported, and fully clamped walls printed with linear or exponentially decaying curing kinetics. It was shown that simply-supported and fully-clamped walls render the lower and upper bounds of the wall buckling lengths, respectively. R.J.M. Wolfs et al. [1] considered the Mohr-Coulomb criterion for describing the yield stress. In this formulation, the cohesion parameter (C), the angle of internal friction (ϕ), and the modulus of elasticity were considered as functions of time, and their values were fitted to the experimental data. In [51], a DP-type plastic yielding criterion was utilized; the study assumed an improved Duncan-Chang [57] type stress-strain relation and used the DP yield criterion provided in ABAQUS 6.14 [58] for numerical simulations; the parameters of this model were related to the two experimentally measured parameters of the Mohr-Coulomb criterion using the formulations in [58, 51].

Various studies have proposed experimental procedures to validate or modify the used models in the indirect assessment of buildability and to obtain their relevant parameters. Common approaches include the uni-axial compression test [44, 59, 60], the constant rotational velocity (CRV) rheometry test [59, 44], and the triaxial compression test [61]. Unconfined uni-axial compression tests (UUCT) were conducted on cast samples in a displacement-controlled fashion to obtain the stress-strain behavior [44, 1, 59]. I. Ivanova et al. [44] proposed a new experimental procedure called the "Confined uni-axial Compression Test" (CUCT), where uni-axial compression tests were conducted on samples cut from layered printed specimens. Other experimental methods include penetration test [62], squeeze flow test [60, 62], and ultrasonic wave transmission tests [63, 64]. To determine the cohesion and angle of internal friction parameters of the Mohr-Coulomb yield criterion, R.J.M. Wolfs et al. [1] customized a direct shear test; the tests were repeated for three normal loads on cylindrical specimens.

Within the scope of this study, a DP-type microplane plasticity damage model will be utilized to describe the elastoplastic behavior of early-age concrete. Microplane framework for constitutive modeling of various materials was first introduced in 1983 by Z. Bažant & B. Oh [65]. The theory involves formulating the material constitutive behavior on tangent planes with arbitrary orientations and later, integrating the obtained plane-level responses to yield the overall behavior at the point of interest [66].

The method was initially developed as an approach for the constitutive modeling of quasi-brittle materials like concrete, and later, it was applied to other materials such as soil [67], shape memory alloys [68], and rocks [69]. Starting from a definition of a mass-specific Helmholtz free energy (HFE) functional, I. Carol et al. [66] derived a thermodynamically consistent formulation of the microplane framework. In [70], the elasticity, plasticity, and damage constitutive formulations were integrated into the microplane theory, with a normal-tangential-volumetric decomposition of the plane strains. E. Kuhl & E. Ramm [71] conducted a comparative study on integrating elastoplastic-damage formulations into the microplane theory for cohesive frictional materials in the effective stress space. M. Leukart & E. Ramm [72] integrated different definitions of energy equivalent strains and damage loading functions into the microplane theory. Due to the mesh sensitivity of continuum plasticity damage models, an implicit gradient regularization scheme was applied to microplane damage models in [3]. The implicit gradient enhancement scheme was applied for modeling softening plasticity of concrete in the small-strain setting [73] and in the large-strain setting [2]. In continuum damage-plasticity models, the effect of the damage parameter is enacted on the undamaged material stiffness; however, in [73] and [2], the effect of damage is considered only in the yield stress in plastic hardening.

In this study, we will consider a 1^{st} degree ODE model to describe the concrete curing in the post-printing regime. This approach was used in other studies regarding polymeric materials. In [74], the curing kinematics driving the vulcanization process of rubber was described using a 1^{st} degree ODE in terms of the "state of cure" variable. The paper considered the curing of rubber from an uncured state, modeled in a sense proposed in [75], to a cured state, modeled to be a generalized Maxwell branch. The present study considers the "degree of cure" parameter as a quantified representation of the progression of the aging process. It will be integrated into the microplane plasticity damage model to describe the evolution of material properties used in buildability predictions of Early-age concrete.

1.3 The Outline of the thesis

In **chapter one**, an overview of recent scientific literature regarding additive manufacturing of concrete is provided, including its economic and environmental impacts, its common practices, materials used in widely accepted printable mixes, modeling approaches, experimental testing procedures, and the circumstances in which it is deemed superior (and inferior) to traditional casting methods.

Chapter two lays forth the theoretical underpinnings of plasticity damage models, which are used in the early-age framework. As the first model, the theoretical foundations of a microplane DP plasticity damage model in a consistent thermodynamic context are laid out. Also provided is the mathematical structure of two additional concrete plasticity damage models taken from the scientific literature. The second scheme is a plasticity damage model that uses empirical formulations for plasticity and damage, and the last approach is a gradient-enhance microplane DP plasticity damage model.

The **third chapter** begins with a description of the apparatus used to conduct a series of unconfined uni-axial compressive tests and then continues with an in-depth analysis of the resulting data (with the assumptions and precautions taken in the procedure). Moreover, age-dependent mathematical frameworks for stress-strain behavior are proposed by coupling curing and hydration kinetics to the plasticity and damage models from the second chapter. For further numerical simulations of 3D printed structures, the gradient-enhanced microplane DP plasticity damage model, coupled with curing and hydration kinetics, is used. Also, a mathematical model is developed to account for the printing process and its associated parameters. Numerical simulations are performed for various geometries, and the effects of various parameters on the self-weight-induced deformations in the principal directions are taken into account. In the final step, numerical simulations are performed for a 3D printed column geometry produced at the Iston Inc. firm in Istanbul.

Lastly, in **chapter four** synopsis of the findings of this work and some suggestions for future work in this research area are presented.

CHAPTER 2

THEORETICAL FRAMEWORK

Within the scope of this thesis, three plasticity damage models for hardened concrete will be implemented with a mathematical treatment of the hydration and curing mechanisms in order to characterize the early-age behavior of concrete. The first model is based on a modification of the microplane DP plasticity damage model proposed by I. Zreid & M. Kaliske [73]. The other models had formerly been established by D. Feng et al. [17], and I. Zreid & M. Kaliske [2].

2.1 Plasticity damage model based on microplane framework

2.1.1 Microplane kinematics

The basic idea in the microplane theory is to describe constitutive laws within a plane of arbitrary direction and then integrate it over all possible orientations leading to the overall response of a material point, where normal plane vectors uniquely determine the planes. In the first step, quantities at a material point are projected onto planes of interest through plane normal vectors yielding their plane-level counterparts. If the quantity in consideration is the macroscopic strain or stress, the projection is known as "kinematic" or "static" constraint, respectively.

Projection of the stress and strain tensors through plane normal ($\boldsymbol{n}$) vector leads to the stress and strain vectors on those planes, represented by $\boldsymbol{t_\epsilon}$ and $\boldsymbol{t_\sigma}$ in equation (2.1):

$$\boldsymbol{t_\epsilon} = \boldsymbol{\epsilon} \cdot \boldsymbol{n}, \quad \text{and} \quad \boldsymbol{t_\sigma} = \boldsymbol{\sigma} \cdot \boldsymbol{n}. \tag{2.1}$$

Various decompositions of the projected stress and strain vectors are possible. Two common methods include the normal-tangential (N-T) split [76] and the volumetric-

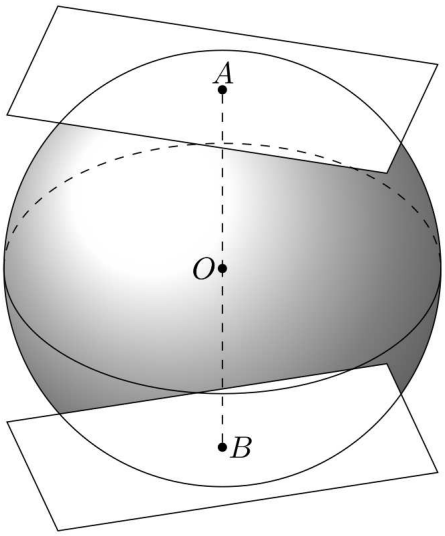

Figure 2.1: Representation of tangent planes to a unit sphere, surrounding the material point of interest.

deviatoric-tangential (V-D-T) split [77, 71]. The two splitting methods were compared in [71], and it was concluded that although the N-T method fully determines plane-level elastic constants in the normal and tangential directions, it only covers the Poisson's ratio in the range of $-1 \leq \nu \leq 0.25$. The V-D-T split, on the other hand, leads to non-unique elastic constants in the deviatoric and tangential directions; however, it can cover the full range of the Poisson's ratio $-1 \leq \nu \leq 0.5$. Neglecting the tangential component of the V-D-T split, M. Leukert & E. Ramm [72] proposed a different splitting format known as the volumetric-deviatoric (V-D) split. This study uses the kinematic constraint with the V-D split to describe the plane-level material constitutive behavior.

In Figure 2.2.a, the projected strain vector can be decomposed as:

$$\boldsymbol{t}_{\boldsymbol{\epsilon}} = \epsilon_V \boldsymbol{n} + \boldsymbol{\epsilon}_D. \tag{2.2}$$

In equation (2.2), ϵ_V (a scalar quantity) and $\boldsymbol{\epsilon}_D$ (a vector quantity) represent plane-level volumetric and deviatoric strain components, respectively. To obtain ϵ_V and $\boldsymbol{\epsilon}_D$, first, the macroscopic strain tensor is additively decomposed into volumetric and deviatoric parts:

$$\boldsymbol{\epsilon} := \boldsymbol{\epsilon}_{dev} + \boldsymbol{\epsilon}_{vol}. \tag{2.3}$$

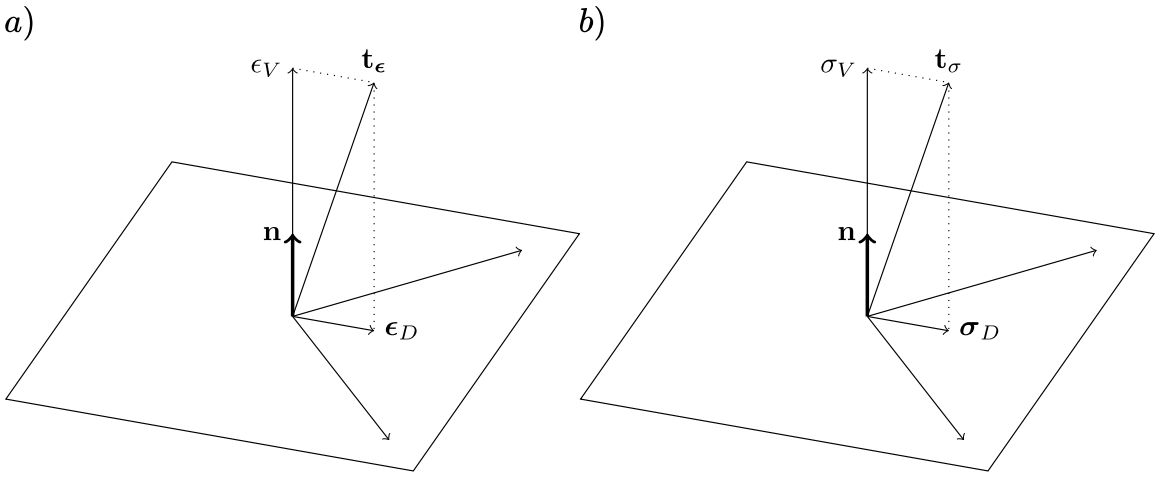

Figure 2.2: V-D split considered for a) kinematic, and b) static constraints.

The volumetric and deviatoric components in equation (2.3) are defined in terms of the macroscopic strain according to:

$$\boldsymbol{\epsilon}_{vol} := \frac{1}{3}\left[\boldsymbol{\epsilon} : \mathbf{1}\right]\mathbf{1}, \quad \text{and} \quad \boldsymbol{\epsilon}_{dev} := \boldsymbol{\epsilon} - \frac{1}{3}\left[\boldsymbol{\epsilon} : \mathbf{1}\right]\mathbf{1}. \tag{2.4}$$

Substitution of the definitions in equations (2.3) and (2.4) back into equation (2.1) yields an alternative definition for $\boldsymbol{t}_{\boldsymbol{\epsilon}}$:

$$\boldsymbol{t}_{\boldsymbol{\epsilon}} = \boldsymbol{\epsilon} \cdot \boldsymbol{n} = (\boldsymbol{\epsilon}_{vol} + \boldsymbol{\epsilon}_{dev}) \cdot \boldsymbol{n} = \frac{1}{3}\left[\boldsymbol{\epsilon} : \mathbf{1}\right]\boldsymbol{n} + \boldsymbol{\epsilon}_{dev} \cdot \boldsymbol{n}. \tag{2.5}$$

By comparing equations (2.2) and (2.5), to relate the V-D microplane strain components to the macroscopic strain, a 2^{nd} order volumetric projection tensor $\mathbf{V}$ and a 3^{rd} order deviatoric projection tensor $\overline{\overset{3}{\mathbf{Dev}}}$ are defined in terms of the plane normal $\mathbf{n}$ and the 2^{nd} order identity tensor $\mathbf{1}$. These tensors operate on the macroscopic strain tensor and render the plane-level volumetric and deviatoric strain components:

$$\begin{aligned} \boldsymbol{V} &:= \frac{1}{3}\mathbf{1}, \quad \text{and} \quad \overline{\overset{3}{\mathbf{Dev}}} := \boldsymbol{n} \cdot \mathbb{I}^{sym} - \frac{1}{3}\boldsymbol{n} \cdot \mathbf{1} \otimes \mathbf{1}, \\ \epsilon_V &= \boldsymbol{V} : \boldsymbol{\epsilon}, \quad \text{and} \quad \boldsymbol{\epsilon}_D = \overline{\overset{3}{\mathbf{Dev}}} : \boldsymbol{\epsilon}. \end{aligned} \tag{2.6}$$

In equation (2.6), $\mathbb{I}$ refers to the 4^{th} order identity tensor and its symmetric part defined as $\mathbb{I}^{sym} = \frac{1}{2}\left[\delta_{ik}\delta_{jl} + \delta_{il}\delta_{jk}\right]$. To be able to use the microplane theory to formulate material behavior in a thermodynamically consistent fashion, I. Carol et al. [66] proposed the existence of a plane-level HFE functional Ψ_{Ω}^{mic}, such that the macro-

scopic free energy can be obtained from integrating Ψ_Ω^{mic} over all planes:

$$\begin{aligned} \Psi_\Omega^{mic} &:= \bar{\Psi}_\Omega^{mic}\left(\boldsymbol{t}_{\boldsymbol{\epsilon}}, \boldsymbol{q}\right) := \hat{\Psi}_\Omega^{mic}\left(\boldsymbol{\epsilon}_D, \epsilon_V, \boldsymbol{q}\right), \\ \Psi^{mac} &= \frac{3}{4\pi}\int_\Omega \Psi_\Omega^{mic} d\Omega. \end{aligned} \tag{2.7}$$

In equation (2.7), it is assumed that microplane free energy is a function of the plane-level strain vector $\boldsymbol{t}_{\boldsymbol{\epsilon}}$ (which incorporates the plane orientations according to equation (2.5)) and a set of plane-level internal variables accumulated in vector $\boldsymbol{q}$. According to equation (2.2), an alternative functional definition of Ψ_Ω^{mic} is considered via using V-D strain components ($\boldsymbol{\epsilon}_D$, ϵ_V) instead of $\boldsymbol{t}_{\boldsymbol{\epsilon}}$, along with the vector of internal variables $\boldsymbol{q}$.

2.1.2 Thermodynamically consistent framework

With the assumptions presented in equation (2.7), the standard form of macroscopic Clausius-Duhem inequality (CDI) will be applied to derive microplane constitutive equations, in the sense proposed in [70]:

$$\mathscr{D}^{mac} = \boldsymbol{\sigma} : \dot{\boldsymbol{\epsilon}} - \dot{\Psi}^{mac} \geq 0, \quad \text{with} \quad \dot{\Psi}^{mac} = \frac{3}{4\pi}\int_\Omega \dot{\Psi}_\Omega^{mic} d\Omega. \tag{2.8}$$

Furthermore, according to functional definition of $\dot{\Psi}_\Omega^{mic}$ in equation (2.7), we have:

$$\dot{\Psi}^{mic} = \frac{\partial \Psi^{mic}}{\partial \boldsymbol{\epsilon}_D} \cdot \dot{\boldsymbol{\epsilon}}_D + \frac{\partial \Psi^{mic}}{\partial \epsilon_V}\dot{\epsilon}_V + \frac{\partial \Psi^{mic}}{\partial \boldsymbol{q}} \cdot \dot{\boldsymbol{q}}. \tag{2.9}$$

Volumetric and deviatoric stress components are defined as work-conjugate pairs of the relevant strain quantities:

$$\boldsymbol{\sigma}_D := \frac{\partial \Psi^{mic}}{\partial \boldsymbol{\epsilon}_D}, \quad \text{and} \quad \sigma_V := \frac{\partial \Psi^{mic}}{\partial \epsilon_V}. \tag{2.10}$$

Moreover, microscopic dissipation is defined as:

$$\mathscr{D}^{mic} := -\frac{\partial \Psi^{mic}}{\partial \boldsymbol{q}} \cdot \dot{\boldsymbol{q}}. \tag{2.11}$$

If we substitute the results of equation (2.6) and the definitions (2.10, 2.11) into equation (2.9), we would obtain expressions for time-rates of microscopic and macroscopic HFE functionals:

$$\begin{aligned} \dot{\Psi}^{mic} &= \left[\overline{\overset{3}{\mathbf{Dev}} \cdot \boldsymbol{\sigma}_D} + \boldsymbol{V}\sigma_V\right] : \dot{\boldsymbol{\epsilon}} - \mathscr{D}^{mic}, \\ \dot{\Psi}^{mac} &= \frac{3}{4\pi}\int_\Omega \left[\overline{\overset{3}{\mathbf{Dev}} \cdot \boldsymbol{\sigma}_D} + \boldsymbol{V}\sigma_V\right] d\Omega : \dot{\boldsymbol{\epsilon}} - \frac{3}{4\pi}\int_\Omega \mathscr{D}_{mic} d\Omega. \end{aligned} \tag{2.12}$$

Comparing equation (2.12) with equation (2.8), the expressions for macroscopic stress and dissipation can be obtained:

$$\begin{aligned} \boldsymbol{\sigma} &= \frac{3}{4\pi}\int_{\Omega}\left[\overline{\overset{3}{\mathbf{Dev}}}\cdot\boldsymbol{\sigma}_D + \boldsymbol{V}\sigma_V\right]d\Omega, \\ \mathscr{D}^{mac} &= \frac{3}{4\pi}\int_{\Omega}\mathscr{D}_{mic}d\Omega \geq 0. \end{aligned} \tag{2.13}$$

E. Kuhl et al. [70] proposed a stronger assumption (sufficient for equation (2.13) to always satisfy the 2^{nd} law of thermodynamics), which provides the necessary tool for plane-level plasticity and damage formulations:

$$\mathscr{D}^{mic} \geq 0. \tag{2.14}$$

For calculation of the overall stress in equation (2.12), a numerical quadrature technique introduced by [78] is used. In this method, the integral over the surface of a unit-sphere is alternatively calculated by a weighted sum over finite microplane directions (the weights are represented by $w^{n_{mic}}$ in equation (2.15)). Although a higher number of microplanes results in more accurate approximations, Bažant & Oh in [78] indicated that 42 orientations result in sufficient accuracy. To further reduce the computational costs, the symmetry of the integration structure reduces the integration points to 21 (the corresponding weights and the coordinates of the integration points can be found in Appendices):

$$\boldsymbol{\sigma} = \frac{3}{4\pi}\int_{\Omega}\left[\overline{\overset{3}{\mathbf{Dev}}}\cdot\boldsymbol{\sigma}_D + \boldsymbol{V}\sigma_V\right]d\Omega \approx \sum_{n_{mic}=1}^{42}\left[\overline{\overset{3}{\mathbf{Dev}}}\cdot\boldsymbol{\sigma}_D + \boldsymbol{V}\sigma_V\right]\omega^{n_{mic}}. \tag{2.15}$$

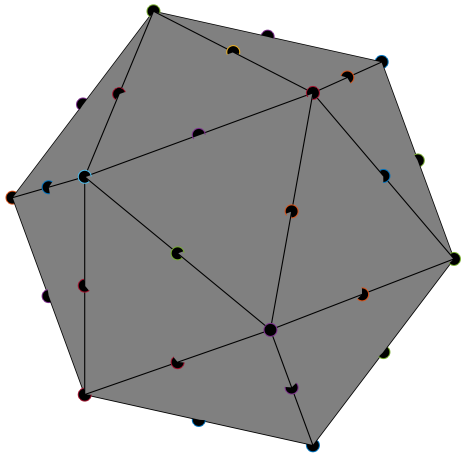

Figure 2.3: Representation of 42 integration points on the vertices and mid edges of an icosahedron for performing numerical integration over the surface of a unit-sphere.

2.1.3 DP-type plasticity and damage in microplane framework

In the scope of the small-strain theory, the macroscopic strain is additively decomposed into elastic and plastic parts:

$$\boldsymbol{\epsilon} := \boldsymbol{\epsilon}^e + \boldsymbol{\epsilon}^p. \tag{2.16}$$

Considering the kinematic constraint in equations (2.1) and (2.2), the additive elastic-plastic decomposition is also performed for the plane-level V-D strain components:

$$\epsilon_V := \epsilon_V^e + \epsilon_V^p, \quad \text{and} \quad \boldsymbol{\epsilon}_D := \boldsymbol{\epsilon}_D^e + \boldsymbol{\epsilon}_D^p. \tag{2.17}$$

In equation (2.11), the vector of internal variables $\boldsymbol{q}$ is assumed to be composed of plastic volumetric and plastic deviatoric strains, a scalar strain-like hardening variable κ^{mic}, and a damage variable d^{mic}:

$$\boldsymbol{q} = \left\{ \boldsymbol{\epsilon}_D^p, \epsilon_D^p, \kappa^{mic}, d^{mic} \right\}. \tag{2.18}$$

Inserting the functional form of the vector $\boldsymbol{q}$ to the definition of Ψ^{mic} in equation (2.7), renders the corresponding functional definition of Ψ^{mic}:

$$\Psi^{mic} = \hat{\Psi}^{mic} \left(\boldsymbol{\epsilon}_D, \epsilon_V, \boldsymbol{\epsilon}_D^p, \epsilon_V^p, \kappa^{mic}, d^{mic} \right). \tag{2.19}$$

The following definition is considered for the microplane HFE functional:

$$\Psi^{mic} := (1 - d^{mic})\Psi_0^{mic}. \tag{2.20}$$

In equation (2.20), Ψ_0^{mic} corresponds to the undamaged state of the material. The process of material degradation renders the value of the scalar variable d^{mic} to approach 1, and Ψ^{mic} to approach zero. The undamaged state of the material is defined as:

$$\Psi_0^{mic} := \frac{1}{2}K^{mic}\left(\epsilon_V - \epsilon_V^p\right)^2 + \frac{1}{2}G^{mic}\left(\boldsymbol{\epsilon}_D - \boldsymbol{\epsilon}_D^p\right)\cdot\left(\boldsymbol{\epsilon}_D - \boldsymbol{\epsilon}_D^p\right) + \frac{1}{2}H\kappa^{mic2}. \tag{2.21}$$

In equation (2.21), only isotropic hardening is assumed to take place. Also, K^{mic} and G^{mic} represent microplane bulk and rigidity moduli, respectively. As mentioned in [73], the relationship between these quantities and macroscopic bulk modulus (K), modulus of rigidity (G), modulus of elasticity (E), and Poisson's ratio (ν) is established as:

$$K^{mic} = 3K = \frac{E}{1-2\nu}, \quad \text{and} \quad G^{mic} = 2G = \frac{E}{1+\nu}. \tag{2.22}$$

Inserting the definition of the HFE functional presented in equation (2.20) into equation (2.10), we obtain the following relations for the volumetric and deviatoric stress components:

$$\sigma_V = \left(1 - d^{mic}\right)K^{mic}\left(\epsilon_V - \epsilon_V^p\right), \quad \text{and} \quad \boldsymbol{\sigma}_D = \left(1 - d^{mic}\right)G^{mic}\left(\boldsymbol{\epsilon}_D - \boldsymbol{\epsilon}_V^p\right). \tag{2.23}$$

Moreover, equation (2.11) with the definition of the HFE functional in equation (2.20), yields the plane-level energy dissipation:

$$\begin{aligned}\mathscr{D}^{mic} &= -\frac{\partial\Psi^{mic}}{\partial\epsilon_V^p}\dot{\epsilon}_V^p - \frac{\partial\Psi^{mic}}{\partial\boldsymbol{\epsilon}_D^p}\cdot\dot{\boldsymbol{\epsilon}}_D^p - \frac{\partial\Psi^{mic}}{\partial\kappa^{mic}}\dot{\kappa}^{mic} - \frac{\partial\Psi^{mic}}{\partial d^{mic}}\dot{d}^{mic}, \\ &= \sigma_V\dot{\epsilon}_V^p + \boldsymbol{\sigma}_D\cdot\dot{\boldsymbol{\epsilon}}_D^p + Y^{mic}\dot{d}^{mic} - \phi^p\dot{\kappa}^{mic} \geq 0.\end{aligned} \tag{2.24}$$

In equation (2.24), $Y^{mic} := -\dfrac{\partial\Psi^{mic}}{\partial d^{mic}} = \Psi_0^{mic}$, and $\phi^p := -\dfrac{\partial\Psi^{mic}}{\partial\kappa^{mic}}$ represent the energy-conjugate quantities to the damage, and hardening variables, respectively. To describe the evolution of the damage variable, a damage loading function Φ^d is considered:

$$\Phi^d = \phi^d(Y^{mic}) - d^{mic} \leq 0. \tag{2.25}$$

Application of the loading-unloading and consistency conditions to equation (2.25) yields:

$$\Phi^d \leq 0, \qquad \dot{\gamma}^{d,mic} \geq 0, \qquad \Phi^d\dot{\gamma}^{d,mic} = 0, \qquad \dot{\Phi}^d\dot{\gamma}^{d,mic} = 0. \tag{2.26}$$

In equation (2.26), $\gamma^{d,mic}$ represents a microplane damage multiplier arising from consideration of principle of maximum dissipation in equations (2.24) and (2.25).

Consequently, the evolution law for the damage variable is obtained as:

$$\dot{d}^{mic} = \dot{\gamma}^{d,mic} \frac{\partial \phi^d}{\partial Y^{mic}}. \tag{2.27}$$

According to [79], evaluation of the consistency condition results in $\dot{Y}^{mic} = \dot{\gamma}^{d,mic}$. In the case of a monotonic function $\phi^d \geq 0$, this result leads to an explicit updating scheme for the damage variable:

$$d^{mic} = \phi^d(\gamma^{d,mic}), \quad \text{with} \quad \gamma^{d,mic} = \underset{-\infty<\tau<t}{max} \left\{ Y^{mic}(\tau), \kappa_0^d \right\}. \tag{2.28}$$

In equation (2.28), κ_0^d represents a damage threshold that controls damage initiation. For the particular definition of damage in this study, the evolution of the damage parameter is assumed to be driven by the maximum value of the damage history parameter $(i.e., \gamma^{d,mic})$ over the microplanes surrounding the material point of interest. The functional form of the damage can be written as:

$$d^{mic} := \hat{d}^{mic}\left(\gamma^d\right) = 1 - exp\left[-\left(\frac{\gamma^d - \kappa_0^d}{a} \right)^p \right], \quad \text{with} \quad \gamma^d = \underset{mic=1}{\overset{21}{max}} \left\{ \gamma^{d,mic} \right\}. \tag{2.29}$$

In this equation, it is assumed that the values of the damage threshold for all microplanes are the same. When the damage energy release rate is below κ_0^d the value of d^{mic} is zero. During the loading process, the value of $\gamma^{d,mic}$ increases over all microplanes, and the first plane in which the history parameter reaches the threshold value initiates the damage mechanism. Moreover, a and p represent material parameters that control the material behavior in the descending portion of the stress-strain graph and they are to be determined via fitting the graphs to the experimental data.
Sources of damage (micro-crack and micro-void formation) result in reduction of a material's nominal cross-section; hence, in damaged material, effective stresses are greater than nominal ones, resulting in earlier plastic yielding. Hence, the evolution of plastic variables $\left(\epsilon_V^p, \boldsymbol{\epsilon}_D^p, \kappa^{mic}\right)$ in equation (2.24) is considered in undamaged (i.e., effective) stress-space. For this purpose, the plastic yield function is considered in the following form:

$$\Phi^p = \phi^p\left(\bar{\sigma}_V, \bar{\boldsymbol{\sigma}}_D\right) - \varphi^p\left(\kappa^{mic}\right) \leq 0. \tag{2.30}$$

The undamaged volumetric and deviatoric microplane stress components are represented as $\bar{\sigma}_V, \bar{\boldsymbol{\sigma}}_D$, respectively:

$$\bar{\sigma}_V := \frac{\sigma_V}{(1 - d^{mic})}, \quad \text{and} \quad \bar{\boldsymbol{\sigma}}_D := \frac{\boldsymbol{\sigma}_D}{(1 - d^{mic})}. \tag{2.31}$$

Application of the principle of maximum dissipation to equation (2.30) to solve the constrained optimization problem results in thee following evolution equations for the plastic variables:

$$\dot{\epsilon}_V^p = \dot{\gamma}^{p,mic}\frac{\partial \phi^p}{\partial \bar{\sigma}_V}, \qquad \dot{\boldsymbol{\epsilon}}_D^p = \dot{\gamma}^{p,mic}\frac{\partial \phi^p}{\partial \bar{\boldsymbol{\sigma}}_D}, \qquad \dot{\kappa}^{mic} = \dot{\gamma}^{p,mic}. \tag{2.32}$$

Also, the loading-unloading and consistency conditions take up the following expressions:

$$\Phi^p \leq 0, \qquad \dot{\gamma}^{p,mic} \geq 0, \qquad \Phi^p \dot{\gamma}^{p,mic} = 0, \qquad \dot{\Phi}^p \dot{\gamma}^{p,mic} = 0. \tag{2.33}$$

In this study, the particular form of the yield function is chosen to be of DP type. The macroscopic form of this criterion is formulated in terms of 1^{st} and 2^{nd} invariants of the overall stress tensor (represented by $\boldsymbol{I}_1$ and $\boldsymbol{J}_2$, respectively). As is mentioned in [71] and [73], these invariants can be formulated in terms of the V-D stress components:

$$\begin{aligned} \Phi^{DP,mac} &= \sqrt{\boldsymbol{J}_2} + \alpha^{mac}\boldsymbol{I}_1 - \sigma_0, \quad \text{with} \\ \boldsymbol{I}_1 &= \frac{3}{4\pi}\int_\Omega \sigma_V \, d\Omega, \quad \text{and} \quad \boldsymbol{J}_2 = \frac{3}{8\pi}\int_\Omega \boldsymbol{\sigma}_D \cdot \boldsymbol{\sigma}_D \, d\Omega. \end{aligned} \tag{2.34}$$

In this equation, σ_0 and α represent the initial yield stress, and macroscopic friction coefficient, respectively.

For obtaining the microplane version of the DP yield function, stress components are assumed to be constant across each microplane. Moreover, according to [71], the macroscopic and microscopic friction coefficients can be related as $\alpha^{mic} = \sqrt{\frac{3}{5}}\alpha^{mac}$. Addition of the linear hardening term together with the definition $\alpha := 3\alpha^{mac}$ results in the microplane form of the DP yield criterion. In the effective stress space, it takes the form:

$$\Phi^{DP,mic}\left(\bar{\sigma}_V, \bar{\boldsymbol{\sigma}}_D, \kappa^{mic}\right) = \sqrt{\frac{3}{2}\bar{\boldsymbol{\sigma}}_D \cdot \bar{\boldsymbol{\sigma}}_D} + \alpha\bar{\sigma}_V - \left(\sigma_0 + H\kappa^{mic}\right). \tag{2.35}$$

2.1.4 Numerical integration scheme

For the numerical integration of the model, the stresses at each material point are calculated using the radial return mapping algorithm. Also, the plastic and damage variables are updated at each increment of the displacement field. Within the small-strain setting, given the current-step displacement field $\boldsymbol{u}^{n+1}$, the current strain field

can be calculated as:

$$\boldsymbol{\epsilon}^{n+1} = \frac{1}{2}\left(\nabla \boldsymbol{u}^{n+1} + \nabla^T \boldsymbol{u}^{n+1}\right). \tag{2.36}$$

The volumetric and deviatoric components of the strain tensor are calculated via projecting the current strain on the microplanes surrounding the material point of interest according to equation (2.6). In the next step, the elastic trial states for microplane strain components are obtained as:

$$\epsilon_V^{e,trial} = \boldsymbol{V} : \boldsymbol{\epsilon}^{n+1} - \epsilon_V^{p,n}, \quad \text{and} \quad \boldsymbol{\epsilon}_D^{e,trial} = \overset{3}{\overline{\mathbf{Dev}}} : \boldsymbol{\epsilon}^{n+1} - \boldsymbol{\epsilon}_D^{p,n}. \tag{2.37}$$

Accordingly, the trial states of the effective volumetric and deviatoric microplane stresses are computed as:

$$\bar{\sigma}_V^{trial} = K^{mic}\epsilon_V^{e,trial}, \quad \text{and} \quad \bar{\boldsymbol{\sigma}}_D^{trial} = G^{mic}\boldsymbol{\epsilon}_D^{e,trial}. \tag{2.38}$$

Moreover, to check whether the current step corresponds to an elastic or plastic deformation, the yield function is computed for the trial stress components obtained in equation (2.38):

$$\Phi_{trial}^{DP,mic}\left(\bar{\boldsymbol{\sigma}}_D^{trial}, \bar{\sigma}_V^{trial}\right) = \sqrt{\frac{3}{2}\bar{\boldsymbol{\sigma}}_D^{trial} \cdot \bar{\boldsymbol{\sigma}}_D^{trial}} + \alpha\bar{\sigma}_V^{trial} - \left(\sigma_0 + H\kappa_n^{mic}\right). \tag{2.39}$$

If the trial stress states satisfy the yield criterion $\Phi_{trial}^{DP,mic} \leq 0$, the trial step corresponds to an elastic state, and the plastic strains at the current step correspond to their value at the end of the previous step; hence, no plastic flow occurs:

$$\epsilon_V^{p,n+1} = \epsilon_V^{p,n}, \quad \text{and} \quad \boldsymbol{\epsilon}_D^{p,n+1} = \boldsymbol{\epsilon}_D^{p,n}. \tag{2.40}$$

Similarly, plasticity and damage internal variables at the current step are assigned to their values from the previous step:

$$\kappa_{n+1}^{mic} = \kappa_n^{mic}, \quad \text{and} \quad \gamma_{n+1}^{d,mic} = \gamma_n^{d,mic}. \tag{2.41}$$

If $\Phi_{trial}^{DP,mic} > 0$, however, the trial state corresponds to a plastic step, and a plastic corrector step is required to bring the trial stress state onto the DP yield surface. For this step, the plasticity multiplier increment $\Delta\gamma_{n+1}^{p,mic}$ needs to be computed. The yield surface of the DP plasticity criterion has a conic shape, and the returned stress values, based on the condition $\Phi_{trial}^{DP,mic} = 0$, may lay on the yield surface itself or on the extension of the yield surface from its vertex in the tension region Figure 2.4.

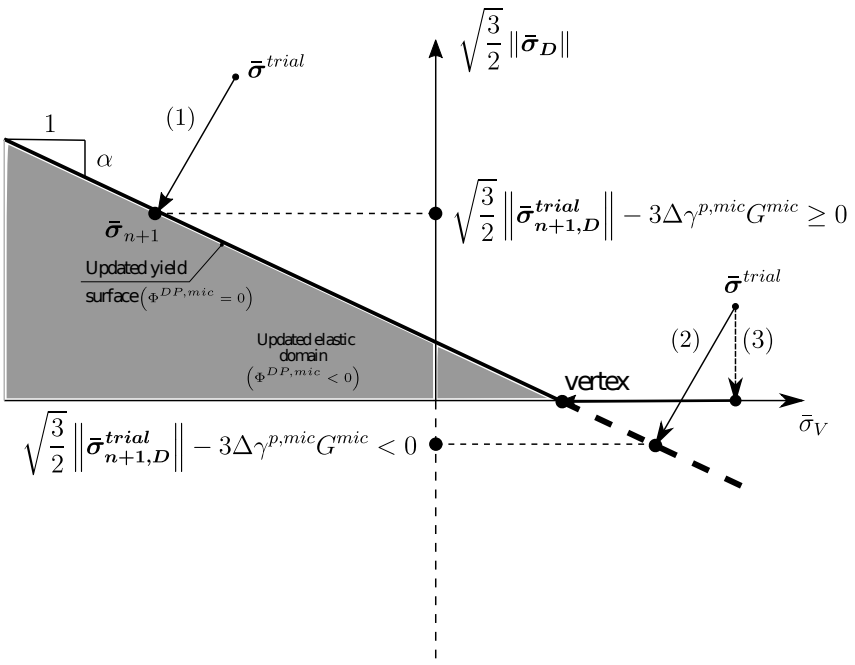

Figure 2.4: Representation of the return mappings for the DP yield criterion.

- *Return mapping to the smooth part of the updated DP cone:*

The flow directions for this part of the return mapping are derived as the following:

$$m_V := \frac{\partial \Phi^{DP,mic}}{\partial \bar{\sigma}_V} = \alpha, \quad \text{and} \quad \boldsymbol{m}_D := \frac{\partial \Phi^{DP,mic}}{\partial \bar{\boldsymbol{\sigma}}_D} = \sqrt{\frac{3}{2}}\frac{\bar{\boldsymbol{\sigma}}_D}{||\bar{\boldsymbol{\sigma}}_D||}. \tag{2.42}$$

Hence, the evolution equations for the plastic variables are obtained according to equation (2.32) as:

$$\epsilon_V^{p,n+1} = \epsilon_V^{p,n} + \Delta\gamma_{n+1}^{p,mic} m_V, \quad \boldsymbol{\epsilon}_D^{p,n+1} = \boldsymbol{\epsilon}_D^{p,n} + \Delta\gamma_{n+1}^{p,mic}\boldsymbol{m}_D^{trial}, \quad \kappa_{n+1}^{mic} = \kappa_n^{mic} + \Delta\gamma_{n+1}^{p,mic}. \tag{2.43}$$

Also, the volumetric and deviatoric effective stress components can be updated according to:

$$\bar{\sigma}_V^{n+1} = \bar{\sigma}_V^{trial} - \Delta\gamma_{n+1}^{p,mic} K^{mic} m_V, \quad \text{and} \quad \bar{\boldsymbol{\sigma}}_D^{n+1} = \bar{\boldsymbol{\sigma}}_D^{trial} - \Delta\gamma_{n+1}^{p,mic} G^{mic}\boldsymbol{m}_D^{trial}. \tag{2.44}$$

According to Figure 2.4, the two vectors $\bar{\boldsymbol{\sigma}}_D^{n+1}$ and $\bar{\boldsymbol{\sigma}}_D^{trial}$ share the same directions; hence, from equation (2.44), it can be deduced that:

$$||\bar{\boldsymbol{\sigma}}_D^{n+1}|| = ||\bar{\boldsymbol{\sigma}}_D^{trial}|| - \sqrt{\frac{3}{2}}\Delta\gamma_{n+1}^{p,mic} G^{mic}. \tag{2.45}$$

After returning the stress components onto the yield surface of the DP plasticity criterion, we will have:

$$\Phi^{DP,mic}\left(\bar{\boldsymbol{\sigma}}_D^{n+1}, \bar{\sigma}_V^{n+1}, \kappa_{n+1}^{mic}\right) = \sqrt{\frac{3}{2}\bar{\boldsymbol{\sigma}}_D^{n+1}\cdot\bar{\boldsymbol{\sigma}}_D^{n+1}} + \alpha\bar{\sigma}_V^{n+1} - \left(\sigma_0 + H\kappa_{n+1}^{mic}\right) = 0. \tag{2.46}$$

Substitution of equations (2.43) and (2.44) into (2.46) and using the condition expressed in equation (2.45), the plasticity multiplier can be obtained as:

$$\Delta\gamma_{n+1}^{p,mic} = \frac{\sqrt{\frac{3}{2}}||\bar{\boldsymbol{\sigma}}_D^{trial}|| + \alpha\bar{\sigma}_V^{trial} - \left(\sigma_0 + H\kappa_n^{mic}\right)}{\frac{3}{2}G^{mic} + K^{mic}\alpha^2 + H}. \tag{2.47}$$

Substitution of equation (2.47) into equations (2.43)-(2.44) completes the update scheme for the plastic variables and the V-D stress components. This mapping corresponds to path (1) in Figure 2.4; however, if the returned stress lies on the continuation of the yield surface (path (2) in Figure 2.4), a return mapping to the vertex of the yield surface is needed (path (3) in Figure 2.4). The two cases can be differentiated by the ordinate values of the returned effective stresses:

$$\begin{cases} \sqrt{\frac{3}{2}}||\bar{\boldsymbol{\sigma}}_{n+1,D}^{trial}|| - 3\Delta\gamma_{n+1}^{p,mic}G^{mic} \geq 0 & \Rightarrow \text{returned to the smooth portion of the yield surface,} \\ \sqrt{\frac{3}{2}}||\bar{\boldsymbol{\sigma}}_{n+1,D}^{trial}|| - 3\Delta\gamma_{n+1}^{p,mic}G^{mic} < 0 & \Rightarrow \text{return to the vertex of the yield surface is required.} \end{cases} \tag{2.48}$$

- *Return mapping to the vertex of updated DP cone:*

If the ordinate value of the returned stress is less than zero (i.e., 2^{nd} case in equation (2.48)), the trial stress is needed to return to the vertex of the yield surface. In this case, the deviatoric stress component of the effective microplane stress becomes zero. Hence, the yield function takes the following form:

$$\alpha\bar{\sigma}_V^{n+1} - \left(\sigma_0 + H\kappa_{n+1}^{mic}\right) = 0. \tag{2.49}$$

According to equation (2.43), the relation between the plastic multiplier and volumetric plastic strain rate $(\dot{\epsilon}_V^p)$ can be written as:

$$\Delta\gamma_{n+1}^{p,mic} = \frac{\Delta\epsilon_V^p}{m_V}. \tag{2.50}$$

Substituting the equations (2.43), (2.44), and (2.50) back into (2.49), the volumetric plastic strain change can be solved for as:

$$\Delta\epsilon_V^p = \frac{m_V\bar{\sigma}_V^{trial} - (\sigma_0 + H\kappa_n^{mic})}{m_V K^{mic} + H/\alpha}. \tag{2.51}$$

Hence, the effective stress components can then be updated according to:

$$\bar{\boldsymbol{\sigma}}_D^{n+1} = \mathbf{0}, \quad \text{and} \quad \bar{\sigma}_V^{n+1} = \bar{\sigma}_V^{trial} - K^{mic}\Delta\epsilon_V^p. \tag{2.52}$$

This return map brings the trial stress state to the vertex of the DP cone through the 3^{rd} path in Figure 2.4. Lastly, the update scheme for the plastic history variables is according to:

$$\boldsymbol{\epsilon}_D^{p,n+1} = \boldsymbol{\epsilon}_D^{p,n}, \quad \epsilon_V^{p,n+1} = \epsilon_V^{n+1} - \frac{\bar{\sigma}_V^{n+1}}{K^{mic}}, \quad \kappa_{n+1}^{mic} = \kappa_n^{mic} + \frac{\Delta\epsilon_V^p}{m_V}. \tag{2.53}$$

After obtaining the updated effective stresses, the current energy release rate is obtained as the driving force of damage:

$$Y_{n+1}^{mic} = \frac{1}{2}K^{mic}\left(\epsilon_V^{n+1} - \epsilon_V^{p,n+1}\right)^2 + \frac{1}{2}G^{mic}\left(\boldsymbol{\epsilon}_D^{n+1} - \boldsymbol{\epsilon}_D^{p,n+1}\right)\cdot\left(\boldsymbol{\epsilon}_D^{n+1} - \boldsymbol{\epsilon}_D^{p,n+1}\right) + \frac{1}{2}H{\kappa_{n+1}^{mic}}^2. \tag{2.54}$$

Based on equations (2.27) and (2.29), the state of damage is updated using the history of damage driving force during the loading history, and the state of damage energy release-rate at the surrounding microplanes:

$$\begin{aligned} &d_{n+1} = 1 - exp\left[-\left(\frac{\gamma_{n+1}^d - \kappa_0^d}{a}\right)^p\right], \quad \text{with} \\ &\gamma_{n+1}^d = \underset{mic=1}{\overset{21}{max}}\left\{\gamma_{n+1}^{d,mic}\right\}, \quad \text{and} \quad \gamma_{n+1}^{d,mic} = \underset{-\infty<\tau<t}{max}\left\{Y_{n+1}^{mic}(\tau), \kappa_0^d\right\}. \end{aligned} \tag{2.55}$$

Knowing the current states of damage and the effective stresses, which were considered in equation (2.31), the damaged V-D stresses can also be determined:

$$\sigma_V^{n+1} = (1 - d_{n+1})\,\bar{\sigma}_V^{n+1}, \quad \text{and} \quad \boldsymbol{\sigma}_D^{n+1} = (1 - d_{n+1})\,\bar{\boldsymbol{\sigma}}_D^{n+1}. \tag{2.56}$$

The V-D stress components in equation (2.55) are then substituted in equation (2.15) to obtain the current stress in the point of interest.

2.1.5 Model performance for hardened concrete

To check the performance of the proposed model, we adopted plain concrete uni-axial tension and compression test results which were reported by D. Feng et al. [17]. For this purpose, the values for Young's modulus and Poisson's ratio are set to 35 MPa and 0.2, respectively. The behavior of the model in the post-peak region is controlled by properly choosing the damage material parameters a and p in equation (2.29). An optimization scheme is used for fitting the model results to the experimental data via minimizing the least square errors. Tables 2.1 and 2.2 summarize the optimized plasticity- and damage-related parameters for the compressive and tensile loading scenarios, respectively.

Table 2.1: Material parameters for the uni-axial compression test.

$E\,[GPa]$	$\nu\,[-]$	$\sigma_0\,[MPa]$	α	$H\,[GPa]$	a	p	κ_0^d
35	0.2	7	0.25	45	70000	0.89	100

Table 2.2: Material parameters for the uni-axial tension test.

$E\,[GPa]$	$\nu\,[-]$	$\sigma_0\,[MPa]$	α	$H\,[GPa]$	a	p	κ_0^d
35	0.2	2	0.5	40	170	0.94	10

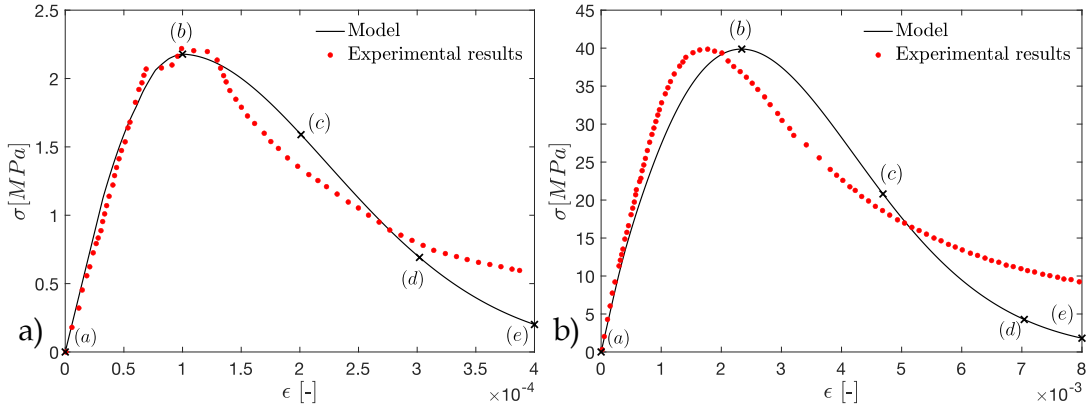

Figure 2.5: a) tensile and b) compressive stress-strain behavior of the suggested model compared to the experimental data.

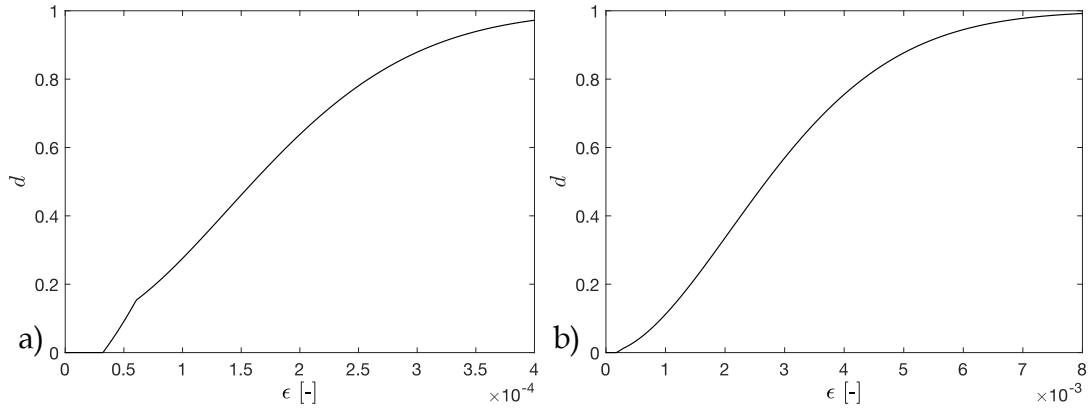

Figure 2.6: Evolution of the overall damage parameter in a) tensile and b) compressive loading history.

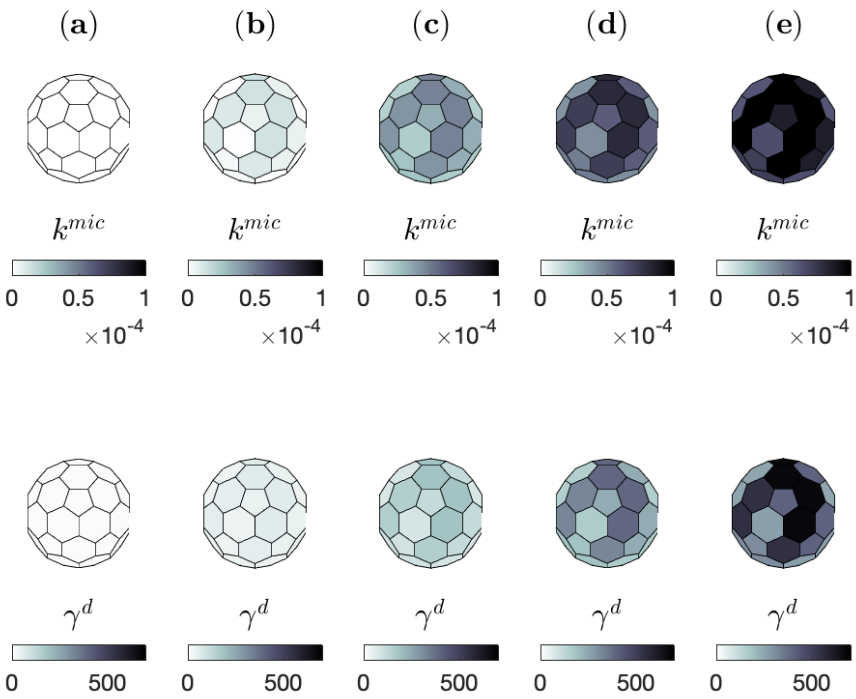

Figure 2.7: Evolution of the damage and plastic hardening variables, over the microplanes, in tensile loading history.

In Figure 2.5, the stress-strain behavior is demonstrated for the proposed model in tensile and compressive loading cases against an experimental data set for a strain change of $\Delta\epsilon = 0.008$ in compression, and $\Delta\epsilon = 0.004$ in tension. The model represents the post-peak softening effect, a characteristic of damaging materials. Moreover, the evolution of the damage variable during the loading process is represented in Figure 2.6.

Moreover, in Figure 2.5, five representative states are marked on the stress-strain curves. At the material point level, the evolution of damage and plasticity history parameters in tensile and compressive loading cases are represented on the surrounding microplanes in Figure 2.7 and 2.8, respectively, for the stages (a)-(d). As the loading progresses, the damage is concentrated in some microplanes and propagates towards the adjacent less damaged planes. In each loading step, the microplane in which the damage history parameter reaches the maximum value determines the overall damage

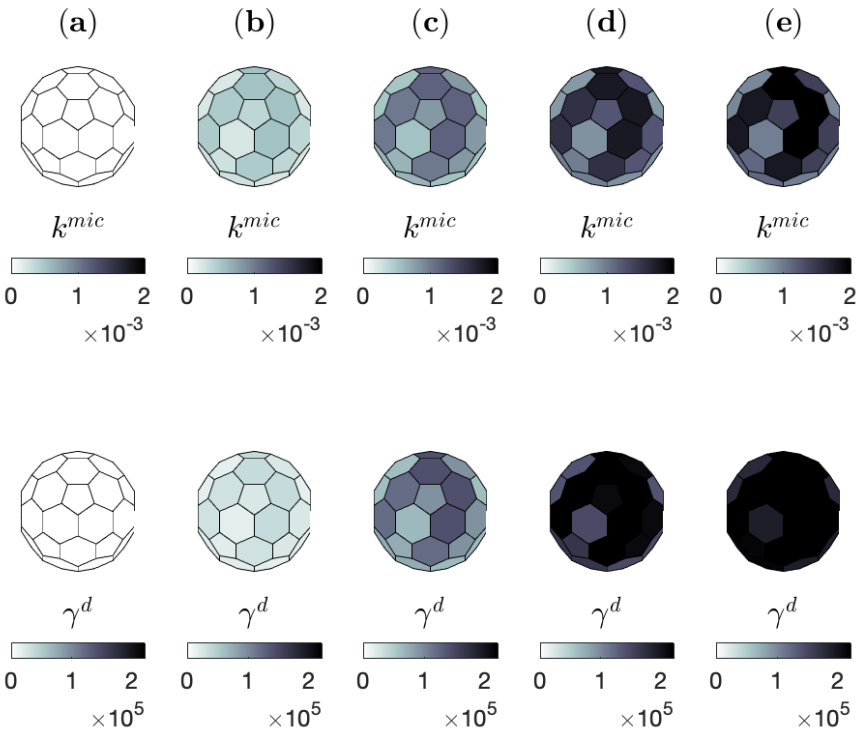

Figure 2.8: Evolution of the damage and plastic hardening variables, over the microplanes, in compressive loading history.

to the material.

2.2 Plasticity damage model introduced by D. Feng et al.

Based on the assumption of strain equivalence in classical continuum damage mechanics (CDM) [80, 81, 82], to define the effective (i.e. undamaged) stress state, the following definition was used:

$$\bar{\boldsymbol{\sigma}} := \mathbb{C}_0 : (\boldsymbol{\epsilon} - \boldsymbol{\epsilon}^p). \tag{2.57}$$

In this equation, $\boldsymbol{\epsilon}$, $\boldsymbol{\epsilon}^p$, and $\mathbb{C}_0$ represent the total strain, plastic strain, and the fourth-order intact stiffness tensors, respectively. In accordance with the formulation of J.Y. Wu et al. [80], an additive decomposition of the stress tensor into tensile and compressive sections was studied in order to differentiate the behavior of concrete

under tensile and compressive loading conditions:

$$\begin{aligned}
\bar{\boldsymbol{\sigma}} &:= \bar{\boldsymbol{\sigma}}^{+} + \bar{\boldsymbol{\sigma}}^{-}, \\
\bar{\boldsymbol{\sigma}}^{+} &= \mathbb{P}^{+} : \bar{\boldsymbol{\sigma}}, \\
\bar{\boldsymbol{\sigma}}^{-} &= \mathbb{P}^{-} : \bar{\boldsymbol{\sigma}}, \\
\mathbb{P}^{+} &= \sum_{t} H\left(\hat{\bar{\sigma}}_i\right) \boldsymbol{p}^{(i)} \otimes \boldsymbol{p}^{(i)} \otimes \boldsymbol{p}^{(i)} \otimes \boldsymbol{p}^{(i)}, \\
\mathbb{P}^{-} &= \mathbb{I} - \mathbb{P}^{+}.
\end{aligned} \tag{2.58}$$

In equation (2.58), $\mathbb{P}^{-}$, and $\mathbb{P}^{+}$ represent 4^{th} order projection tensors that function on the effective stress yielding the compressive, and tensile components, respectively. Additionally, the definition of these tensors is based on the eigenvalues ($\hat{\bar{\sigma}}_i$), and eigenvectors ($\boldsymbol{p}^{(i)}$) of the effective stress and $H(\bullet)$ represents the Heaviside function that performs the tensile (+)/compressive (-) decomposition on the effective stress. For the implementation of the plasticity and damage frameworks, the HFE functional was defined with the mathematical form of:

$$\psi := (1 - d^{+})\psi_0^{+} + (1 - d^{-})\psi_0^{-}. \tag{2.59}$$

In addition, the tensile (ψ_0^{+}), and compressive (ψ_0^{-}) portions of the free energy function were divided into elastic and plastic portions; for the specific definitions of elastic and plastic portions of the HFE, the recommendations of J.Y. Wu et al. [80] were adopted:

$$\begin{aligned}
\psi_0^{\pm} &= \psi_0^{e\pm} + \psi_0^{p\pm}, \\
\psi_0^{e\pm} &= \frac{1}{2}\left(\bar{\boldsymbol{\sigma}}^{\pm} : \mathbb{C}_0^{-1} : \bar{\boldsymbol{\sigma}}\right), \\
\psi_0^{p\pm} &= \int \bar{\boldsymbol{\sigma}}^{\pm} : d\boldsymbol{\epsilon}^{p}.
\end{aligned} \tag{2.60}$$

As the particular definition of ψ_0^{-}, J.Y. Wu et al. [80] hypothesized that the influence of tensile plastic strains on the total HFE potential was negligible. Hence, denoting the vector of internal variables as $\boldsymbol{q}$, for a plastic deformation of $\boldsymbol{\epsilon}^{p}$:

$$\psi_0^{p}(\boldsymbol{q}) = \psi_0^{p-}(\boldsymbol{q}) = \int_0^{\boldsymbol{\epsilon}^{p}} \bar{\boldsymbol{\sigma}}^{-} : d\boldsymbol{\epsilon}^{p}. \tag{2.61}$$

To account for the coupled effects of tensile and compressive concrete behavior, which is most prominent in the bi-axial loading case, J.Y. Wu et al. [80] introduced a parameter called "dilitancy parameter" (λ^{p} in below equations) for which a value

of 0.25756 was assigned (considering experimental data) to arrive at the following simplified definition for the compressive part of the HFE:

$$\psi_0^- = b_0 \left(\alpha \bar{\boldsymbol{I}}_1^- + \sqrt{3 \bar{\boldsymbol{J}}_2^-} \right)^2 . \tag{2.62}$$

In equation (2.62), $\bar{\boldsymbol{I}}_1^-$ and $\bar{\boldsymbol{J}}_2^-$ represent 1^{st} and 2^{nd} invariants of the compressive component of the effective stress tensor in equation (2.58). Moreover, b_0 and α represent material parameters with the following definitions:

$$\begin{aligned} \rho_0 &= \frac{f_{b0}^-}{f_0^-}, \rho = \rho_0 = 1.16, \\ \gamma &= \frac{1 - 2(1 - 2\nu_0)\rho^2}{(1 - 2\lambda^p)\rho^2 - (1 - \lambda^p)} \, (\lambda^p := 1.16), \\ \mu &= 3\gamma + 2(1 + \nu_0), \\ b_0 &= \frac{\mu}{6E_0}, b_1 = \frac{3\gamma\lambda^p}{\mu}, \alpha = \frac{b_1}{2}. \end{aligned} \tag{2.63}$$

The result in equation (2.62) was assumed a priori in the study of D. Feng et al. [17]. In the same study, to arrive at thermodynamically consistent definitions for total (i.e., damaged) stress and damage variables, the frameworks of HFE presented in equations (2.60) and (2.62) were incorporated into a traditional form of the CDI:

$$\dot{\gamma} = -\dot{\psi} + \boldsymbol{\sigma} : \dot{\boldsymbol{\epsilon}} \geq 0. \tag{2.64}$$

which in turn leads to the following definition of the 2^{nd} order Cauchy stress tensor ($\boldsymbol{\sigma}$) and damage energy release rates in tension and compression (Y^+ and Y^-, respectively) which are considered as the energy-conjugates to the strain tensor and tensile and compressive damage variables:

$$\begin{aligned} \boldsymbol{\sigma} &= (\mathbb{I} - \mathbb{D}) : \mathbb{E}_0 : (\boldsymbol{\epsilon} - \boldsymbol{\epsilon}^p) \, , \\ Y^+ = \psi_0^+ &\approx \frac{1}{2} \left(\bar{\boldsymbol{\sigma}}^+ : \mathbb{C}_0^{-1} : \bar{\boldsymbol{\sigma}} \right) , \\ Y^- = \psi_0^+ &\approx b_0 \left(\alpha \bar{\boldsymbol{I}}_1^- + \sqrt{3 \bar{\boldsymbol{J}}_2^-} \right)^2 . \end{aligned} \tag{2.65}$$

The damage driving forces Y^+ and Y^-, together with damage threshold values ($r^\pm$), lead to the determination of the damage variables in tensile and compressive loading cases:

$$\begin{aligned} d^\pm &= g^\pm(Y^\pm, r^\pm), \\ r^\pm &= \max_{\tau \in [0,t]} \{ Y^\pm(\tau) \}. \end{aligned} \tag{2.66}$$

Where $g^{\pm}(\bullet)$ are monotonic damage functions, the formulation of which may be derived from sub-scale or empirical correlation.

For calculating the plastic strain at each loading step, instead of using a completely rigorous treatment of plasticity evolution (identified by defining a yield surface and a flow rule) leading to computationally costly computations, D. Feng et al. [17] used one of the simplified formulations suggested by R. Faria et al. [81] (later modified by J.Y. Wu et al. [80]), based on empirical correlations, leading to improved numerical efficiency. In this framework, the definition of the plastic strain rate was formulated as:

$$\begin{aligned} \dot{\boldsymbol{\epsilon}}^p &= b^p \bar{\boldsymbol{\sigma}}, \\ b^p &= \xi^p E_0 H(\dot{d}^-) \frac{\langle \boldsymbol{\epsilon}^e : \dot{\boldsymbol{\epsilon}} \rangle}{\bar{\boldsymbol{\sigma}} : \bar{\boldsymbol{\sigma}}}. \end{aligned} \tag{2.67}$$

In equation (2.67), b^p represents the plastic flow parameter, whereas $\xi^p \geq 0$ and E_0 represent the plastic coefficient and initial modulus of elasticity, respectively.

For the particular definitions of the monotonic damage function, instead of utilizing the damage driving forces (Y^+, Y^-), energy equivalent strains ($\bar{\epsilon}^{e\pm}$) were defined for the tensile and compressive loading scenarios with the following forms:

$$\begin{aligned} \bar{\epsilon}^{e+} &:= \sqrt{\frac{2Y^+}{E_0}}, \\ \bar{\epsilon}^{e-} &:= \frac{1}{E_0(1-\alpha)} \sqrt{\frac{Y^-}{b_0}}. \end{aligned} \tag{2.68}$$

In these formulations, b_0 and α correspond to the parameters from equation (2.62). In addition, D. Feng et al. [17] incorporated the aforementioned definitions of the energy equivalent strains into the monotonic tensile and compressive damage functions, using the mathematical expressions described in [83]:

$$d^{\pm} = g^{\pm}(\bar{\epsilon}^{e\pm}) = \begin{cases} 1 - \frac{\rho^{\pm} n^{\pm}}{n^{\pm} - 1 + (x^{\pm})^{n^{\pm}}} & x^{\pm} \leq 1, \\ 1 - \frac{\rho^{\pm}}{\alpha^{\pm}(x^{\pm} - 1)^2 + x^{\pm}} & x^{\pm} \geq 1. \end{cases} \tag{2.69}$$

In the above description of the monotonic damage function, $\alpha^{\pm}$ are the parameters used to govern the descending stress-strain behavior of concrete under tensile and compressive loading conditions. Moreover, representing the concrete modulus of elasticity with E_c, ultimate tensile (+) and compressive strengths (-) with f_c^+ and f_c^-,

and the corresponding strains of $f_c^{\pm}$ with $\epsilon_c^{\pm}$, the parameters $x^{\pm}$, $\rho^{\pm}$, and $n^{\pm}$ were defined as:

$$x^{\pm} = \frac{\bar{\epsilon}^{e\pm}}{\epsilon_c^{\pm}},\ \rho^{\pm} = \frac{f_c^{\pm}}{E_c \epsilon_c^{\pm}},\ n^{\pm} = \frac{E_c \epsilon_c^{\pm}}{E_c \epsilon_c^{\pm} - f_c^{\pm}}. \tag{2.70}$$

Lastly, to further account for the softening behavior of concrete in compression in multiaxial loading cases, the compressive part in the definition of the Cauchy stress tensor in equation (2.65) was updated via multiplication of a softening coefficient "β" for which, considering the experimental compression test data, the following definition was proposed:

$$\beta := \frac{1}{\sqrt{1 + 400\bar{\epsilon}^{e+}}}. \tag{2.71}$$

In equation (2.71), the definition of β depends on the history of the tensile energy equivalent strain, which acts as a coupling between the tensile and compressive loading behaviors of concrete in multiaxial loading cases, and in the case of reverse loading, it accounts for the contribution of compression softening.

2.3 Gradient enhancement plasticity damage model introduced by I. Zreid & M. Kaliske (2018).

For the particular model proposed in this study, the theoretical framework presented in Section 2.1 holds, up to the equation (2.23). Due to the non-smooth edges of the conventional definition of the DP yield surface, it necessitates additional return algorithmics steps that may result in numerical complications. To rectify the mentioned problems, L. E. Schwer & Y. D. Murray [84] introduced a smooth capped version of the plastic yield surface. The same formulation was also utilized in the study of I. Zreid & M. Kaliske [2] as the microplane plastic yield surface:

$$\Phi^{mic}(\bar{\boldsymbol{\sigma}}_D, \bar{\sigma}_V, \kappa^{mic}) := \frac{3}{2}\bar{\boldsymbol{\sigma}}_D \cdot \bar{\boldsymbol{\sigma}}_D - \Phi^{DP}(\bar{\sigma}_V, \kappa^{mic})^2 f_c(\bar{\sigma}_V, \kappa^{mic}) f_t(\bar{\sigma}_V, \kappa^{mic}). \tag{2.72}$$

Similar to the definition in equation (2.35), the yield surface is defined in the effective stress-space in terms of effective volumetric ($\bar{\sigma}_V$), deviatoric ($\bar{\boldsymbol{\sigma}}_D$) stresses, and microplane strain-like hardening parameter (κ^{mic}). Moreover, in equation (2.72), Φ^{DP}, f_c, and f_t represent the DP yield function, tension, and compression caps, respec-

tively, with the definitions listed below:

$$\begin{aligned}\Phi^{DP} &= \sigma_0 - \alpha^{mic}\sigma_V^e + f_h(\kappa^{mic}),\\ f_c &= 1 - H(\sigma_V^C - \sigma_V^e)\frac{(\sigma_V^C - \sigma_V^e)^2}{X^2},\\ f_t &= 1 - H(\sigma_V^e - \sigma_V^T)\frac{(\sigma_V^e - \sigma_V^T)^2}{(T - \sigma_V^T)^2}.\end{aligned} \tag{2.73}$$

In this equation, $H(\bullet)$ represents the Heaviside function. Also, considering R_t and T_0 to be material parameters and representing the hardening function as $f_h(\bullet)$, the following definitions were adopted for X and T:

$$\begin{aligned}X &= R\Phi^{DP}(\sigma_V^C),\\ T &= T_0 + R_t f_h(\sigma_V^C).\end{aligned} \tag{2.74}$$

The hardening function in equation (2.74) was defined to have a linear dependence on the hardening variable (κ^{mic}) with the proportionality constant of D (also a material parameter). Denoting the plastic multiplier as $\gamma^{p,mic}$, the evolution equation for κ^{mic} is presented in equation (2.75):

$$\begin{aligned}f_h(\kappa^{mic}) &:= D\kappa^{mic},\\ \dot{\kappa}^{mic} &= \dot{\gamma}^{p,mic}.\end{aligned} \tag{2.75}$$

Moreover, the multiplicative introduction of tension and compression caps to Φ^{DP}[2] renders the yield surface to have the same slope as the original DP yield surface at the intersection points of Φ^{DP} with f_t and f_c, which results in the C^1 continuity (i.e. the existence of continuous derivatives at all points) of the resulting yield surface. Initial yield stress, microplane friction coefficient, and microplane strain-like hardening variables are symbolized as σ_0, α^{mic}, and κ^{mic}, respectively, in equation (2.73). In addition, σ_V^C and σ_V^T were deemed as material parameters representing the horizontal coordinates of the crossing points of tension and compression caps with the DP yield function, respectively. Additionally, R is defined as the ratio of the volumetric and deviatoric parts of the compression caps, which affects the amount of compression cap enlargement in hardening (i.e. the variable X). Finally, T_0 represents the initial tension cap's crossing coordinates with the horizontal axis, which increases to T during hardening, the amount of which is determined by the variable R_t. A schematic of the smooth yield-surface is given in Figure 2.9.

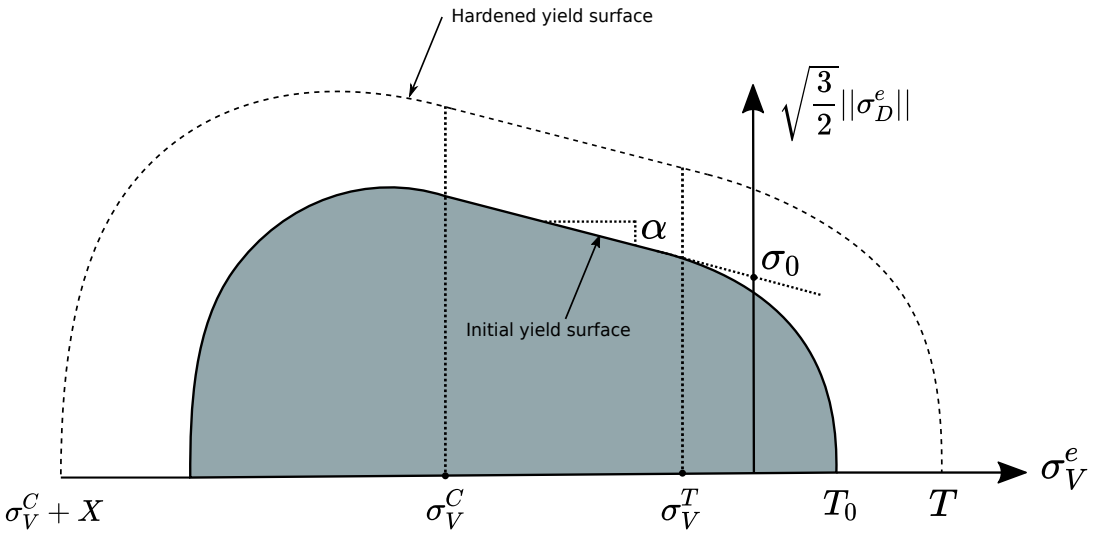

Figure 2.9: A schematic of the C^1 continuous capped DP yield sufrace used in [2].

In contrast to the compressive loading behavior, in which a degree of hardening behavior occurs prior to the onset of damage, it is known that the softening behavior of concrete under tension begins immediately when the elastic limit is achieved. In addition, if the loading direction is switched from tensile to compressive, the tensile stiffness loss is regained, however, in the reverse setting, the compressive damage persists in tensile loading. J. lee et al. [85] offered the following definition of damage, to incorporate the mentioned concrete softening behavior, which was also utilized by I. Zreid & M. Kaliske [2]:

$$(1 - d^{mic}) := (1 - d_c^{mic}) \cdot (1 - r_w d_t^{mic}). \tag{2.76}$$

In equation (2.76), the variables for microplane damage in tension and compression were defined as follows:

$$d_t^{mic} := 1 - \exp(\beta_t \gamma_t^{mic}),\ d_c^{mic} := 1 - \exp(\beta_c \gamma_c^{mic}). \tag{2.77}$$

Considering β_t and β_c as material parameters in equation (2.77), the evolution of the damage variables is governed by γ_t^{mic} and γ_c^{mic}. The evolution scheme for these variables was based on the equivalent strain variables (η_t^{mic} and η_c^{mic}) based on the following definition for tension:

$$\gamma_t^{mic} := \begin{cases} \eta_t^{mic} - \gamma_0^t & \eta_t^{mic} > \gamma_0^t, \\ 0 & \eta_t^{mic} \leq \gamma_0^t. \end{cases} \tag{2.78}$$

and for compression:

$$\gamma_c^{mic} := \begin{cases} \eta_c^{mic} - \gamma_0^c & \eta_c^{mic} > \gamma_0^c, \\ 0 & \eta_c^{mic} \leq \gamma_0^c. \end{cases} \tag{2.79}$$

in which γ_0^t and γ_0^t were regarded as material parameters regulating the onset of damage in tension and compression, respectively.

To distinguish the equivalent strains under compressive and tensile loading conditions and to hinder tensile damage in compression, the following definition of the partitioning scale parameter r_w in equation (2.76) was used based on the principal values of the equivalent strain tensor:

$$r_w = \frac{\sum_{I=1}^{3} \langle \epsilon_I \rangle}{\sum_{I=1}^{3} |\epsilon_I|}. \tag{2.80}$$

Lastly, for obtaining the equivalent strain variables, a gradient-enhancement scheme was proposed to enforce the displacement field to be void of discontinuities, resulting in a well-posed problem. For this reason, denoting the vector of microplane equivalent strains in tension and compression with $\boldsymbol{\eta}_m$:

$$\boldsymbol{\eta}_m := \begin{bmatrix} \eta_t^{mic} \\ \eta_c^{mic} \end{bmatrix} \tag{2.81}$$

The extra degree of freedom for the enhancement scheme was considered to be the non-local counter-part of the equivalent strain vector (i.e. $\bar{\boldsymbol{\eta}}_m$), for which a non-homogeneous Helmholtz-type PDE with homogeneous boundary condition was proposed, to be coupled with the balance of momentum equation:

$$\begin{aligned} \bar{\boldsymbol{\eta}}_m - c\nabla^2 \bar{\boldsymbol{\eta}}_m &= \boldsymbol{\eta}_m, \\ \nabla \bar{\boldsymbol{\eta}}_m \cdot \boldsymbol{n} &= 0. \end{aligned} \tag{2.82}$$

Where $\boldsymbol{n}$ denotes the outward normal to the system's boundary.

Using the over-non-local approach mentioned in [86, 87] to treat the regularization of the equivalent strain variables, I. Zreid & M. Kaliske [2] introduced the over-non-local equivalent tensile and compressive strains ($\hat{\eta}_t^{mic}$, $\hat{\eta}_c^{mic}$) as a weighted linear sum

of the local and non-local variables in tension and compression:

$$\begin{aligned}\hat{\eta}_t^{mic} &:= m\bar{\eta}_t^{mic} + (1-m)\eta_t^{mic},\\ \hat{\eta}_c^{mic} &:= m\bar{\eta}_c^{mic} + (1-m)\eta_c^{mic}.\end{aligned} \tag{2.83}$$

The weight parameter "m" in equation (2.83) was regarded as a material parameter to be tuned to the particular experimental data. Later, the over-non-local parameters were introduced to equations (2.78) and (2.79) to alter the formulations of governing damage variables:

$$\gamma_t^{mic} = \begin{cases} \hat{\eta}_t^{mic} - \gamma_0^t & \hat{\eta}_t^{mic} > \gamma_0^t,\\ 0 & \hat{\eta}_t^{mic} \leq \gamma_0^t. \end{cases}, \gamma_c^{mic} = \begin{cases} \hat{\eta}_c^{mic} - \gamma_0^c & \hat{\eta}_c^{mic} > \gamma_0^c,\\ 0 & \hat{\eta}_c^{mic} \leq \gamma_0^c. \end{cases} \tag{2.84}$$

For the constructed model to be easily used with the parameters typically obtained from performing uni-axial (tension and compression) and bi-axial tests on concrete, I. zreid & M. Kaliske [2] utilized the approximation formulas presented in [88] to express the uni-axial tensile (f_t) and bi-axial compressive (f_b) strengths in terms of uni-axial compressive strength (f_c). Also, some of the presented material parameters of the presented plasticity damage model were expressed in terms of the uni-axial and bi-axial strengths according to equation (2.85):

$$\begin{aligned} f_b &= 1.15 f_c,\\ f_t &= 1.4\left(\frac{f_c}{10}\right)^{\frac{2}{3}},\\ \alpha &= \frac{\sqrt{3}\,(f_b - f_c)}{2f_b - f_c},\\ \sigma_0 &= \left(\frac{1}{\sqrt{3}} - \frac{\alpha}{3}\right) f_c,\\ \sigma_V^T &= -\frac{1}{3} f_c,\\ \sigma_V^C &= \frac{2}{3} f_b,\\ T_0 &= \frac{1}{3} f_t. \end{aligned} \tag{2.85}$$

CHAPTER 3

RESULTS AND DISCUSSIONS

3.1 Unconfined uni-axial compression tests

A series of UUCT tests were conducted, in a sense performed by R.J.M. Wolfs et al. [1], to capture the time-change of modulus of elasticity. For the preparation of samples, two-piece cylindrical dies with $d = 10$ cm and a height-to-diameter ratio of $h/d = 2$ were prepared to see the formation of the shear failure plane and to avoid the size effects. Oil was applied to the interior of all dies before pouring the samples to eliminate induced deformations in the samples during die removal. To render the samples homogeneous, the dies were filled in 3 steps, each followed by a compaction process. The tests were performed on fresh specimens in a displacement-controlled fashion up to $25\,\%$ total deformation at ages of 5, 15, 25, 35, 45, 55, 65, 75, 85 minutes. Experimental measurements were not feasible for ages below 5 minutes since the specimen did not maintain its initial shape. Also, the end of the mixing step was set as the reference to measure specimen ages. For each age, the UUCT tests were repeated twice, and their nominal averages were considered to assure the consistency of the results. The results were transformed into stress-strain (i.e., $\sigma - \epsilon$) plots. Figures 3.1, and 3.3 represent the individual and comparative $\sigma - \epsilon$ diagrams for all ages considered, respectively.

After obtaining the average $\sigma - \epsilon$ graphs, Young's Modulus was calculated for each age of the tested samples from the linear portions of the stress-strain graphs up to 0.05 strain. The obtained Young's moduli are indicated in Figure 3.1.

As it can be seen in this Figure, by the increase in Young's moduli with age, the advancement of hydration and curing processes in concrete samples resulted in their

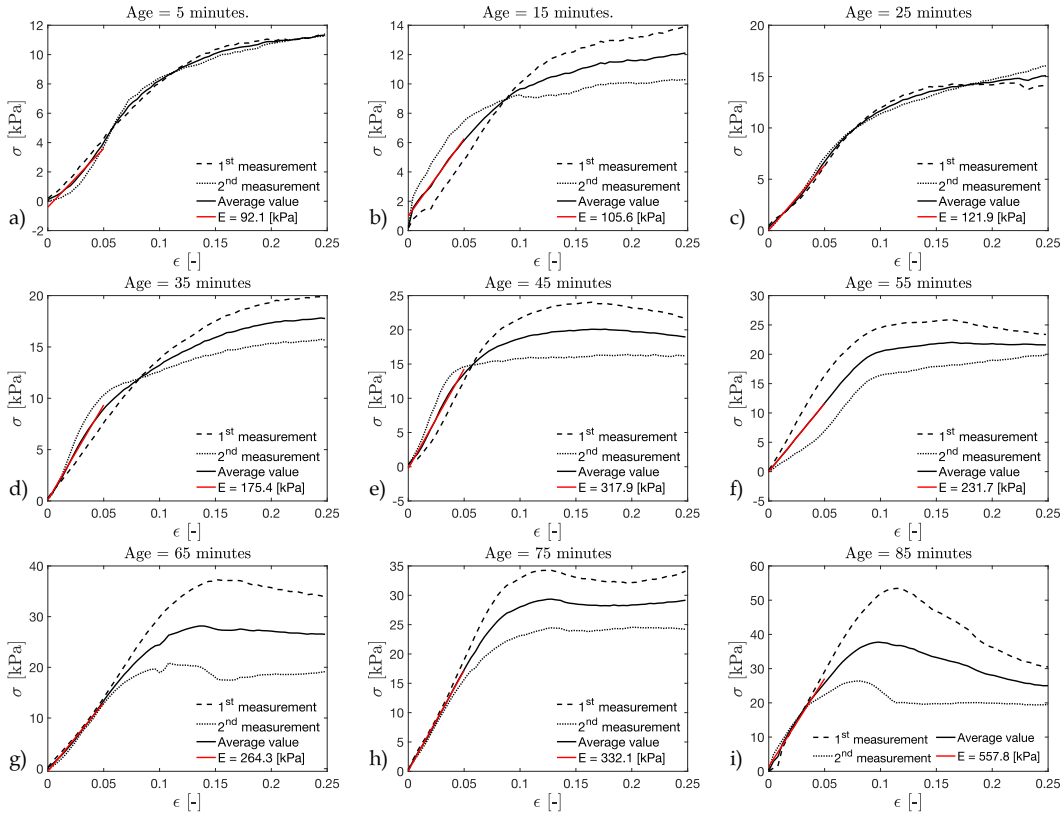

Figure 3.1: The acquired stress-strain data from displacement-controlled UUCT tests conducted for a) 5 minutes up to i) 85 minutes.

Figure 3.2: Three stages of the UUCT test, performed for a specimen at 35 minutes of age, up to a strain change of 25%.

hardening. In addition, further displacement in the compression process resulted in a softening of the tested materials' stress-strain response, as seen in Figure 3.3. Softening damage behavior is more pronounced in older samples, which can be attributed to the creation and merging of microcracks in the samples' microstructure. During

performing UUCT experiments, it was noticed that the onset of softening coincided with the appearance of cracks in the test samples' structures (Figure 3.2).

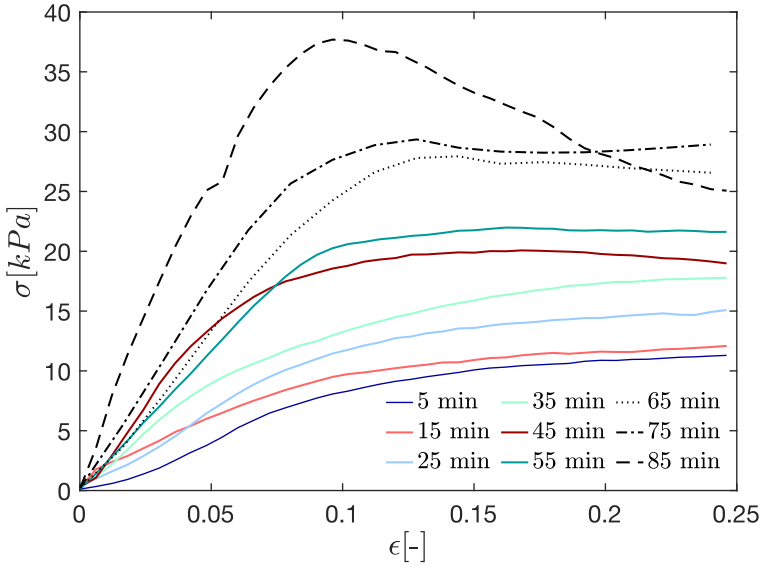

Figure 3.3: The stress-strain graphs for early-age samples performed at ages of 5, 15, 25, 35, 45, 55, 65, 75, 85 minutes.

3.2 Curing kinetics in early-age concrete

During the curing process, material properties and Young's modulus demonstrate an age-dependent change. In the framework of time-dependent change of material properties in the early-age setting, "degree of cure" or "χ" is considered as a quantification of the curing process with values of $\chi = 0$ and $\chi = 1$ corresponding to "uncured" and "completely cured" states, respectively. This parameter will be used in framing a time-dependent setting for the evolution of the modulus of elasticity. It is assumed that the degree of cure evolves through a thermally-activated process, for which a 1^{st} degree ODE is assumed to describe its evolution in time.

$$\dot{\chi} = k\chi^m(1-\chi)^n. \tag{3.1}$$

To further simplify the analyses, it is assumed that in equation (3.1), $n = 1-m$. Doing so eliminates one of the material parameters and results in computational efficiency in the curve-fitting optimization processes. To get a stable solution for all step-size ranges, equation (3.1) is solved using an implicit Euler scheme. Moreover, to account

for the dependency of the degree of cure on temperature, an Arrhenius-type equation is considered for the parameter k.

$$k := k_0 \, exp\Big(- \frac{E}{R\theta} \Big). \tag{3.2}$$

In equation (3.2), E and R represent the activation energy for the evolution of χ and the universal gas constant, respectively. For the proposed evolution scheme based on equations (3.1), and (3.2), k_0, E, and m are considered to be material parameters related to the curing process. We assume the following form to relate the current values of Young's modulus to the state of the curing process.

$$E = \bar{E}(\chi) := \chi^b E_f + (1 - \chi)^c E_i. \tag{3.3}$$

In this equation, b and c are provided as material parameters to enhance the fitting performance of the scheme throughout the whole curing spectrum. They are determined by fitting the theoretical elasticity moduli to the empirically obtained values. Additionally, E_i and E_f indicate the initial and final values of Young's moduli, respectively, during the curing process. E_i is set equal to the obtained Young modulus for the freshest examined specimens (i.e., at 5 min). Due to the fact that the printing process of bigger or more intricate pieces may require further time to complete and harden, the curing process of early-age concrete is deemed complete at the end of one day. Young's modulus was measured at one day of age using an LVDT device attached to a cast cylindrical specimen with dimensions of d = 10 cm and h = 20 cm in order to determine the value of E_f. All the experiments were conducted at room temperature resulting $\theta = 20^{\circ}$C. In addition, in equation (3.3), the functional form of E is written as an interpolation between E_i = 92.145 kPa and E_f = 10.8 GPa, with regard to the degree of cure. The initial value of E throughout the curing process is E_i, and it converges to E_f once the curing process is finished. The material parameters presented in equations (3.1) - (3.3) are acquired by fitting the predicted Young's moduli of elasticity in equation (3.3) to the empirically determined values of Figure 3.2. Figure 3.4 depicts the development of the degree of cure, as well as theoretical and experimental moduli of elasticity, over the course of a day. Moreover, Table 3.1 contains the optimized material parameters for curing kinetics of the tested samples.

The formulation presented in equations (3.1) - (3.3) are implemented in such a fashion that the thermal dependence of evolution of the degree of cure can also be in-

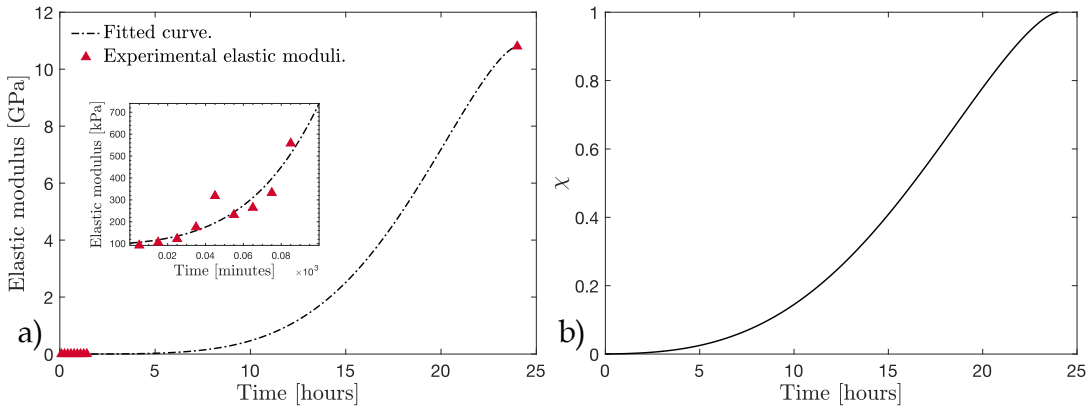

Figure 3.4: Evolution of a) Young's modulus and b) the degree of cure over time.

Table 3.1: Material parameters for the evolution of the degree of cure.

m	k_0	$E\left[\frac{kJ}{kg\,mol}\right]$	$R\left[\frac{kg\,m^2}{s^2\,mol\,K}\right]$	b	c
0.671	1.439	25557	8.3144	1.625	1.299

corporated. This means that knowing the temperature at which the UUCT tests were conducted, the evolution of χ at any other one can also be obtained. Increasing the temperature accelerates the convergence of the degree of cure towards completion, hence accelerating the early-age concrete's curing kinetics. Consequently, the temperature dependence of Young's moduli could also be accounted for using the provided formulation.

3.3 Hydration kinetics in early-age concrete

In a study conducted by G. D. Shutter et al. [16], specimens ranging in age from 12 hours to 28 days were subjected to adiabatic and isothermal hydration tests. In addition, mechanical splitting, uni-axial, and flexural tests were done for each age group under tensile and compressive loading scenarios. According to the findings, there was an almost linear relationship between the evolution of degree of hydration and compressive strength. This hypothesis has become a common method for assessing the degree of hydration at different concrete ages. In the same study, a power law

framework with two material parameters was presented to relate the degree of hydration to compressive strength. In another study, J. L. Provis et al. [89] proposed an exponential-type evolution equation for the degree of hydration. In the scope of this study, the assumptions of the two cited studies are used to provide a mathematical description of the evolution of the degree of hydration in early-age concrete. Initially, the following exponential form is assumed to describe the time dependency of ξ:

$$\xi = \bar{\xi}(t) := 1 - \left(exp\left(-t/\tau\right)\right)^{d}. \tag{3.4}$$

In addition, the following power law relationship is postulated between the degree of hydration, the final compressive strength, and the present value of compressive strength:

$$f_c = \bar{f}_c(t) := f_c^u \cdot \xi(t)^e. \tag{3.5}$$

In equations (3.4) and (3.5), d, τ, and e reflect material-related parameters determined by fitting the relevant graphs to the mix-specific experimental data. Also, f_c^u denotes the compressive strength of concrete at the end of the 28^{th} day. Furthermore, to obtain the material parameters, a series of uni-axial splitting compression tests were performed to assess the compressive strengths at $1, 3, 7, 14, 21,$ and 28 days of age. In Figure 3.5.b, experimental measurements are shown by red markers.

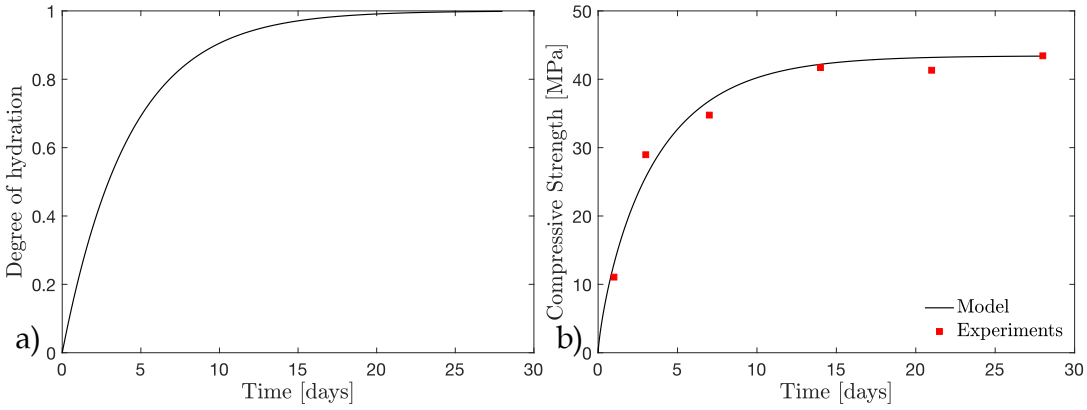

Figure 3.5: Evolution of a) degree of hydration, and b) compressive strengths.

The compressive strength measurements, along with the definitions of equations (3.4) and (3.5), are employed in an error minimization procedure to estimate the material parameters. Figures 3.5.a and .b, respectively, depict the resultant time-evolution of $\xi(t)$ and $f_c(t)$ as solid lines. Also, the obtained hydration kinetics material parameters

Table 3.2: Material parameters for describing the kinetics of hydration for the used mix in Section 3.1.

$f_c^u\,[MPa]$	$\tau\,[days]$	d	e
43.43	3.833	0.904	0.773

are summarized in Table 3.2.

Based on published experimental data, G. D. Schutter et al. [16] established a mathematical relationship between the Poisson's ratio and the degree of hydration, which has the following mathematical form:

$$\nu\left(\xi\right) = 0.18 sin\left(\frac{\pi\xi}{2}\right) + \frac{1}{2} exp\left(-10\xi\right). \tag{3.6}$$

Based on this model, for each age of the concrete, the resulting value of ξ can be

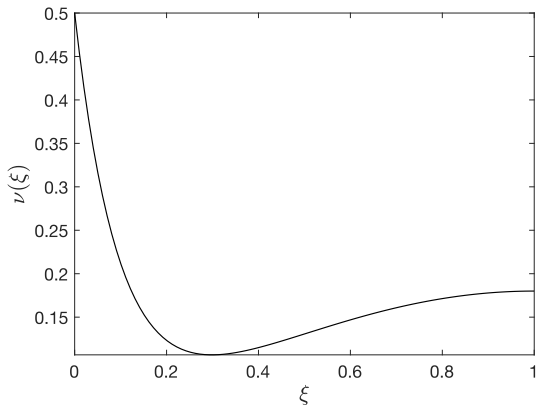

Figure 3.6: The relation between ν and ξ according to [16].

introduced into equation (3.6) to yield the age-specific Poisson's ratio, which refers to the macroscopic value of Poisson's ratio, stated in Section 2.1.3. Figure 3.7 illustrates the associated Poisson's ratio results for the ages at which the UUCT tests were performed in Section 3.1, as well as the additional ages of 2h, 4h, and one day.

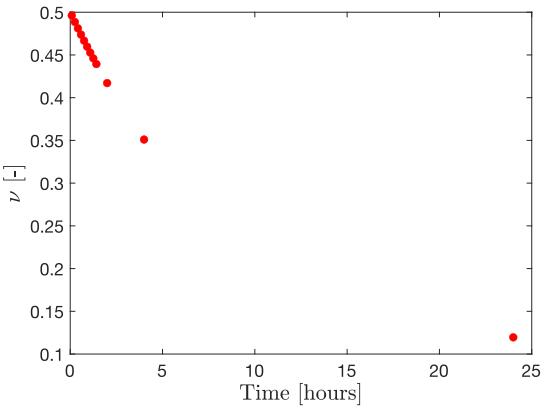

Figure 3.7: Evolution of Poisson's ratio during a 24-hour period.

3.4 Incorporation of curing and hydration kinetics into the microplane DP plasticity damage model

So far, frameworks have been constructed for the evolution of the degree of hydration and cure, which also characterize the evolution of Young's modulus and Poisson's ratio at different ages. To represent the early-age behavior of concrete, the microplane plasticity damage method described in Section 2.1.3 is integrated with the results of Sections 3.2 and 3.3. According to equation (2.22), the microplane moduli of elasticity and rigidity can be derived from the macroscopic modulus of elasticity and the Poisson's ratio; furthermore, the macroscopic Young's modulus and Poisson's ratio are assumed to have the functional form presented in equations (3.3) and (3.6), respectively, in terms of degree of cure (ξ) and hydration (χ).

The algorithmic treatment to incorporate the curing kinetics into the microplane plasticity damage scheme involves the following steps:

Assuming that for a representative material point the macroscopic strain tensor ($\boldsymbol{\epsilon}^{n+1}$) is known for the current time step (t_{n+1}), and the history parameters ($Y_n^{mic}, \epsilon_V^{p,n}, \boldsymbol{\epsilon}_D^{p,n}, \kappa_n^{mic}$) and microplane stresses (σ_V^n and $\boldsymbol{\sigma}_D^n$) are known at the end of previous time step (t_n):

1. Find the current degree of hydration χ_{n+1} according to the equation (3.1).
2. Find the current degree of cure ξ_{n+1} according to the equation (3.4).

3. Find the current modulus of elasticity $E_{n+1}\,(\chi_{n+1})$ according to the equation (3.3).

4. Find the current Poisson's ratio $\nu_{n+1}\,(\xi_{n+1})$ according to the equation (3.6).

5. Find the microplane bulk modulus (K_{n+1}^{mic}) and modulus of rigidity (G_{n+1}^{mic}) for the current step according to the equation (2.22).

6. Update the damage and plasticity history parameters ($Y_{n+1}^{mic}, \epsilon_V^{p,n+1}, \boldsymbol{\epsilon}_D^{p,n+1}, \kappa_{n+1}^{mic}$) , and find the current microplane and macroscopic stresses ($\sigma_V^{n+1}, \boldsymbol{\sigma}_D^{n+1}, \boldsymbol{\sigma}^{n+1}$) according to the integration scheme presented in Section 2.1.4.

The time-dependent stress-strain behavior of the early-age concrete samples obtained from UUCT tests are examined to check the performance of the proposed solid mechanical buildability model. For this purpose, the data reported in [1] and the experimental results of this study (Figure 3.1) are going to be used.

3.4.1 UUCT results from the work of R.J. Wolfs et al. (2018)

R.J.M. Wolfs et al. [1] conducted UUCT tests on early-age cylindrical specimens with diameters of d = 70 cm and h/d ratio of 2 at room temperature (22 $^{\circ}C$). The tests were conducted for ages of 0, 15, 30, 60, and 90 minutes, and the results were obtained in terms of force-displacement curves and transformed into stress-strain diagrams. To integrate the experimental data to the scheme presented in Section 3.4, initially, the moduli of elasticity for the specimens at different ages were measured. For this purpose, strains up to 0.01 were used. Since the available stress-strain data in this study ranged from 0 to 90 minutes, there is no need for the parameters b and c in equation (3.3) to improve the fitting capabilities of the curing model, and the fitting objective is well-achieved by setting them equal to 1. Moreover, due to the lack of compressive strength data over 28 days and the fact that the available experimental measurements of the Poisson's ratio in the literature over the considered ages report very close values (for example, in [16] the value of the Poisson's ratio for the very early-age concrete is proposed to be 0.5), the evolution of the degree of hydration obtained in Section 3.3 (from the fitting results of the uni-axial compression tests) is applied to obtain the values of Poisson's ratio. Consequently, the material parame-

ters regarding the hydration kinetics (i.e. τ, d, and e) are equal to the ones presented in Table 3.2. Furthermore, the initial and final moduli of elasticity are inserted into equation (3.3) to determine the evolution of Young's modulus. Fitting the computed E values (as functions of χ) to the experimentally obtained Young's moduli is conducted by performing an optimization scheme in terms of minimizing the mean square error between the experimental and theoretical data sets, which results in the determination of the curing-related material parameters, which are summarized in Table 3.3. Inserting the parameters in Table 3.3 back into equations (3.1)-(3.3) results in obtaining the values of E and χ at different times, as they are represented in Figures 3.8a. and Figure 3.8.b. .

Table 3.3: Material parameters pertaining to curing kinetics for the UUCT tests performed in [1].

m	k_0	$E\left[\frac{kJ}{kg\,mol}\right]$	$R\left[\frac{kg\,m^2}{s^2\,mol\,K}\right]$	b	c
0.424	2.942	21484	8.314	1.000	1.000

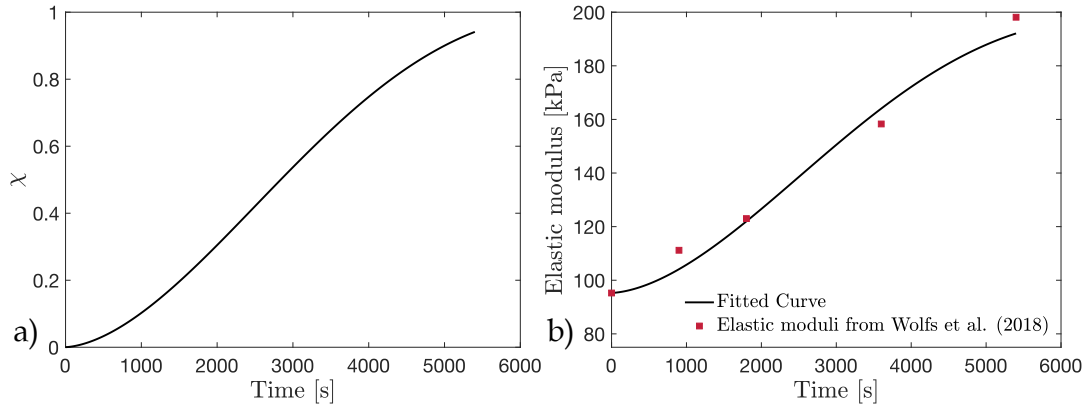

Figure 3.8: Evolution of (a) degree of hydration and (b) Young's modulus versus time for the UUCT data in [1].

In the following step, the Young's modulus and Poisson's ratio for each age are supplied into the described algorithm in Section 3.4, resulting in age-dependent stresses at material points at which the displacements were measured in the UUCT tests. The material parameters are determined via an error minimization process between the

theoretical and experimental stress results for all strain increments. The assumed definition for the cumulative error is given in equation (3.7):

$$Error := \frac{1}{m}\sum_{i=1}^{m}\left(\sigma_{i,model} - \sigma_{i,experiment}\right)^2 . \tag{3.7}$$

In this equation, $m, \sigma_{i,model}$, and $\sigma_{i,experiment}$ refer to the total number of strain increments, obtained stresses from the microplane DP model, and the UUCT, respectively. The optimized values of $\sigma_0, \alpha, H, a, p, k_0^d$ are summarized in Table 3.4.

Table 3.4: Optimized material parameters for fitting stress-strain results obtained from the microplane DP model (used in the early-age scheme) to the UUCT results of [1].

$Age\,[min]$	$\sigma_0\ [kPa]$	α	$H\ [kPa]$	a	p	κ_0^d	$\nu\,[-]$
0	17.00	0.25	1000	940	0.50	40	0.4999
15	18.00	0.27	1300	1194	0.58	40	0.4886
30	19.23	0.28	1500	1580	0.71	40	0.4775
60	20.52	0.30	2300	2282	0.99	40	0.4562
90	21.98	0.33	2900	2250	1.30	40	0.4361

Figure 3.10 contains the stress-strain outputs of the microplane DP model and the results of the UUCT tests for all ages. According to the microplane DP model in Section 2.1.3, the damage threshold parameter (k_0^d) determines the initiation of damage as the loading progresses and it is one of the parameters which controls the extension of the linear portion of the stress-strain graph. Since the extensions of the linear portions of the stress-strain graphs are assumed equal for all ages of the tested samples in measurements of Young's moduli (i.e., up to 0.01 strain), the damage threshold values are also set equal in determining the material parameters. Moreover, as the hydration process continues, material hardening delays the onset of plastic deformation and increases the plasticity hardening modulus. This can be observed in the increasing trends observed in the initial yield (σ_0), friction coefficient (α), and the hardening modulus (H) parameters in the 2^{nd}, 3^{rd}, and 4^{th} columns of the Table 3.4, respectively. Figure 3.9 showcases a graphical representation of the consistent increase in the plasticity- and damage-related parameters, corresponding to the UUCT test results conducted by Wolfs et al. (2018) [1].

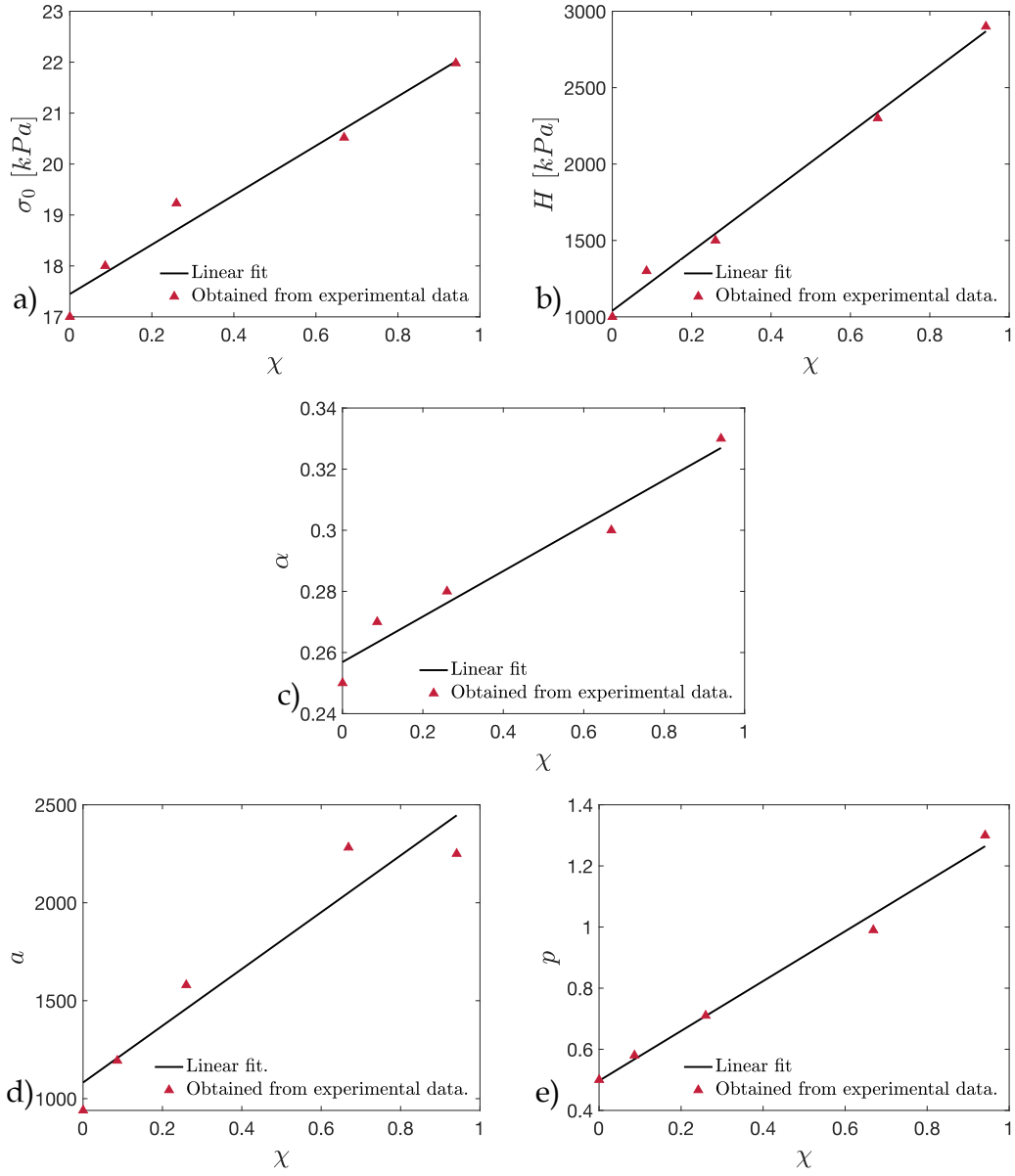

Figure 3.9: The evolution of the material parameters, introduced in the microplane plasticity damage model of Section 2.1, for the ages considered in the UUCT results conduceted in [1].

3.4.2 UUCT results from experiments of the current study

The framework which was introduced in Section 3.4 is also used for the UUCT experiment results presented in Section 3.1. For reaching this purpose, solutions of degree of cure (equation (3.1)), degree of hydration (equation (3.4)), modulus of elasticity

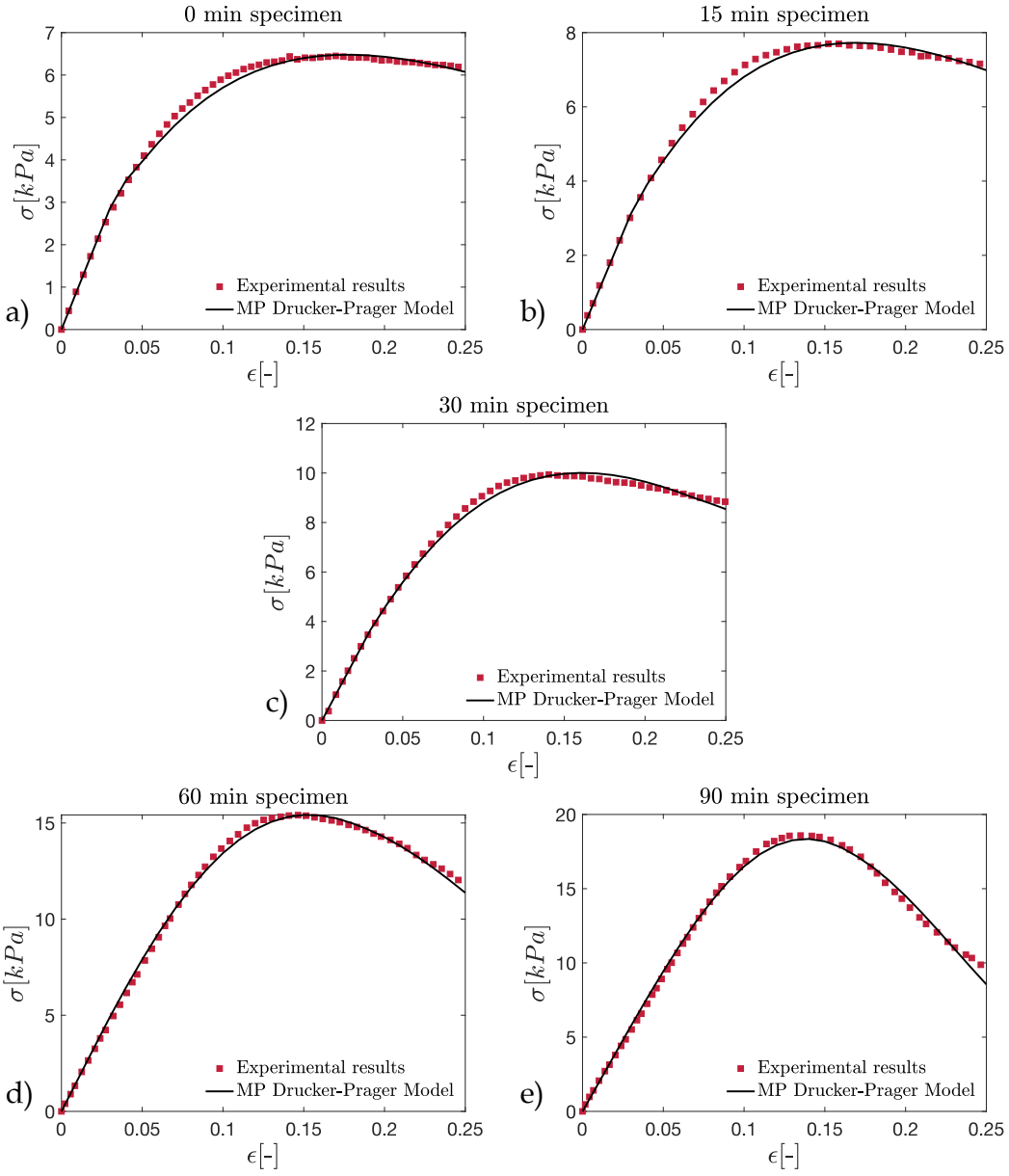

Figure 3.10: UUCT results from [1] and theoretical predictions of the stress-strain behavior of fresh concrete, when the microplane plasticity damage model, developed in Section 2.1, is used in the early-age scheme.

(equation (3.3)), and Poisson's ratio (equation (3.6)) are inserted into steps 1-4 of the algorithm presented in Section 3.4 for each loading step. The stress-strain graphs are fitted to the experimental data by minimizing the mean squared error, defined according to equation (3.7). The optimized material parameters for ages of 5-85 minutes are summarized in Table 3.5.

Table 3.5: Optimized material parameters for fitting the stress-strain results obtained from the microplane DP model (used in the early-age scheme) to the UUCT results of the current study.

$Age\,[min]$	$\sigma_0\ [kPa]$	α	$H\ [kPa]$	a	p	κ_0^d	$\nu\,[-]$
5	22.66	0.25	4194	2800	0.5000	3	0.496
15	22.97	0.27	4680	2910	0.5450	3	0.489
25	23.04	0.28	4710	3380	0.6500	3	0.481
35	24.35	0.33	4858	3780	0.7500	3	0.474
45	25.66	0.36	5194	3810	0.7700	3	0.467
55	26.71	0.38	5278	4100	0.7000	3	0.460
65	27.78	0.40	5411	4740	0.7200	3	0.453
75	29.27	0.43	5589	4410	0.7300	3	0.446
85	30.41	0.45	5645	4370	0.8000	3	0.440

Using these parameters, the stress-strain graphs for all ages are drawn in Figure 3.11. As seen in this Figure, the parameter optimization leads to an acceptable fit between the model predictions and the experimental results.

To implement the model with a predictive tool for assessing the buildability of early-age samples at ages for which there were no experimental results, a scheme is presented regarding the time-evolution of the material parameters of the microplane DP plasticity damage model. As it can be seen in Table 3.5, the plasticity (2^{nd}, 3^{rd}, and 4^{th} columns) and damage (5^{th}, and 6^{th} columns) parameters associated with the DP model exhibit an increasing trend with specimen aging, which can be attributed to the material hardening that occurs at higher ages. To relate the increasing trend of material parameters during the curing process, they are formulated as linear functions of the degree of cure (χ). The results are represented in Figure 3.12.

Since a full timescale is considered for the evolution of modulus of elasticity, both for the samples between the ages of 5-85 minutes and the ones at the end of one day of age, a full-scale solution for the degree of cure is obtained. Once the degree of cure are known, the material parameters (hence the microplane DP model) can also be updated for the later ages of the concrete specimens. For example, material parameters

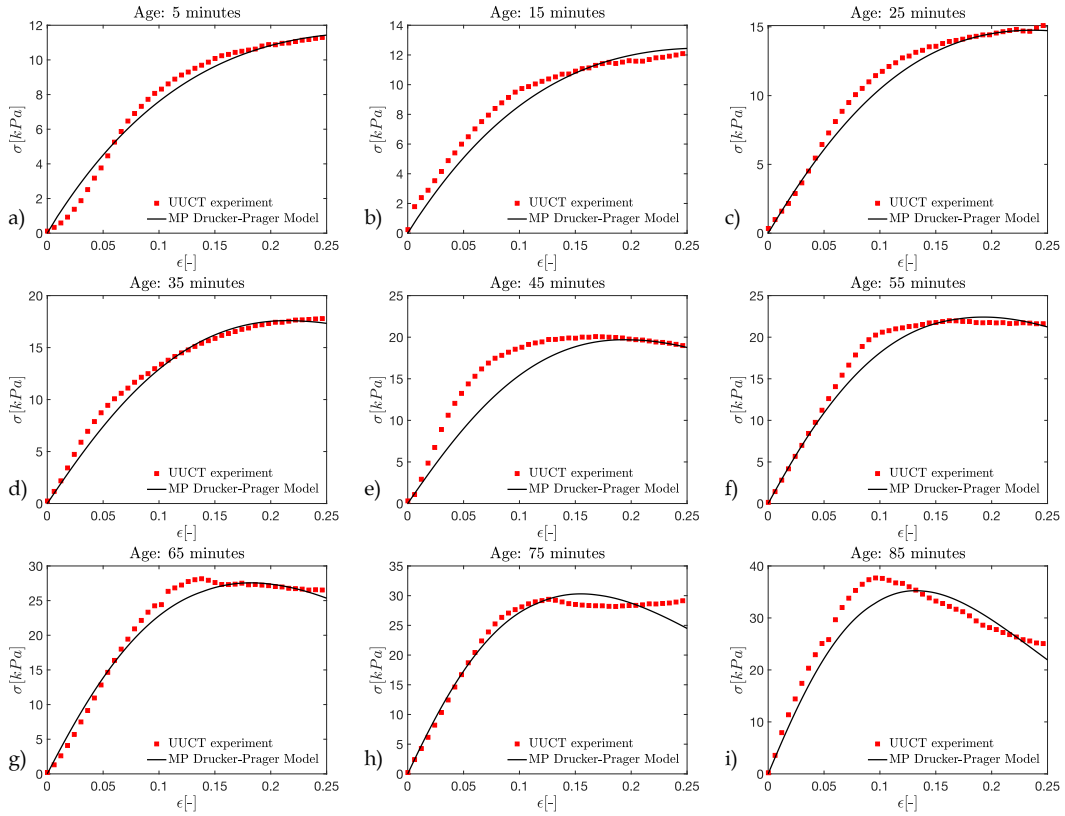

Figure 3.11: UUCT results of Section 3.1 and theoretical predictions of the stress-strain behavior of fresh concrete, when the microplane plasticity damage model developed in Section 2.1 is used in the early-age scheme.

predicted by the linear fits in Figure 3.12 are plugged into the microplane DP model for ages 90, 105, and 120 minutes, for which no experiments were conducted. The predicted compressive stress-strain results are plotted in Figure 3.13, along with the previously fitted results.

As shown in Figure 3.13, the hydration and curing processes result in increased material hardening and broader elastic regions. Moreover, the ultimate compressive stresses are increased, and their corresponding strains tend to decrease with specimen aging. Also, at older ages, post-peak softening behavior is more pronounced, which can be attributed mostly to drying or autogenous shrinkage phenomena. In the drying shrinkage, exposedness of concrete samples to an environment, with a lower relative humidity level than their original pore water content, creates a gradient that results in moisture transport from the specimens (both from interior and exterior lev-

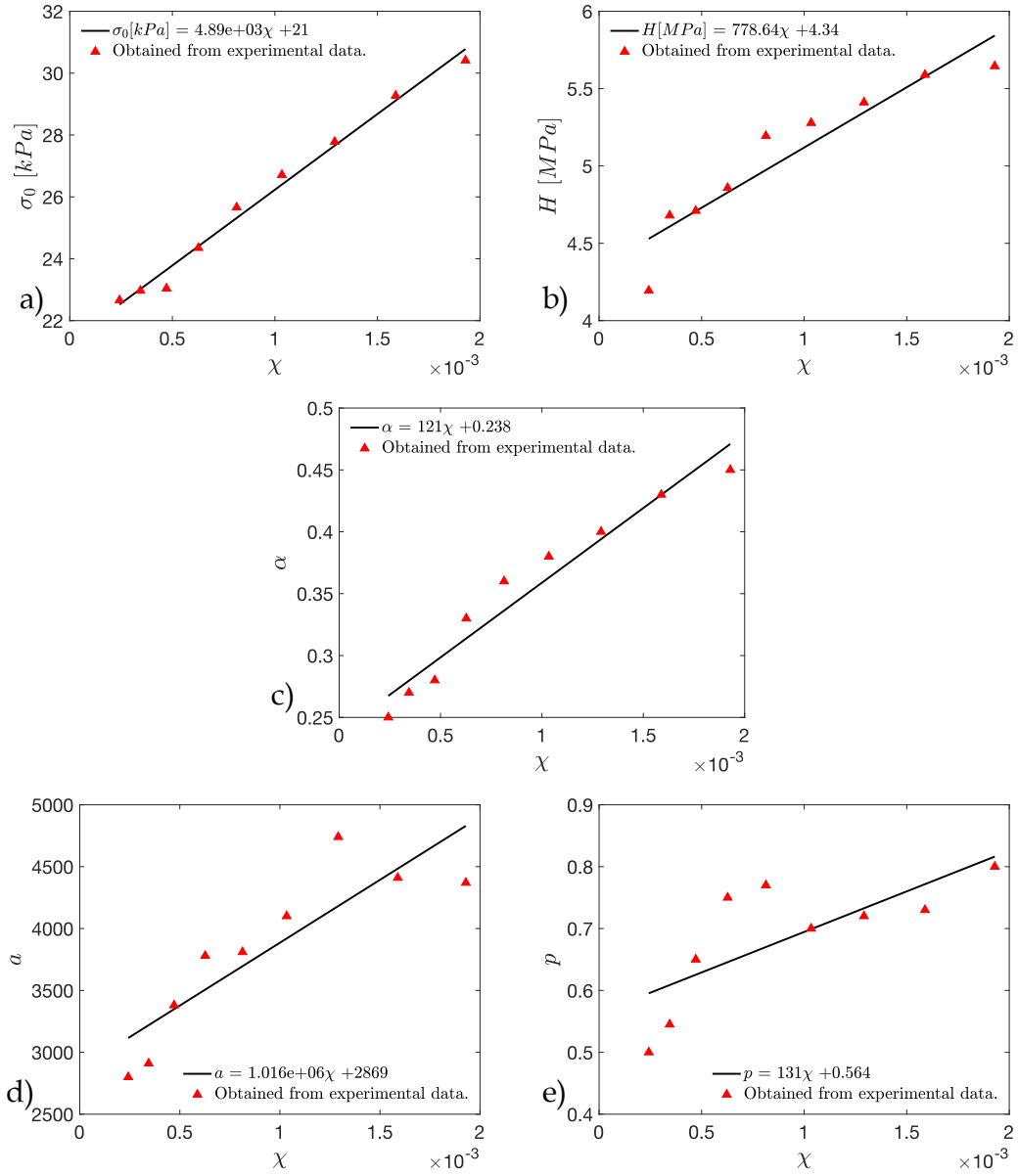

Figure 3.12: Evolution of the material parameters introduced in the microplane plasticity damage of Section 2.1 over the ages considered in the UUCT results of Section 3.1.

els) to the environment. In autogenous shrinkage, the chemical processes that occur during the advancement of the hydration process lead to the consumption of pore water content . Lower pore humidity, in turn, leads to specimens drying from their inner sections; consequently, in both shrinkage phenomena, volume decrease is generated in the aging samples during the hydration process, which can be a source of crack

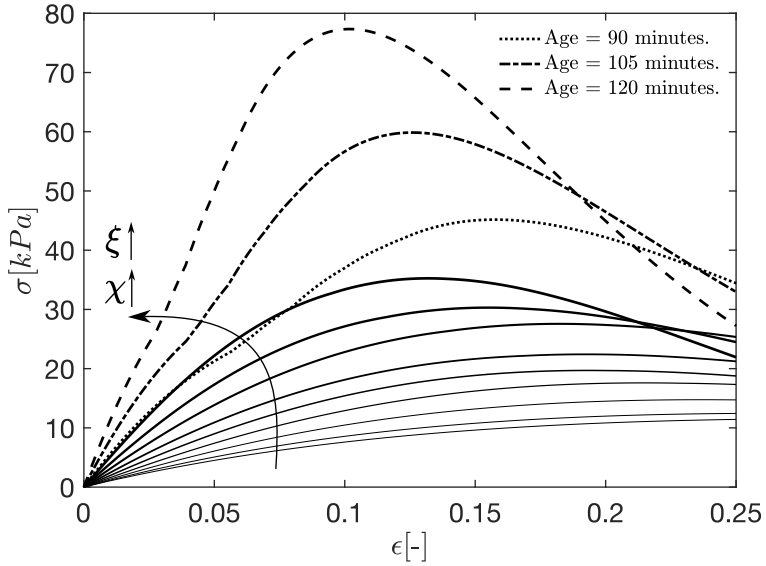

Figure 3.13: Stress-strain results from the microplane DP model for 0 to 120 minutes of age (for the ages of 90, 105, and 120 minutes the predicted results are plotted).

initiation at higher stress levels.

3.5 Incorporation of curing and hydration mechanisms into the plasticity damage model proposed by D. Feng et al. (2018)

In this section, the plasticity damage model explained in Section 2.2 is equipped with the hydration and curing kinetics of Sections3.2 and 3.3, respectively. To attain this objective, the algorithm described in Section 3.4 is utilized, with steps 1 through 4 remaining unaltered for each loading phase. However, the algorithmic treatment of the plasticity damage model, described in Section 2.2, is employed to determine the global macroscopic stress at each loading history. The formal treatment is described, in depth, in the original publication [17].

Due to the fact that the buildability model is validated against the UUCT results from Section 3.1, for the parameters α^+ and α^-, the original paper's recommendations are also accepted in this study. Since the compressive strength, and its related strain, are entered as parameters in this plasticity damage model, they are also determined for each age of the UUCT results, and are expresses as linear functions of χ. Figure 3.14

demonstrates that this assumption is supported when its predictions are compared to experimental values of f_c^- and ϵ_c^-.

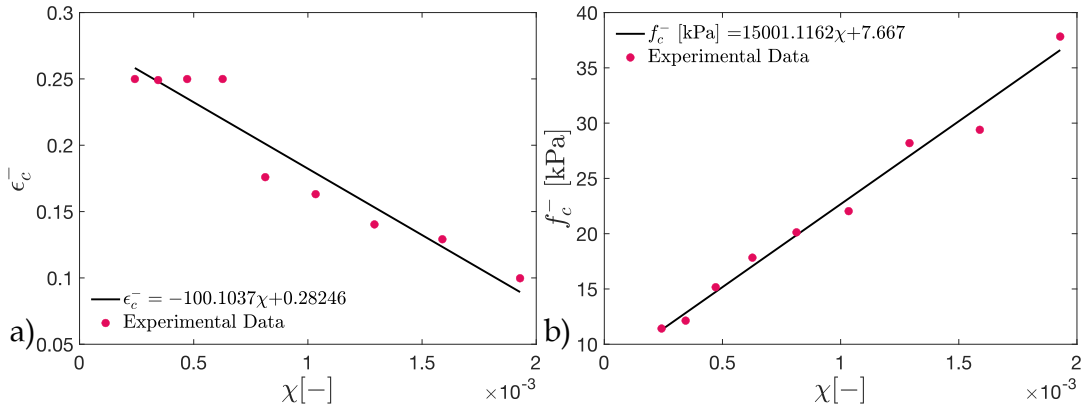

Figure 3.14: Linear evolution of the compressive strength and it's corresponding strain, obtained from the UUCT results of Section 3.1.

Following the mentioned procedure, time dependence is incorporated to the material parameters of the plasticity damage model. Figure 3.15 depicts the projected stress-strain behavior from the plasticity damage model, equipped with the curing and hydration kinetics, in comparison to the UUCT data for all ages of the experiment, and satisfactory performance is observed. Comparatively, this Figure also portrays the model predictions if, instead of the curing model, the experimental moduli of elasticity (shown in Figure 3.2) were used, and it is observed that, with the exception of 45 minutes of age, integration of the curing model does not have an unacceptable difference.

Due to the introduction of compression strengths, and their corresponding strains, as material characteristics to this plasticity damage model, integration of curing and hydration kinetics (in terms of Young's moduli and Poisson's ratio) leads to an excellent fitting performance to this model in capturing the experimental data. In addition, a small number of material parameters and empirical plasticity and damage definition, lead to improved numerical performance and reduced computational cost for this model. Nontheless, empirical plasticity and damage definitions are not always thermodynamically consistent (Unlike the model studied in Section 2.1 and the microplane-based gradient-enhanced plasticity damage model described in the next section).

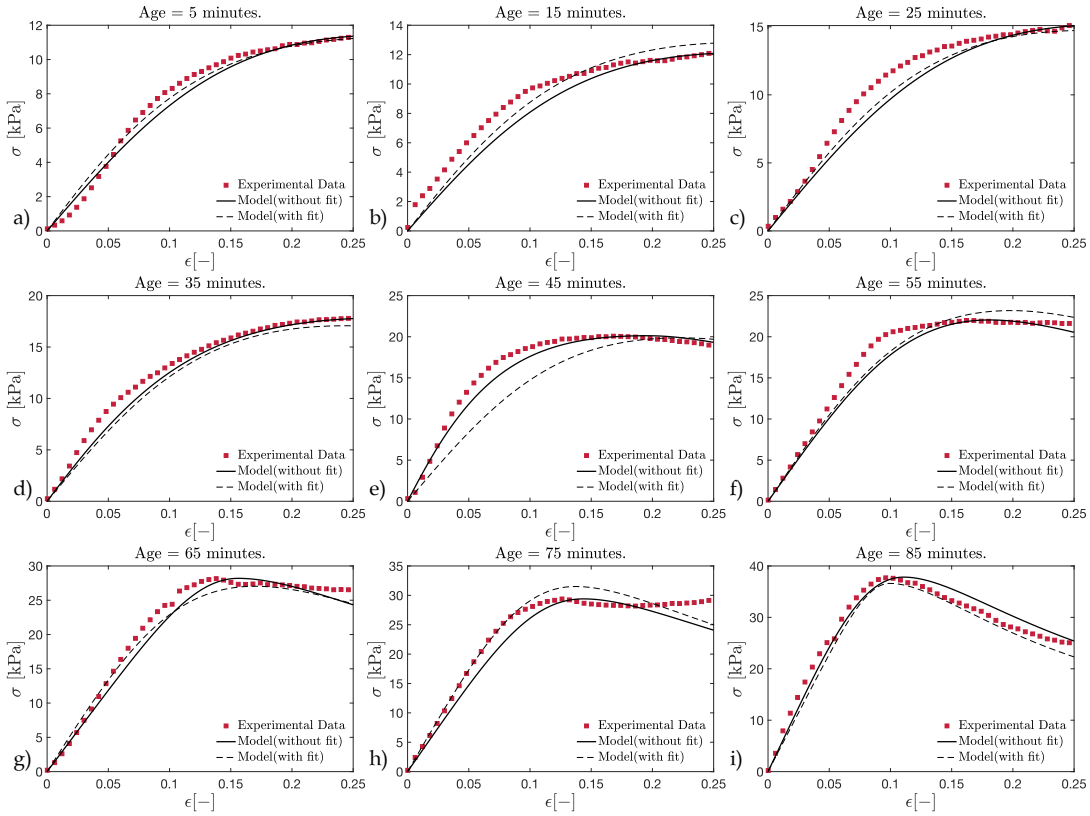

Figure 3.15: Experimental and theoretical predictions of the stress-strain behavior of early-age concrete, when the plasticity damage model proposed by D. Feng et al.[17] is used in the early-age scheme.

3.6 Incorporation of curing and hydration kinetics into the gradient enhanced microplane plasticity damage model proposed by I. Zreid & M. Kaliske (2018)

The curing and hydration kinetics are utilized to obtain a time-dependent format for the Poisson's ratios and moduli of elasticity, according to the procedures of Sections 3.2 and 3.3. Due to the theoretical resemblance between this model and the microplane plasticity damage model provided in Section 2.1, these parameters are used to construct the microplane bulk and rigidity moduli using equation (2.22). Therefore, steps 1 through 4 in Section 3.4 also apply here. The finite element formulation described in the original research [2] is utilized to determine the stress-strain relationship. Since the model is already incorporated in the most recent version of ANSYS, the curing and hydration kinetics are implemented in the APDL environment, result-

ing in time-dependent moduli of elasticity and Poisson's ratios that are supplied into the gradient-enhanced model.

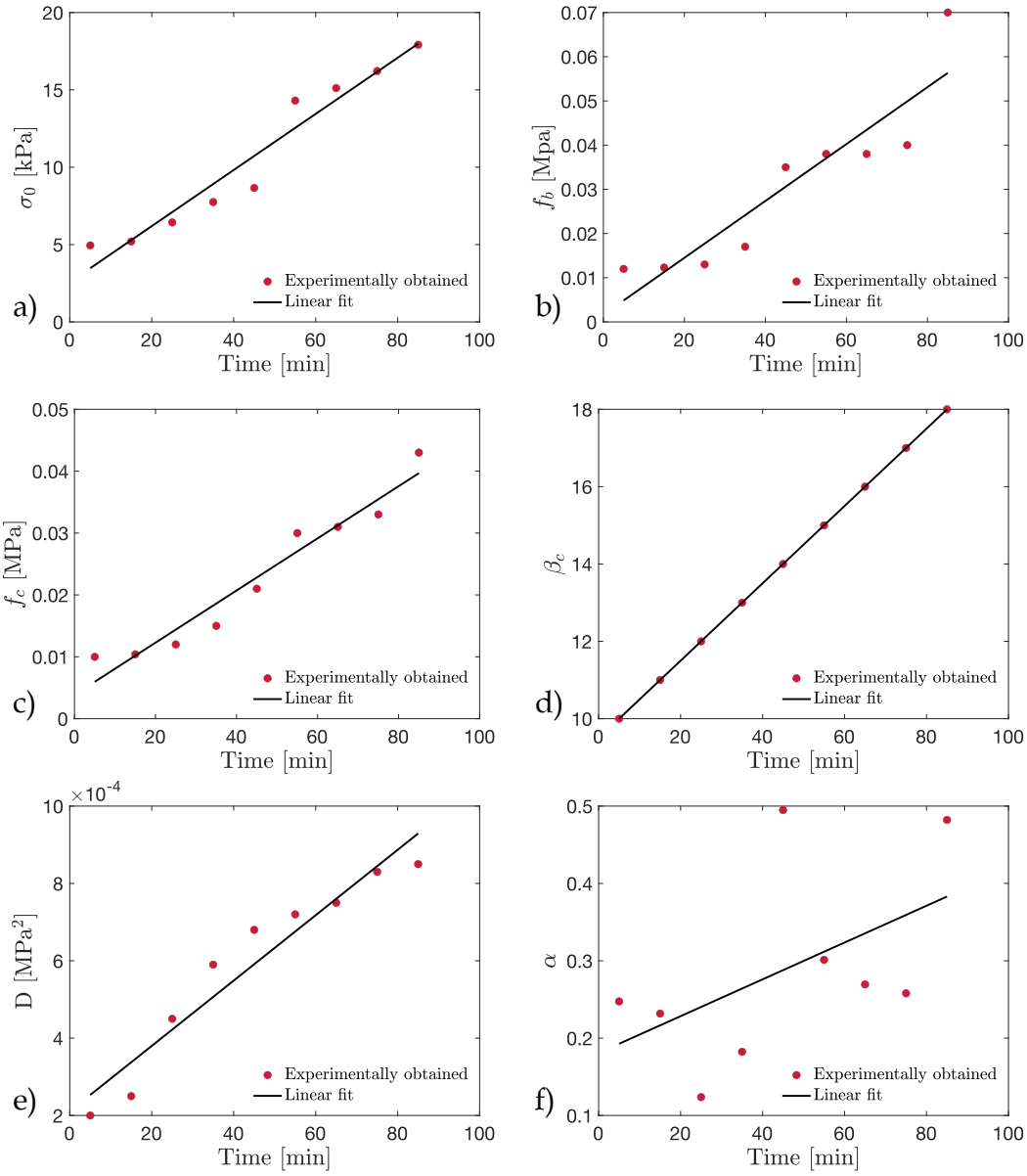

Figure 3.16: Evolution of material parameters introduced in the gradient enhanced microplane plasticity damage model in Section 2.3.

After fitting the stress-strain outputs of the model, in simulating the uni-axial compression test, to the UUCT results, via adjusting the introduced material parameters in equation (2.85), their time-dependent variations are analyzed (optimized parameters are inroduced in Table 3.6).

Table 3.6: Optimized material parameters for fitting the stress-strain results obtained from the gradient-enhanced microplane plasticity damage model of [2] (used in the early-age scheme) to the UUCT results of this study.

$Age\,[min]$	$\sigma_0\ [kPa]$	$f_b\,[MPa]$	$f_c\,[MPa]$	β_c	$D\ \left[MPa^2\right]$	α
5	4.949	0.0120	0.0100	10	2.00×10^{-4}	0.247
15	5.201	0.0123	0.0104	11	2.50×10^{-4}	0.232
25	6.433	0.0130	0.0120	12	4.50×10^{-4}	0.124
35	7.749	0.0170	0.0150	13	5.90×10^{-4}	0.182
45	8.660	0.0350	0.0210	14	6.80×10^{-4}	0.495
55	14.308	0.0380	0.0300	15	7.20×10^{-4}	0.301
65	15.114	0.0380	0.0310	16	7.50×10^{-4}	0.269
75	16.215	0.0400	0.0330	17	8.30×10^{-4}	0.258
85	17.916	0.0700	0.0430	18	8.50×10^{-4}	0.482

As depicted in Figure 3.16, a linear expression of these parameters in terms of time, gives an adequate fit against their experimental values and is, therefore, accepted for this study. Also, to account for the nature of the UUCT experiments in Section 3.1, the uni-axial tensile strength (f_t in equation (2.85)) is set to a small value of 0.0001 (approximately zero), for all of the relevant ages in the fitting process, and are not displayed in Figure 3.16. As the curing and hydration processes progress during the aging of the fresh samples, consumption of hydration products renders the samples hardened by raising their modulus of elasticity and other plasticity-related parameters, such as initial yield stress and friction coefficient. In addition, both the compressive and bi-axial strengths of the young samples show an almost linear dependency on time.

Figure 3.16 also suggests that a linear expression of damage-related material parameters in time agrees well with their experimentally obtained values, which can be understood by observing that the post-peak softening behavior becomes more prominent in aged fresh specimens.

Figure 3.17 depicts the fitting performance of the gradient-enhanced microplane plasticity damage model coupled with the linear time-evolution scheme of its material pa-

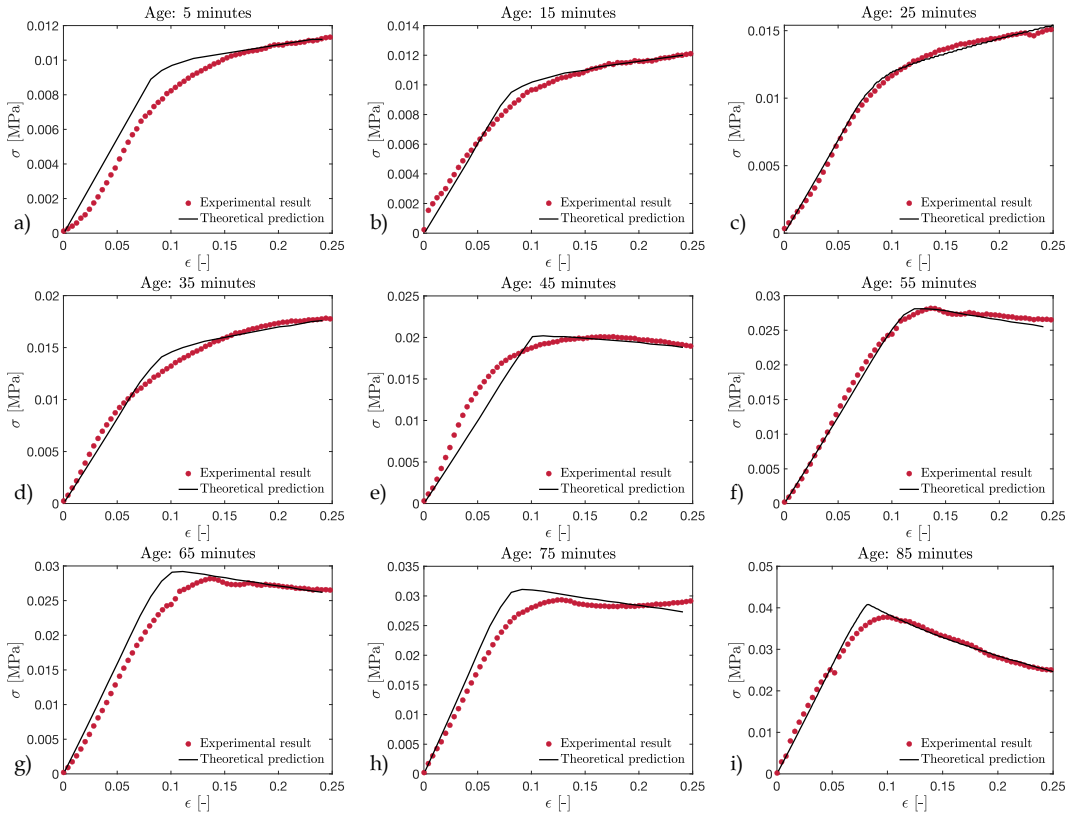

Figure 3.17: Experimental and theoretical predictions of the stress-strain behavior of fresh concrete, when the plasticity damage model proposed by I. Zreid & M. Kaliske [2] is used in the early-age scheme.

rameters for the ages considered in the UUCT experiments, and as can be observed, an excellent agreement is attained. Nevertheless, due to the well-known mesh-sensitivity attributed to microplane models, choosing the correct element-size and solution time-step makes this approach more adept at fitting and less numerically flexible. However, due to its thermodynamically consistent derivation, the physical meaningfulness of the model and its associated parameters are ensured. Lastly, the model is utilized to simulate the UUCT test setup for each age, allowing for the observation of the radial displacement distribution at the completion of the displacement-controlled compression test (Figure 3.18).

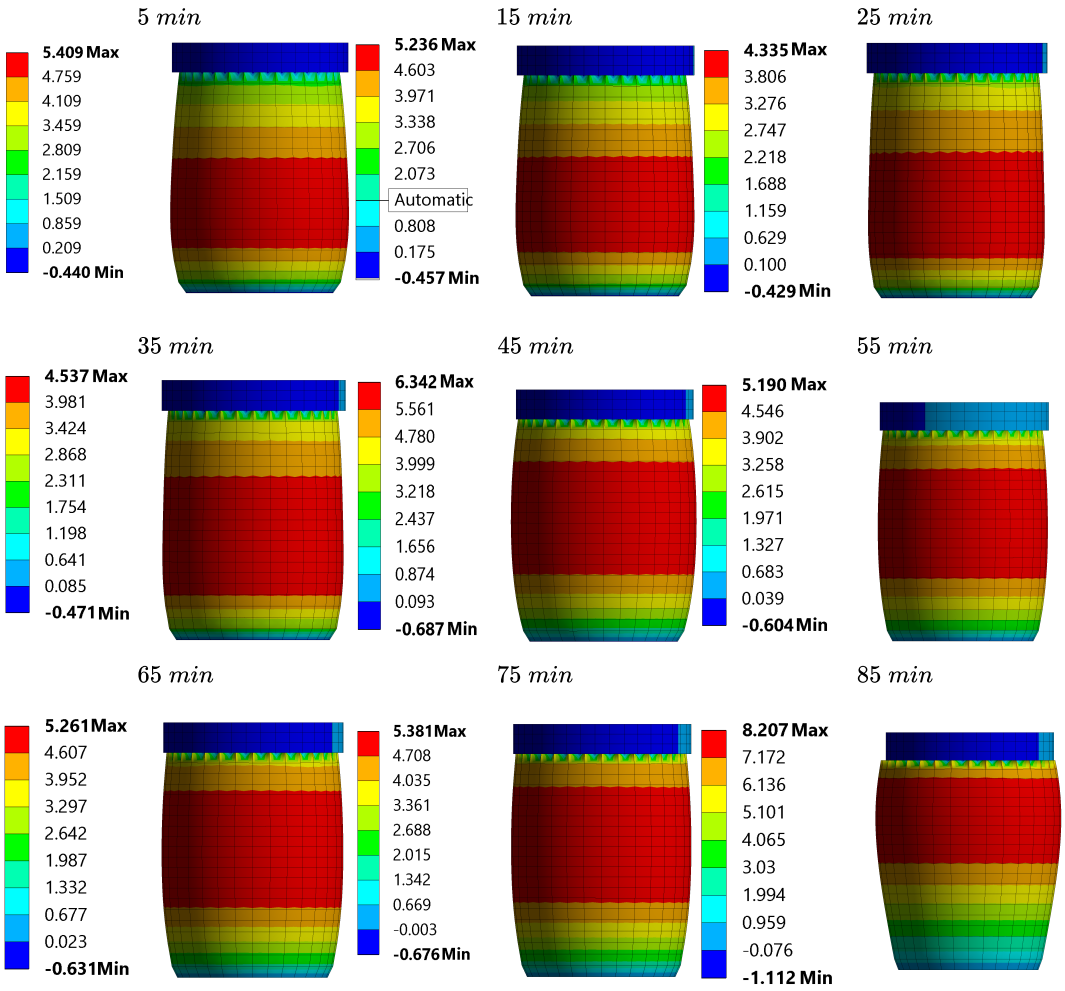

Figure 3.18: Simulation results of the unconfined uni-axial compression tests of Section 3.1 (the radial displacements are in mm).

3.7 Examples of numerical simulations

In this section, the coupling of the mathematical frameworks for early-age concrete hydration and curing kinetics (which led to the determination of E and ν) with the gradient-enhanced microplane plasticity damage model (as described in Section 3.6) is used to to produce a time-evolving stress-strain behavior of the early-age printed specimen; this scheme, in turn, results in obtaining the deformation of various 3D printed structures under their own weights. The following step involves integrating the printing process and its related parameters.

3.7.1 Continuous time-dependency assumption

To begin with, it is assumed that the printing process occurs in a continuous manner, with printer setup delays between layers being ignored. The time required to print one layer is dependent on the layer thickness, the shape of the printed cross section, and the printing speed (v_p). Three common geometries are chosen as control subjects of the numerical simulations: prismatic structures with a) cylindrical, b) rectangular, and c) square cross-sections. For each cross-section, the printing time for one layer is obtained from considering the printing speed and periphery of the cross-section, calculated from the cross-section mid-line.

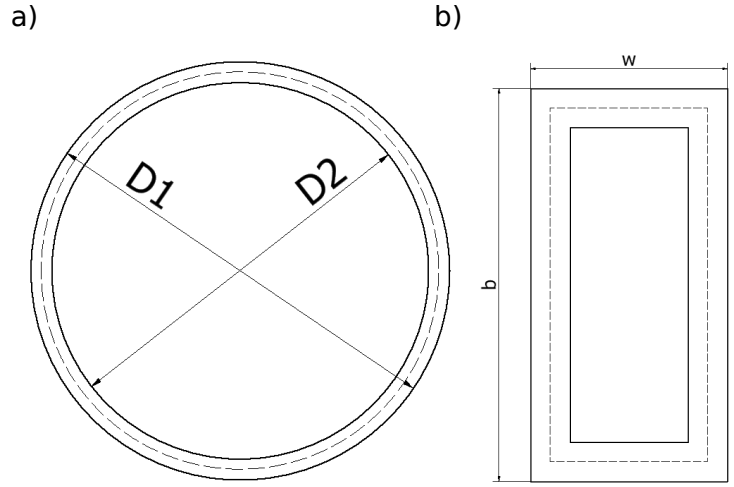

Figure 3.19: Mid-line definition for a) circular and b) rectangular cross-sections with layer-thicknesses of t_{lt}.

Figure 3.19 represents a general cases of circular (dimension of D_1 and D_2) and rectangular (dimensions: $w \times b$) cross-sections. For a printing speed of v_p and layer width of t_{lw}, the printing time (t_p) for one layer can be calculated according to the following.

$$t_p = \frac{\text{mid-line periphery}}{v_p} = \begin{cases} \frac{\pi(D_1+D_2)}{2v_p} = \frac{\pi(D_1-2t_{lw})}{2v_p} & \text{Circular cross-section,} \\ \frac{2(w+b-2t_{lw})}{v_p} & \text{Rectangular cross-section.} \end{cases} \tag{3.8}$$

Moreover, if printing of one layer takes t_p amount of time, at the onset of printing the second layer, the first layer is aged t_p, and when printing of the second layer is

completed (hence its age is t_p), the first layer is aged $2 \times t_p$, and so forth. By analogy, at the end of printing n layers, the last layer is aged t_p, and the first layer is aged $n \times t_p$.

Moreover, a mathematical framework is needed for transforming the aforementioned aging scheme to a continuous age-change format in the vertical (i.e. y) direction. Considering n_{layers} to be the total number of layers to be printed with a constant thickness of t_{lt}, the following form is proposed for obtaining the particular age $t(y)$ at a general vertical coordinate of y:

$$t(y) = t_p \left(n_{layers} - \frac{y}{t_{lt}} \right). \tag{3.9}$$

The following presumptions are a priori held in the suggested formulation of equation (3.9):

1. The cross-sectional material properties of each horizontal slice of the printed structure are constant.

2. The formulation assumes a constant printing speed throughout the printing process (in accordance with equation (3.8)).

3. In the formulation, t_p is assumed to be constant; hence, the formulation is supplied for printing prismatic structures (i.e. constant cross-sections in the vertical direction).

4. At a general height of y, the cross-sectional age is assigned in a step-wise (not gradual) fashion.

The form presented in equation (3.8) provides a mean to simulate the printing process as a continuous stacking of layers in the vertical direction, each of which is assigned an age according to equations (3.8) and (3.9). Denoting the minimum printing time as $t_0 (= t_p)$ (for this study, properties of $5\,min$ specimen from the UUCT results are assigned for this age), and maximum age as t_{max}, the configuration of linear age change is represented in Figure 3.20.

The age of each layer is considered as the time at which χ and ξ (from Sections 3.2 and 3.3) are evaluated, to be the subjects of either plasticity damage model mentioned in Section 2.3. This format provides a means for incorporating and assessing the effects of significant parameters in the 3D printing of concrete, such as printing speed,

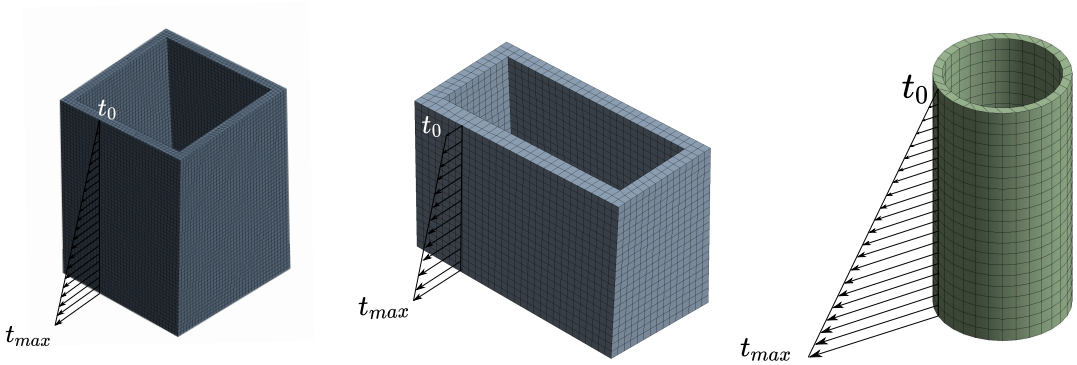

(a) (b) (c)

Figure 3.20: Vertical change of layer ages, defined as linearly decreasing with height, for prismatic structures with a) square, b) rectangular, and c) circular cross-sections.

cross-sectional geometry, nozzle type (t_{lt}), number of layers to be printed, and layer thickness, on the buildability phenomenon.

3.7.1.1 Constant layer-thicknesses

In this section, the numerical simulations are conducted for obtaining induced displacements under self-weight loads of 3D printed prismatic structures with material properties of Section 3.1, having circular (Figures 3.21 and 3.22), rectangular (Figures 3.23 and 3.24), and square (Figures 3.25 and 3.26) cross-sections. In performing the simulations, it is assumed that the layer thickness in the printing process remains constant (a value of 10 mm is selected), and instead, the number of printed layers vary between 20, 30, and 40 for each configuration. Moreover, for each of the cross-section types, three representative dimensions are selected. Also, to see the effects of printing setup on the buildability, the nozzle heads and printing speed are also held as analysis variables for each cross-sectional configuration. For the square and rectangular cross-sections, three circular nozzle heads with diameters of 40 mm, 45 mm, and 50 mm are assigned, since the most common nozzle tips in practical use are circular in shape, and range between 40-50 mm in size [45]. For the circular cross-section, the tip diameters 20 mm, 22.5 mm, and 25 mm are allocated in order to see the impacts of smaller nozzle tips on buildability. All simulations are repeated at printing speeds of 10 mm/s, 50 mm/s, 80 mm/s, and 100 mm/s. In order to account for defects of print-

ing process, a small rotation with a final magnitude of 3° is applied and dispersed over the height of the rectangular and square prism structures to slightly perturb the initial configuration. Within this set-up, the following observations are made:

1. An increase in the printing speed, results in more pronounced lateral (radial, in the case of a cylindrical prism) and vertical deformations for all prismatic configurations.

2. For all prismatic configurations, the impact of nozzle tip diameter appears to be stronger on cross-sections with larger dimensions. In addition, smaller nozzle heads result in more severe lateral/radial and vertical deformations.

3. For a given cross-section (i.e., moving along a column in Figures 3.21–3.26), increasing the number of printed layers corresponds to larger lateral/radial and vertical deformations in all of the studied geometries.

4. Increasing the printing speed results in increased lateral/radial and vertical deformations for all examined configurations. However, beyond a certain printing speed, the self-weight-induced deformations appear to attain a plateau, after which the deformations do not seem to change significantly; hence, along with other considerations, such as adequate layer adhesion, energy consumption of the printing equipment and its constraints, and the workability of the mixture, this fact should be considered when optimizing printing speed for the entire process.

5. For the same number of printed layers (i.e. horizontal movement in Figures 3.21–3.26), larger cross-sections result in greater vertical and lateral deformations, which can be attributed to a greater magnitude of self-weight loads.

6. Considering the lateral deformations in prisms with square cross-sections, due to the symmetry of the structures, equal self-weight-induced deformations in the x and y directions are observed, hence only one of them is presented in Figure 3.25. However, for the case of rectangular cross-sections, different deformations are observed and they are differentiated in Figure 3.23. It is worth noting in the same Figure that for smaller cross-sections, the deformations in the y direction are slightly higher than those in the x direction and as the cross-sections increase, the difference is reduced.

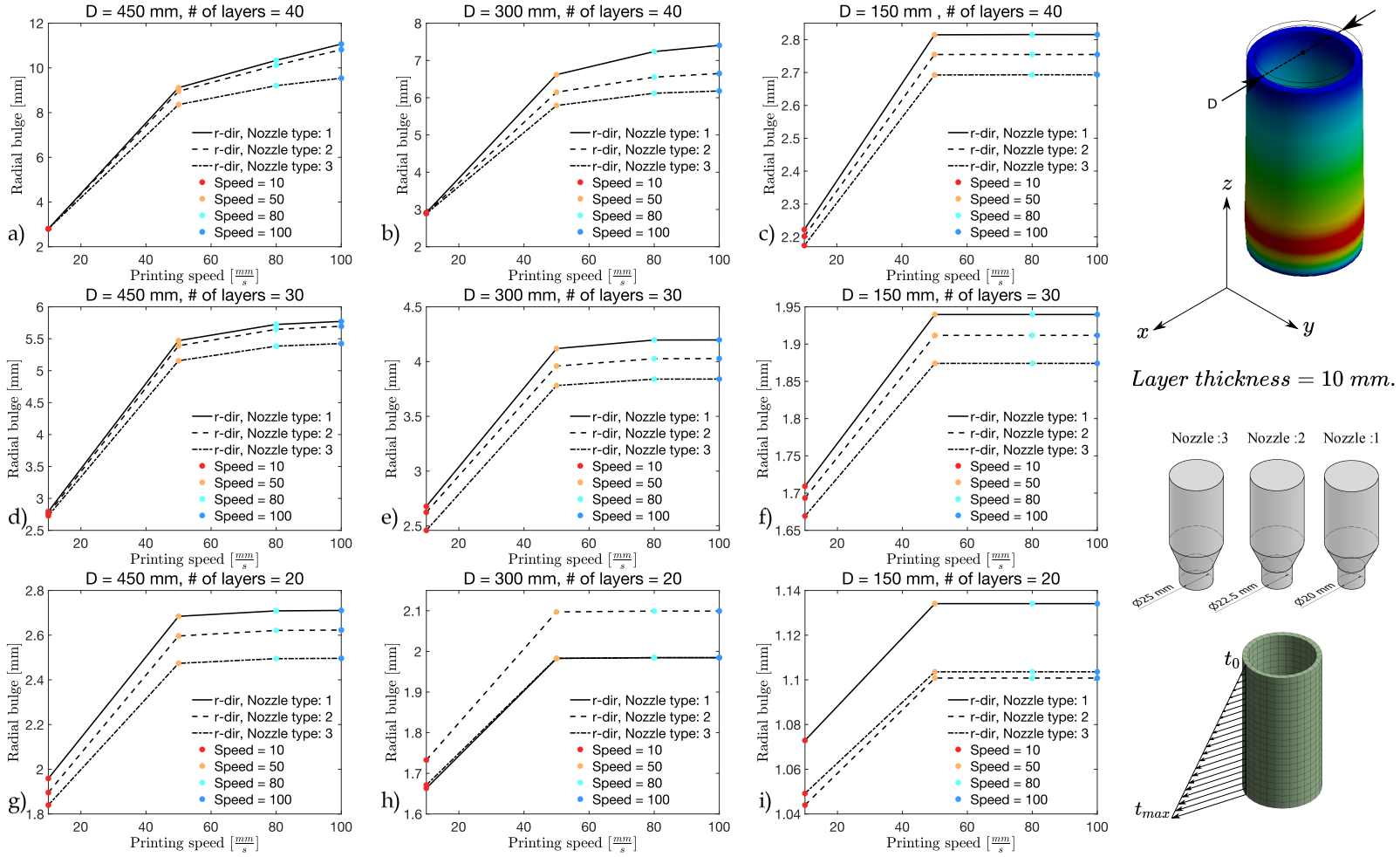

Figure 3.21: Simulation results of radial deformations for a printed prismatic cylindrical specimen (with constant layer thickness), assuming a linear vertical decrease in material age.

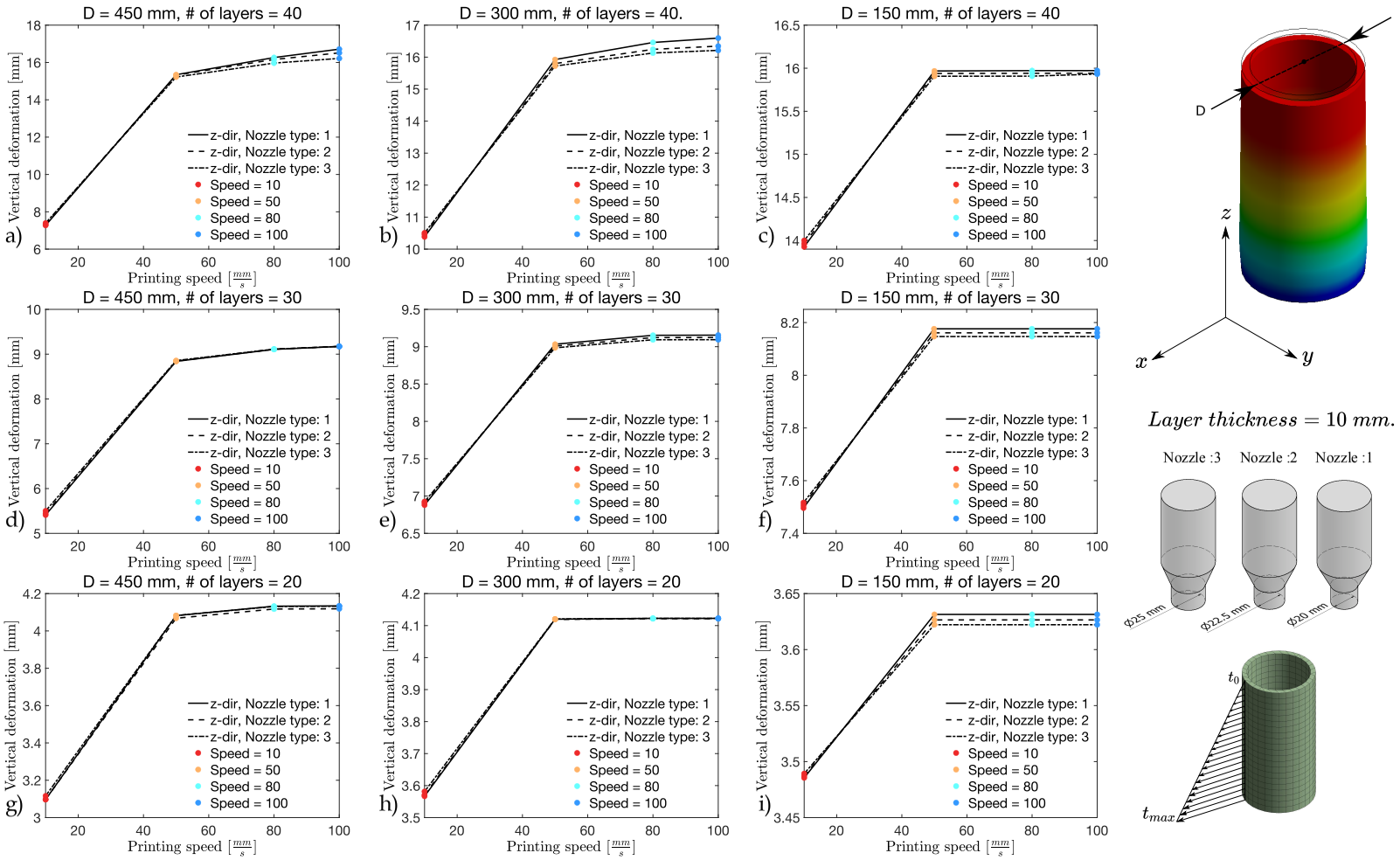

Figure 3.22: Simulation results of vertical deformations for a printed prismatic cylindrical specimen (with constant layer thickness), assuming a linear vertical decrease in material age.

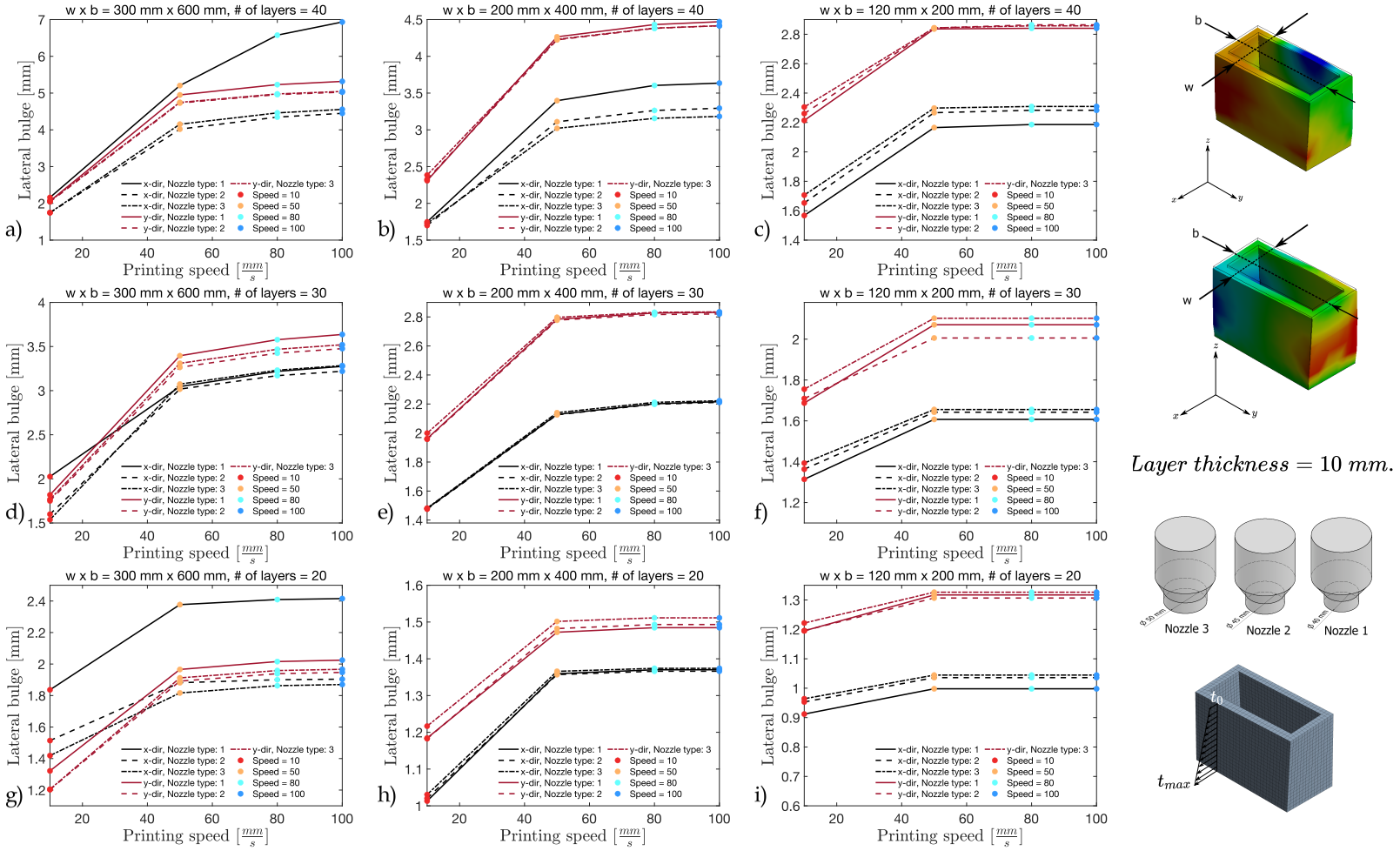

Figure 3.23: Simulation results of lateral deformations for a printed rectangular prismatic specimen (with constant layer thickness), assuming a linear vertical decrease in material age.

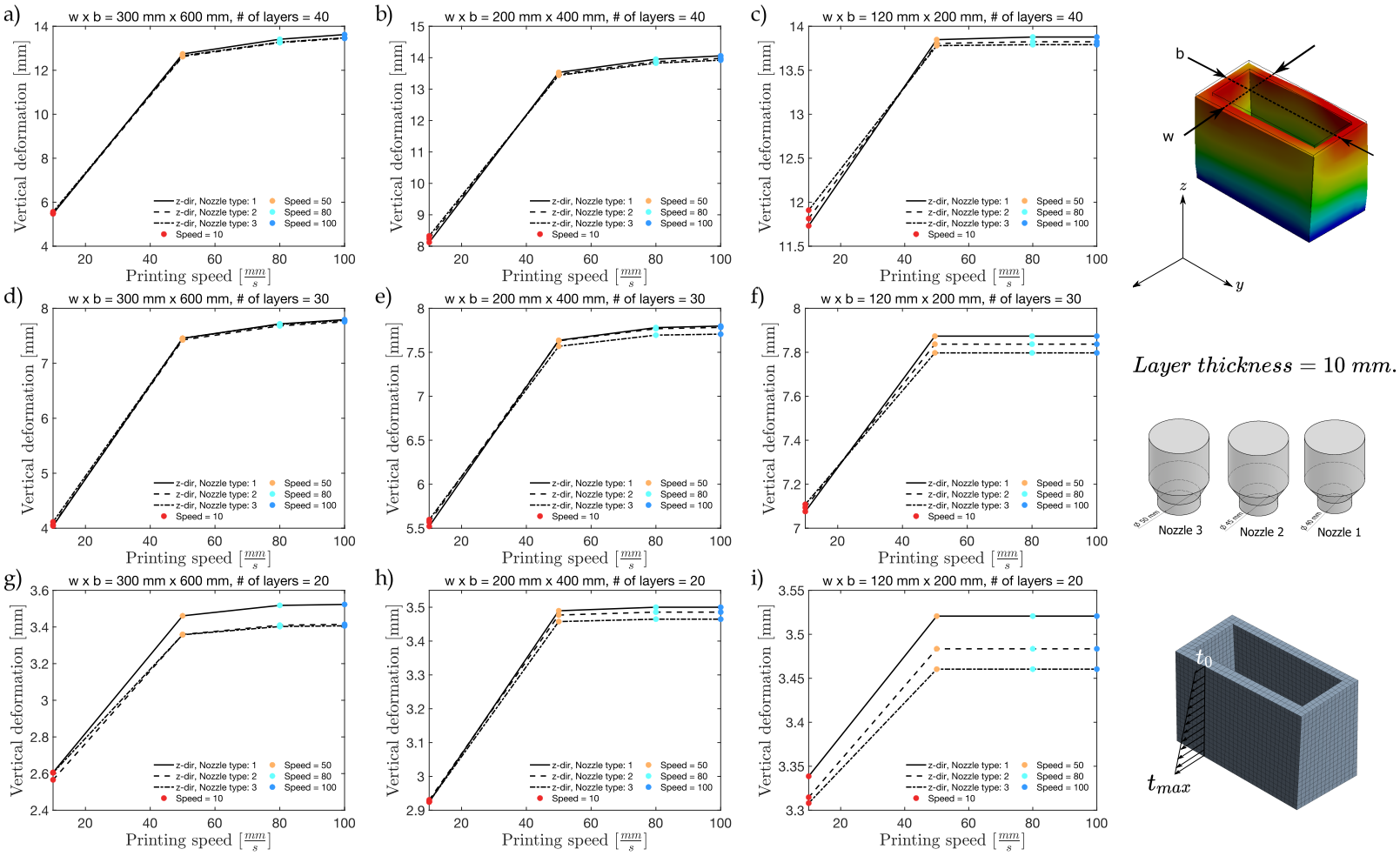

Figure 3.24: Simulation results of vertical deformations for a printed rectangular prismatic specimen (with constant layer thickness), assuming a linear vertical decrease in material age.

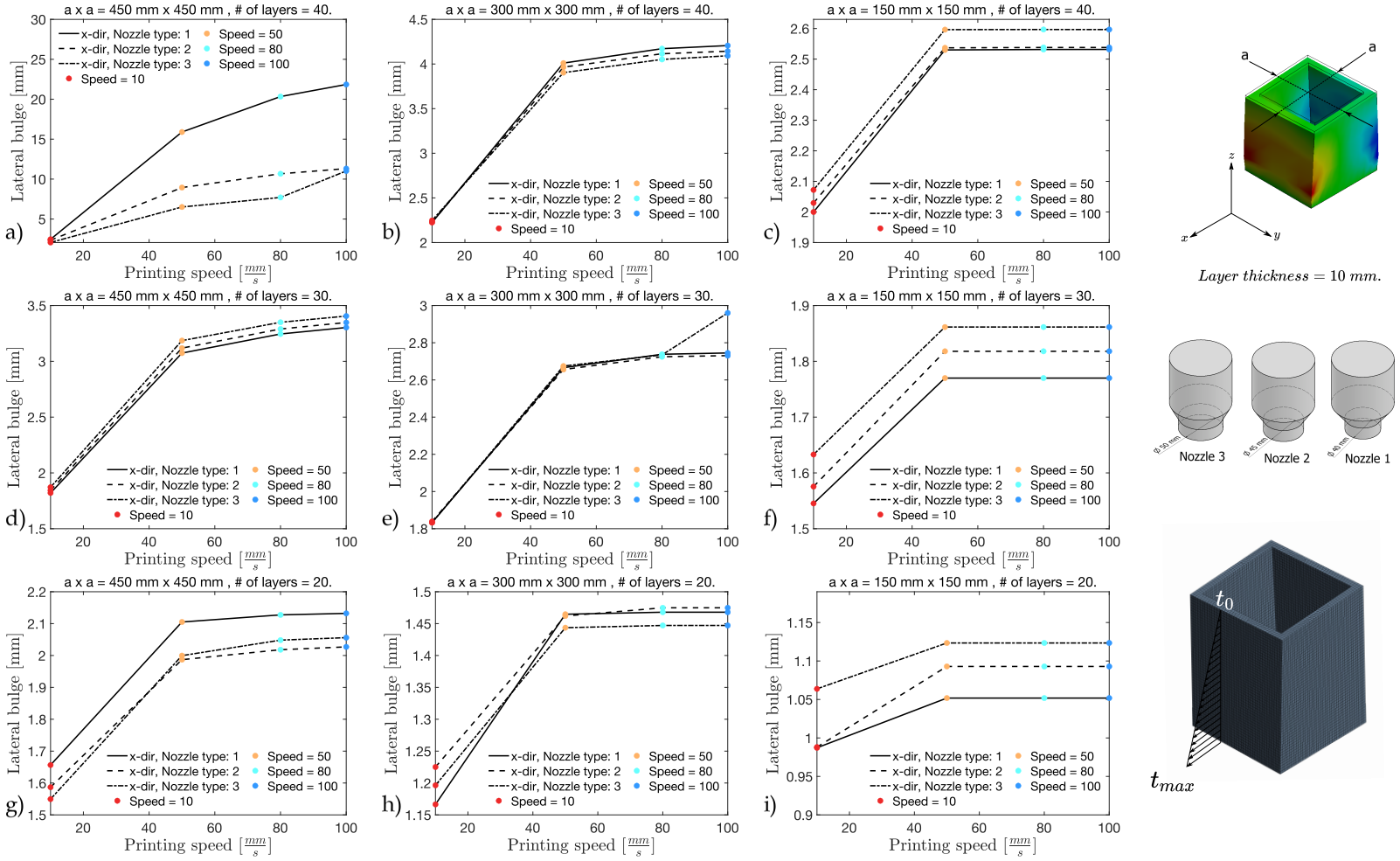

Figure 3.25: Simulation results of lateral deformations for a printed square prismatic specimen (with constant layer thickness), assuming a linear vertical decrease in material age.

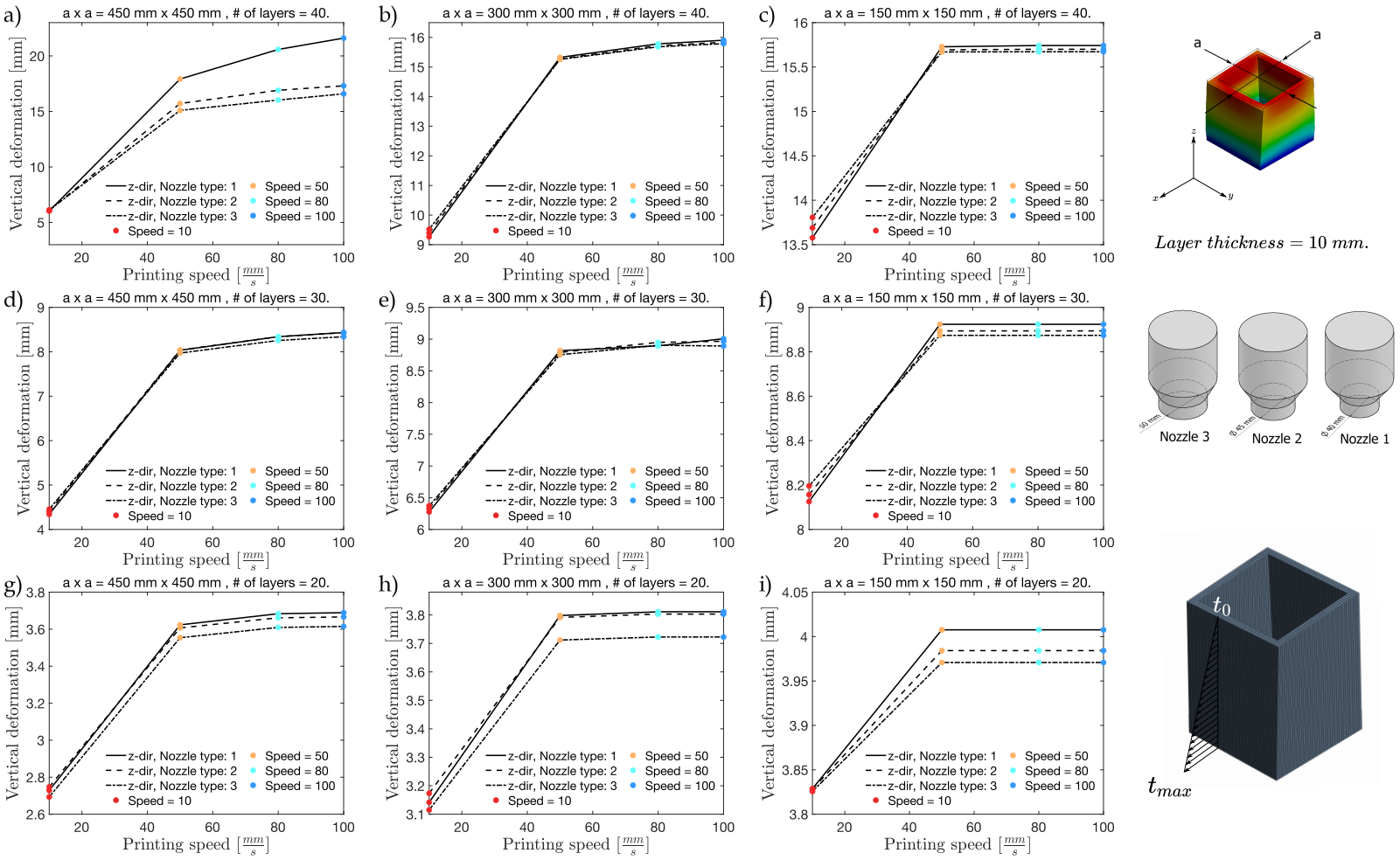

Figure 3.26: Simulation results of vertical deformations for a printed square prismatic specimen (with constant layer thickness), assuming a linear vertical decrease in material age.

3.7.1.2 Variable layer-thickness

Unlike the treatment of Section 3.7.1.1, in this Section, the buildability effects of layer thickness, and printing speed are considered for geometries with obtained material properties of Section 3.1. Similar to the previous configurations, self-weight-induced lateral/radial and vertical deformations for three prismatic 3D printed structures with circular (Figure 3.27), rectangular (Figure 3.29), and square (Figure 3.28) cross-sections are examined. In these simulations, both the total height and the cross-sections of the aforementioned geometries stay unchanged (that can be found for each analysis case on its relevant Figure). Each setup considers printing at speeds between 0-80 mm/s with layer thicknesses of 5 mm, 7.5 mm, 10 mm, 12 mm, 18 mm, and 25 mm. Similar to the analysis steps of Section 3.7.1.1, the imperfections of the printing process and structural defects (for example improper layer bonding) are introduced in terms of gradual rotation of 3° over the heights of the prismatic structures with square and rectangular cross-sections. The results of the performed numerical simulations suggest the following:

1. For a given printing speed and configuration, more lateral/radial and vertical deformations are seen as the layer-thickness increases throughout the board. This can be understood as follows: when printing with thicker layers, more material is deposited at each step, necessitating more time for the material to cure, whereas in printing of thinner layers, less material is deposited at each step, providing more time for the material to cure, resulting in less total deformation.

2. For all examined geometries, the effect of layer-thickness on lateral/radial and vertical deformations becomes less significant at very large and very slow printing speeds. When the printing speed is too slow/fast, the entire printed structure is cured/uncured; hence, the effect of layer thickness on lateral/radial or vertical deformations is insignificant.

3. Increasing the printing speed for a given layer thickness results in more lateral/radial and vertical deformations. Since a faster printing speed leads to the deposition of more fresh material, for which the curing process causes greater deformations.

4. As printing speed increases, the disparity between vertical and lateral deformations increases for all configurations (vertical deformations being larger in magnitude).

5. Regarding lateral deformations of the rectangular cross-section, deformations in the y direction are greater than those in the x direction.

6. When the printing speed is either too slow or too fast, the self-weight-induced lateral/radial or vertical deformations converge to a similar value in all studied configurations. For each configuration, two different analyses are conducted in which the entire geometry is assigned with the material properties of the earliest (5 minutes) and oldest (85 minutes) specimens from the UUCT tests. It is noted that the convergent deformation (true in both lateral/radial and vertical situations) at the fastest and slowest printing speeds is equal to the deformation if the geometry was comprised exclusively of the earliest or oldest specimens, respectively. Therefore, the two extreme scenarios serve as asymptotes for buildability analysis and subsequent printing speed optimization strategies.

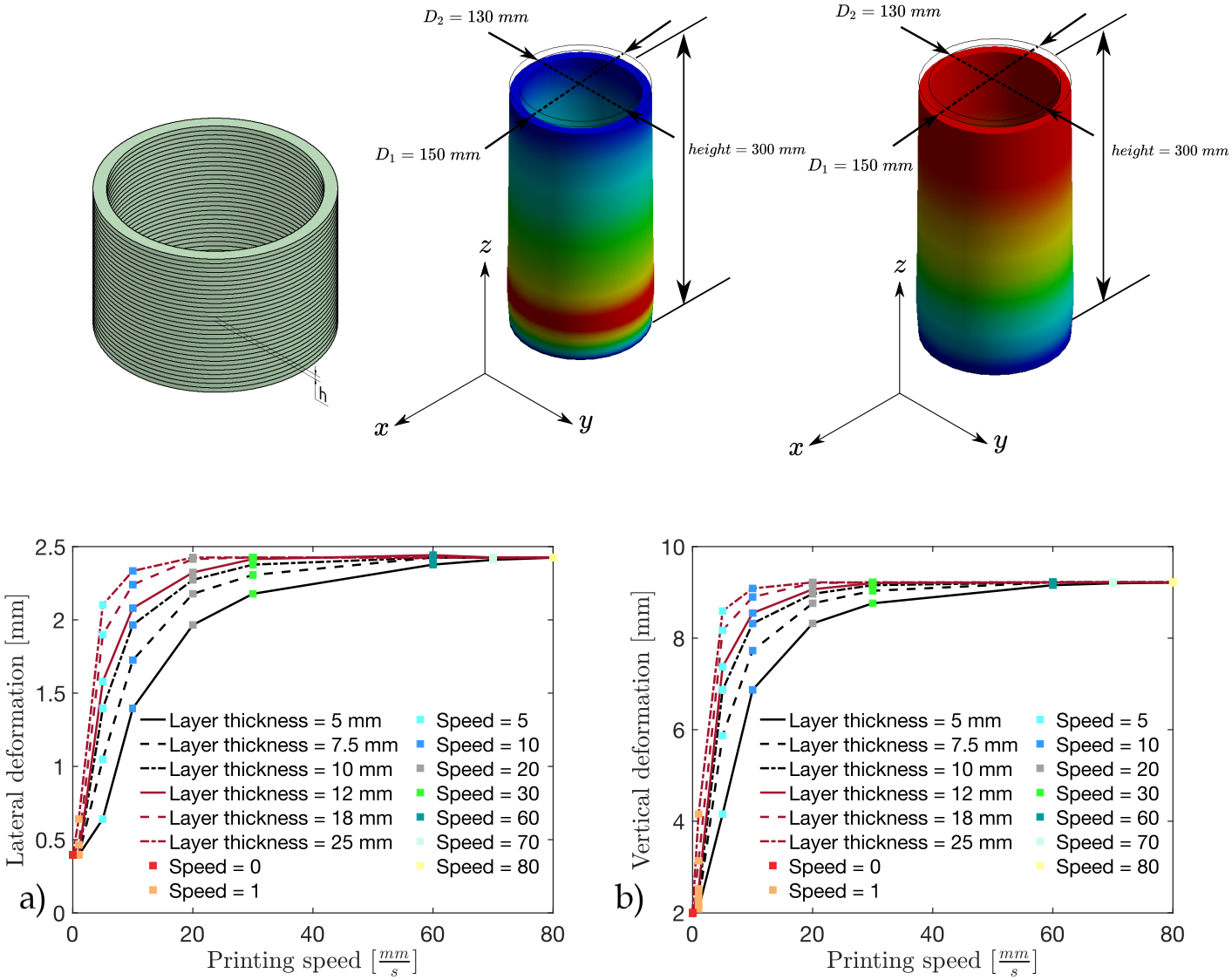

Figure 3.27: Simulation results of vertical and radial deformations for a printed prismatic cylindrical specimen (with differing layer thicknesses), assuming a linear vertical decrease in material age.

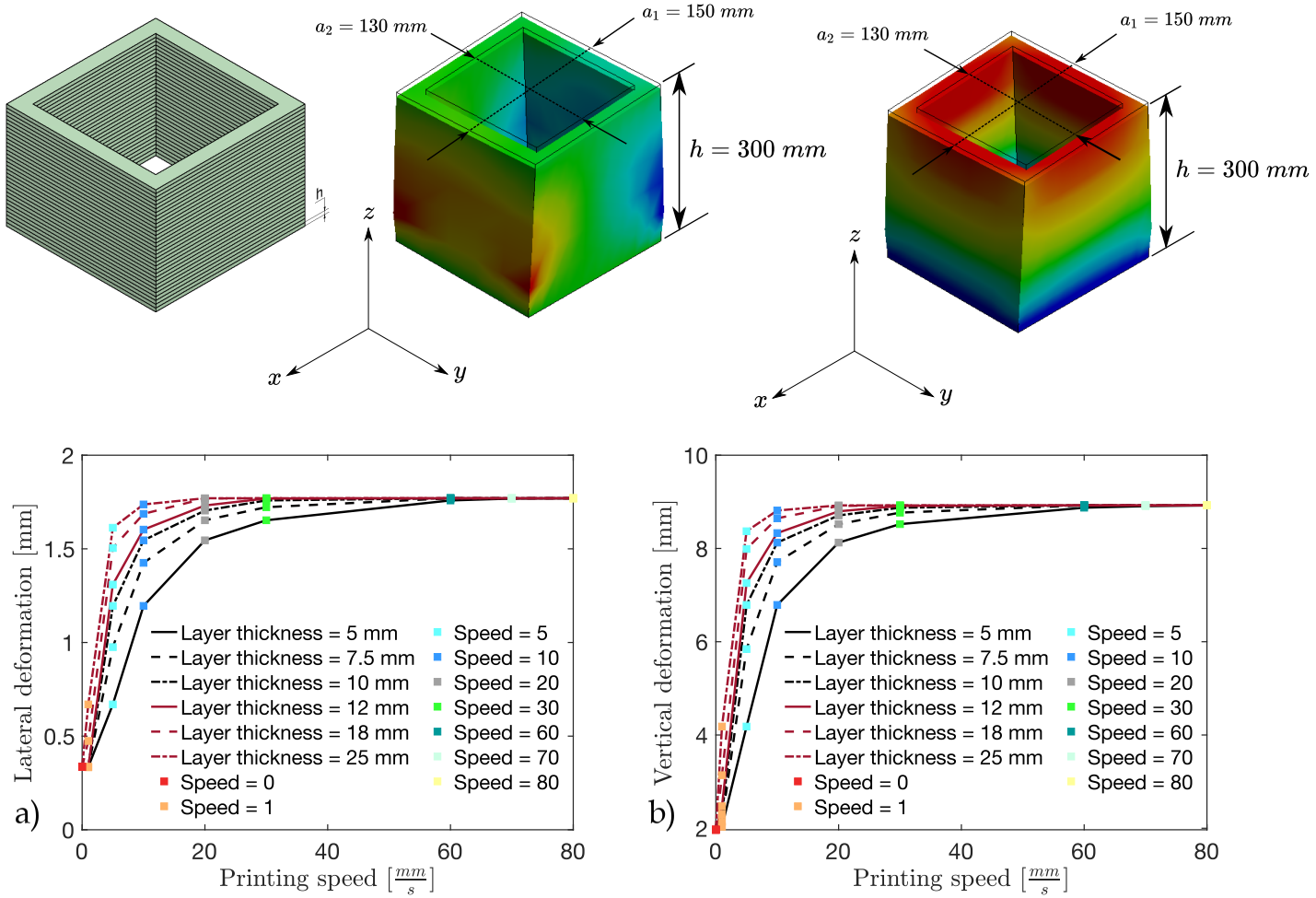

Figure 3.28: Simulation results of vertical and lateral deformations for a printed square prismatic specimen (with differing layer thicknesses), assuming a linear vertical decrease in material age.

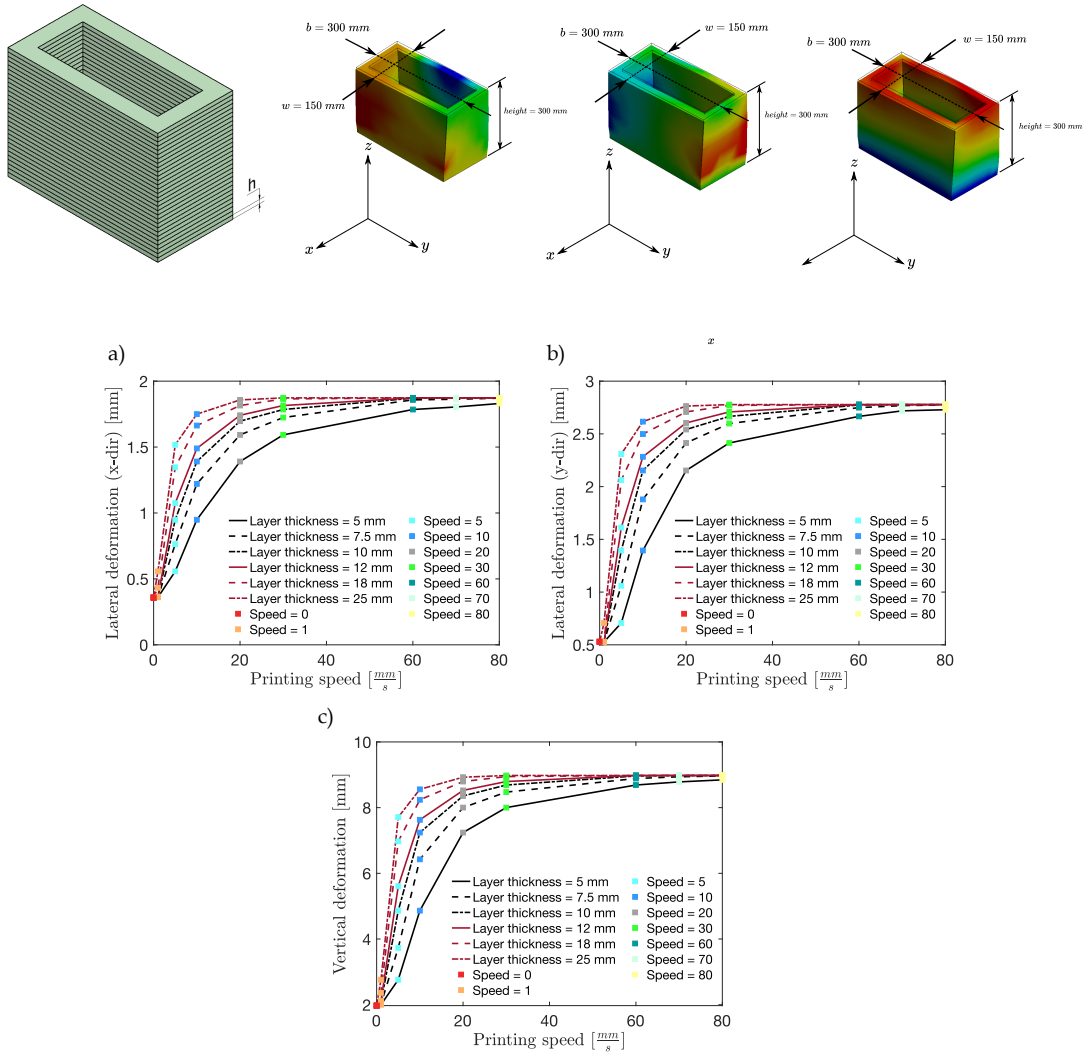

Figure 3.29: Simulation results of vertical and lateral deformations for a printed rectangular prismatic specimen (with differing layer thicknesses), assuming a linear vertical decrease in material age.

3.7.2 Simulations of a real-life printed example

In this part, numerical simulations are performed to evaluate the buildability of a column printed by İSTON Inc. as a structural member of a 3D printed house in Istanbul. In each printing phase, the column geometry contains square cross-sections with a small rotation angle, as shown in Figure 3.31. For numerical simulations of this instance, it is assumed that the specified geometries are comprised of the same mixture with which the UUCT tests of Section 3.1 were examined, and the material properties of the geometry are assumed to be consistent with this assumption. Moreover, continuous linear change of material age in the vertical direction, as a function of height, printing speed and cross-sectional geometry, is accounted for (as outlined in Section 3.7.1). The layer width and thickness of the printed structure are maintained at 35 mm and 10 mm, respectively, in accordance with the printed structure's dimensions. For the geometry of the simulated structure to match the geometry of the printed structure as closely as possible, a CAD model is made for each printed layer, based on inspections of the 3D printed result. Figure 3.30 includes technical drawings for the three layers with square cross-sections, used in the numerical simulations. In order to determine the effects of various parameters on buildability, numerical studies are performed on printing rates of 5, 20, 30, and 100 mm/s. In addition, due to the twisting nature of the printed structure, three angles of twist (AOT) with magnitudes of 0.5, 1, and 1.5 degrees are investigated for each configuration. Finally, simulations of configuration are repeated for a total of 90, 60, and 30 printed layers. Figures 3.32 and 3.33 depict simulation results for the lateral and vertical deformations, respectively. Considering the numerical outcomes, the following observations are made:

1. In all of the examined setups, increased printing speed leads to greater vertical and lateral deformations for a fixed cross-section. This is because a greater volume of material with a younger age undergoes greater deformations induced by its own weight during the curing process when the printing process is performed at higher speeds.

2. In assessing lateral or vertical self-weight-induced deformations, increasing the cross-section of the printed layers leads to bigger lateral and vertical deformations if the number of printed layers is held constant (which corresponds to a

horizontal movement on Figures 3.32 and 3.33).

3. In addition, moving along a particular column in Figures 3.32 and 3.33, provides a comparative examination of the produced lateral or vertical deformations for a fixed cross-section. Evidently, as the number of printed layers increases, so do the deformations, which can be explained by the fact that a greater mass of material on top of each layer during the printing process causes a greater weight load on the bottom layers, which in turn causes greater deformations during the curing process.

4. Induced lateral and vertical deformations exhibit a convergent behavior in all examined setups at both low and high printing rates (similar behavior was observed in sections 3.7.1.1 and 3.7.1.2, and the explanations contained therein apply to this circumstance, as well).

5. Taking into account the induced deformations in all of the investigated configurations, larger AOTs result in greater deformations (true both in lateral, and vertical cases). Moreover, as the number of layers grows, so does the influence of AOT. This can be explained as follows: for a larger AOT, a typically printed layer has a slightly smaller overall support area on its bottom side compared to when it is printed with a lower AOT; therefore, for equal weight forces, the reduction in the aforementioned area leads to greater weight-induced stresses, which in turn cause greater lateral and vertical deformations.

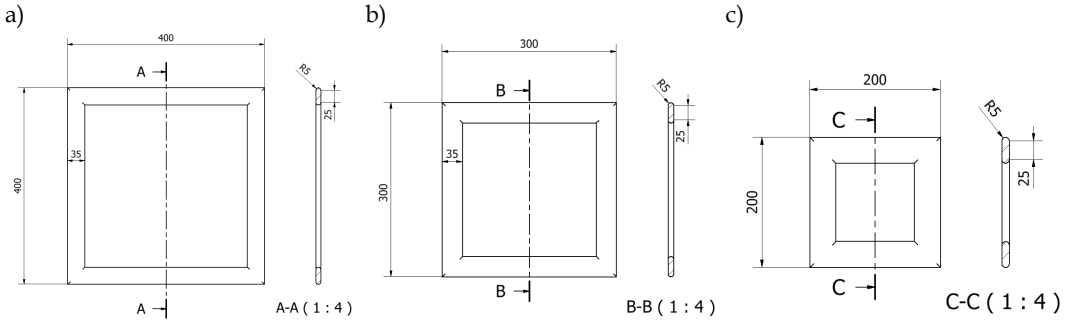

Figure 3.30: Technical drawings detailing three sorts of printed layers utilized in the numerical simulations.

Figure 3.31: An illustration of the column that was printed by İSTON Inc. and its simulated geometry to be utilized in buildability analyses.

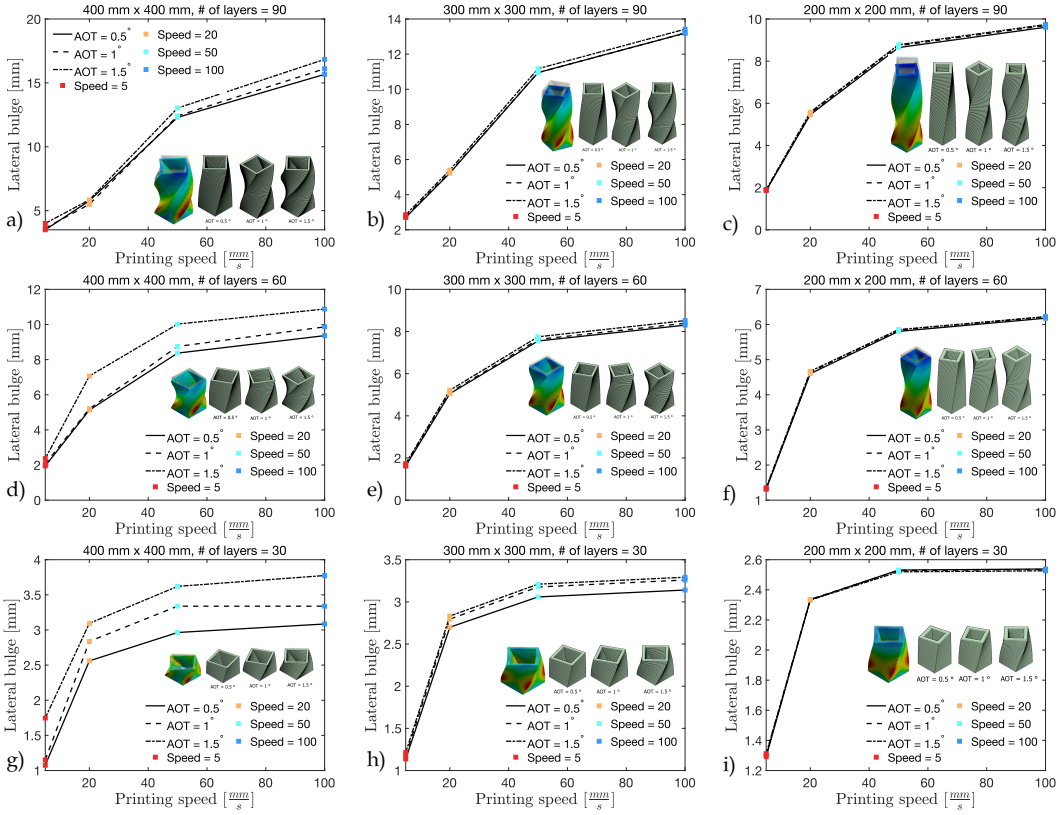

Figure 3.32: Simulation results of lateral deformations for a column printed in the İSTON Inc. in Istanbul.

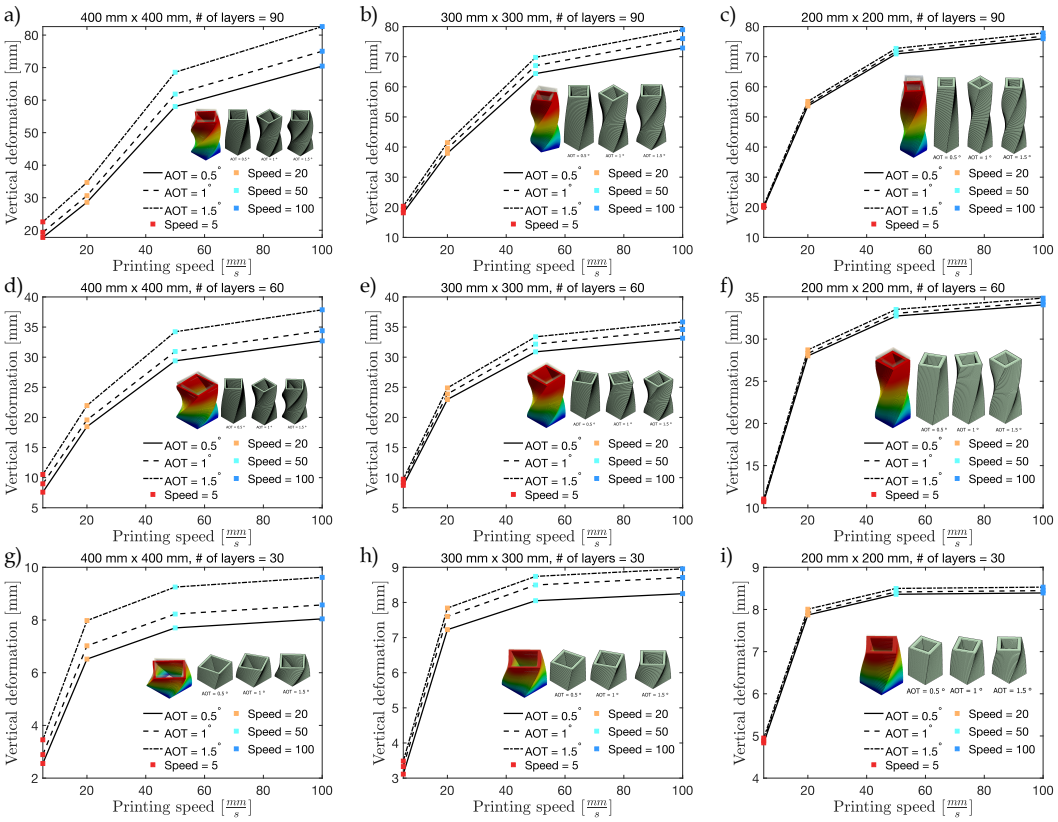

Figure 3.33: Simulation results of vertical deformations for a column printed in the İSTON Inc. in Istanbul.

CHAPTER 4

CONCLUDING REMARKS

This research intended to develop a mathematical model for the phenomenon of buildability in 3D printed concrete structures. For this reason, the curing and hydration phenomena in early-age (i.e. fresh) concrete were mathematically treated, to eventually yield age-dependent frameworks for modulus of elasticity and Poisson's ratio, in terms of the degree of hydration and degree of cure parameters. On the basis of experimentally observed stress-strain behaviors in early-age specimens, these parameters were submitted to plasticity-damage models for concrete, for which three cases were considered.

As the first model, a thermodynamically consistent variant of the microplane framework was used as the basis of the plasticity damage model in the small-strain setting. The volumetric-deviatoric decomposition of the strain tensor on each microplane was utilized for this objective. The DP yield criterion was selected as the plasticity framework in formulation of the plane-level constitutive relations. A monotonically increasing damage function, driven by the history of thermodynamically consistent damage energy release rate, was proposed as the damage definition. Using the available data from the scientific literature, the model was validated for tensile and compressive stress situations, and a good agreement was found. A CDM-based plasticity damage model with empirical definitions for plasticity and damage (computationally efficient, though not totally consistent thermodynamically) and a gradient-enhanced version of the DP plasticity damage model were adopted from the literature as the second and third models, respectively. In addition, a series of unconfined uni-axial compression experiments were performed to evaluate the performance of proposed mathematical frameworks and parameter tuning. Additionally, the investigated mi-

croplane plasticity damage model was further tested against a data set from the literature. After linking the curing kinetics with each of the plasticity damage models, the pertinent model parameters for each model were optimized to improve the fitting performance. In addition, the fitted model-specific parameters were expressed in terms of the degree of cure parameter, completing the framework for a time-dependent scheme for the stress-strain behavior of early-age concrete to be used in the numerical simulations.

The gradient-enhanced microplane plasticity damage model was used as the basis for the numerical simulations. Initially, a framework was proposed to link the printing process, and its related parameters (such as printing speed, cross-sectional geometry, layer thickness, nozzle tip dimension, and number of printed layers), to the mentioned mathematical scope for stress-strain behavior of early-age concrete. Within this scope, simulations were repeated for three common cross-sectional geometries, for which the self-weight-induced deformations were obtained in the principal directions, and the major effects of the printing parameters were emphasized. Last but not least, numerical simulations of a 3D printed geometry (conducted by Iston Inc.) were performed, and the implications of various factors were highlighted.

Additional investigation into the topics covered in this paper could be conducted in subsequent research projects, potentially focusing on the areas outlined below:

1. Extending the examined microplane DP plasticity damage framework for the large-strain situation so that it accurately accommodates a wider range of displacements.

2. Evaluation of the model utilizing alternative plasticity criteria for pressure-dependent materials.

3. A mathematical model that accounts for improper inter-layer adhesion during the printing process (possibly a damage or defect parameter).

4. Comparing the model's predictions to actual printed specimens (which was not possible at the time of preparing this work, due to the lack of experimental apparatus).

REFERENCES

[1] R. J. Wolfs, F. P. Bos, and T. A. Salet, "Early age mechanical behaviour of 3D printed concrete: Numerical modelling and experimental testing," *Cement and Concrete Research*, vol. 106, pp. 103–116, apr 2018.

[2] I. Zreid and M. Kaliske, "A gradient enhanced plasticity–damage microplane model for concrete," *Computational Mechanics*, vol. 62, no. 5, pp. 1239–1257, 2018.

[3] I. Zreid and M. Kaliske, "Regularization of microplane damage models using an implicit gradient enhancement," *International Journal of Solids and Structures*, vol. 51, pp. 3480–3489, oct 2014.

[4] S. El-Sayegh, ·. L. Romdhane, and ·. S. Manjikian, "A critical review of 3D printing in construction: benefits, challenges, and risks A Critical Review of 3D Printing in Construction," *Archives of Civil and Mechanical Engineering*, vol. 20, p. 3, 2020.

[5] A. U. Rehman and J.-H. Kim, "3d concrete printing: A systematic review of rheology, mix designs, mechanical, microstructural, and durability characteristics," *Materials*, vol. 14, no. 14, 2021.

[6] M. R. M. Saade, A. Yahia, and B. Amor, "How has lca been applied to 3d printing? a systematic literature review and recommendations for future studies," *Journal of Cleaner Production*, vol. 244, p. 118803, 2020.

[7] I. Agustí-Juan, F. Müller, N. Hack, T. Wangler, and G. Habert, "Potential benefits of digital fabrication for complex structures: Environmental assessment of a robotically fabricated concrete wall," *Journal of Cleaner Production*, vol. 154, pp. 330–340, jun 2017.

[8] G. De Schutter, K. Lesage, V. Mechtcherine, V. N. Nerella, G. Habert, and I. Agusti-Juan, "Vision of 3D printing with concrete — Technical, economic and

environmental potentials," *Cement and Concrete Research*, vol. 112, pp. 25–36, oct 2018.

[9] S. Liu, B. Lu, H. Li, Z. Pan, J. Jiang, and S. Qian, "A comparative study on environmental performance of 3D printing and conventional casting of concrete products with industrial wastes," *Chemosphere*, vol. 298, p. 134310, jul 2022.

[10] I. Muñoz, J. Alonso-Madrid, M. Menéndez-Muñiz, M. Uhart, J. Canou, C. Martin, M. Fabritius, L. Calvo, L. Poudelet, R. Cardona, H. Lombois-Burger, N. Vlasopoulos, C. Bouyssou, J. Dirrenberger, A. Papacharalampopoulos, and P. Stavropoulos, "Life cycle assessment of integrated additive-subtractive concrete 3D printing," *The International Journal of Advanced Manufacturing Technology*, vol. 112, pp. 2149–2159, 2021.

[11] S. Lim, R. Buswell, T. Le, S. Austin, A. Gibb, and T. Thorpe, "Developments in construction-scale additive manufacturing processes," *Automation in Construction*, vol. 21, pp. 262–268, 2012.

[12] B. Zareiyan and B. Khoshnevis, "Effects of interlocking on interlayer adhesion and strength of structures in 3d printing of concrete," *Automation in Construction*, vol. 83, pp. 212–221, 2017.

[13] D. Lowke, E. Dini, A. Perrot, D. Weger, C. Gehlen, and B. Dillenburger, "Particle-bed 3d printing in concrete construction – possibilities and challenges," *Cement and Concrete Research*, vol. 112, pp. 50–65, 2018. SI : Digital concrete 2018.

[14] X. Zhang, M. Li, J. H. Lim, Y. Weng, Y. W. D. Tay, H. Pham, and Q.-C. Pham, "Large-scale 3d printing by a team of mobile robots," *Automation in Construction*, vol. 95, pp. 98–106, 2018.

[15] P. Wu, J. Wang, and X. Wang, "A critical review of the use of 3-d printing in the construction industry," *Automation in Construction*, vol. 68, pp. 21–31, 2016.

[16] G. D. Schutter and L. Taerwe, "Degree of hydration-based description of mechanical properties of early age concrete," *Materials and Structures*, vol. 29, pp. 335–344, 1996.

[17] Feng-Li2018, "Softened Damage-Plasticity Model for Analysis of Cracked Reinforced Concrete Structures," *Journal of Structural Engineering*, vol. 144, no. 6, p. 04018044, 2018.

[18] J. Pegna, "Exploratory investigation of solid freeform construction," *Automation in Construction*, vol. 5, pp. 427–437, feb 1997.

[19] S. A. Khan, M. Koç, and S. G. Al-Ghamdi, "Sustainability assessment, potentials and challenges of 3d printed concrete structures: A systematic review for built environmental applications," *Journal of Cleaner Production*, vol. 303, p. 127027, 2021.

[20] D. Dey, D. Srinivas, B. Panda, P. Suraneni, and T. Sitharam, "Use of industrial waste materials for 3d printing of sustainable concrete: A review," *Journal of Cleaner Production*, vol. 340, p. 130749, 2022.

[21] M. K. Mohan, A. Rahul, B. van Dam, T. Zeidan, G. De Schutter, and K. Van Tittelboom, "Performance criteria, environmental impact and cost assessment for 3d printable concrete mixtures," *Resources, Conservation and Recycling*, vol. 181, p. 106255, 2022.

[22] S. Muthukrishnan, S. Ramakrishnan, and J. Sanjayan, "Effect of alkali reactions on the rheology of one-part 3d printable geopolymer concrete," *Cement and Concrete Composites*, vol. 116, p. 103899, 2021.

[23] M. Valipour, M. Yekkalar, M. Shekarchi, and S. Panahi, "Environmental assessment of green concrete containing natural zeolite on the global warming index in marine environments," *Journal of Cleaner Production*, vol. 65, pp. 418–423, 2014.

[24] G. Bai, L. Wang, G. Ma, J. Sanjayan, and M. Bai, "3d printing eco-friendly concrete containing under-utilised and waste solids as aggregates," *Cement and Concrete Composites*, vol. 120, p. 104037, 2021.

[25] A. U. Rehman, S.-M. Lee, and J.-H. Kim, "Use of municipal solid waste incineration ash in 3d printable concrete," *Process Safety and Environmental Protection*, vol. 142, pp. 219–228, 2020.

[26] M. Mohammad, E. Masad, and S. G. Al-Ghamdi, "3d concrete printing sustainability: A comparative life cycle assessment of four construction method scenarios," *Buildings*, vol. 10, no. 12, 2020.

[27] Y. Han, Z. Yang, T. Ding, and J. Xiao, "Environmental and economic assessment on 3D printed buildings with recycled concrete," *Journal of Cleaner Production*, vol. 278, p. 123884, jan 2021.

[28] C. Knoeri, E. Sanyé-Mengual, and H. J. Althaus, "Comparative LCA of recycled and conventional concrete for structural applications," *International Journal of Life Cycle Assessment*, vol. 18, pp. 909–918, jun 2013.

[29] S. Marinković, V. Radonjanin, M. Malešev, and I. Ignjatović, "Comparative environmental assessment of natural and recycled aggregate concrete," *Waste Management*, vol. 30, pp. 2255–2264, nov 2010.

[30] J. Turk, Z. Cotič, A. Mladenovič, and A. Šajna, "Environmental evaluation of green concretes versus conventional concrete by means of LCA," *Waste Management*, vol. 45, pp. 194–205, nov 2015.

[31] Y. Weng, M. Li, S. Ruan, T. N. Wong, M. J. Tan, K. L. Ow Yeong, and S. Qian, "Comparative economic, environmental and productivity assessment of a concrete bathroom unit fabricated through 3D printing and a precast approach," *Journal of Cleaner Production*, vol. 261, p. 121245, jul 2020.

[32] J. Faludi, C. Bayley, S. Bhogal, and M. Iribarne, "Comparing environmental impacts of additive manufacturing vs. traditional machining via life-cycle assessment," *Rapid Prototyping Journal*, vol. 21, pp. 14–33, 01 2015.

[33] F. Cerdas, M. Juraschek, S. Thiede, and C. Herrmann, "Life Cycle Assessment of 3D Printed Products in a Distributed Manufacturing System," *Journal of Industrial Ecology*, vol. 21, pp. S80–S93, nov 2017.

[34] N. Labonnote and P. Rüther, "Additive manufacturing: an opportunity for functional and sustainable constructions," in *Challenges for Technology Innovation: An Agenda for the Future*, pp. 201–205, CRC Press, 2017.

[35] N. Labonnote, A. Rønnquist, B. Manum, and P. Rüther, "Additive construction: State-of-the-art, challenges and opportunities," *Automation in Construction*, vol. 72, pp. 347–366, dec 2016.

[36] I. Agustí-Juan and G. Habert, "Environmental design guidelines for digital fabrication," *Journal of Cleaner Production*, vol. 142, pp. 2780–2791, jan 2017.

[37] K. Kuzmenko, A. Feraille, O. Baverel, and N. Roussel, "Environmental Impacts of 6-Axes Robotic Arm for 3D Concrete Printing," *RILEM Bookseries*, vol. 28, pp. 1023–1030, 2020.

[38] B. Khoshnevis, D. Hwang, K.-T. Yao, and Z. Yeh, "Mega-scale fabrication by contour crafting," *International Journal of Industrial and Systems Engineering*, vol. 1, no. 3, pp. 301–320, 2006.

[39] C. Gosselin, R. Duballet, P. Roux, N. Gaudillière, J. Dirrenberger, and P. Morel, "Large-scale 3d printing of ultra-high performance concrete – a new processing route for architects and builders," *Materials Design*, vol. 100, pp. 102–109, 2016.

[40] O. Davtalab, A. Kazemian, and B. Khoshnevis, "Perspectives on a bim-integrated software platform for robotic construction through contour crafting," *Automation in Construction*, vol. 89, pp. 13–23, 2018.

[41] J. Ingaglio, J. Fox, C. J. Naito, and P. Bocchini, "Material characteristics of binder jet 3d printed hydrated csa cement with the addition of fine aggregates," *Construction and Building Materials*, vol. 206, pp. 494–503, 2019.

[42] S. H. Ghaffar, J. Corker, and M. Fan, "Additive manufacturing technology and its implementation in construction as an eco-innovative solution," *Automation in Construction*, vol. 93, pp. 1–11, 2018.

[43] T. Wangler, N. Roussel, F. P. Bos, T. A. Salet, and R. J. Flatt, "Digital Concrete: A Review," *Cement and Concrete Research*, vol. 123, sep 2019.

[44] I. Ivanova, E. Ivaniuk, S. Bisetti, V. N. Nerella, and V. Mechtcherine, "Comparison between methods for indirect assessment of buildability in fresh 3D printed mortar and concrete," *Cement and Concrete Research*, vol. 156, jun 2022.

[45] S. Hou, Z. Duan, J. Xiao, and J. Ye, "A review of 3D printed concrete: Performance requirements, testing measurements and mix design," *Construction and Building Materials*, vol. 273, mar 2021.

[46] T. T. Le, S. A. Austin, S. Lim, R. A. Buswell, A. G. Gibb, and T. Thorpe, "Mix design and fresh properties for high-performance printing concrete," *Materials and Structures/Materiaux et Constructions*, vol. 45, pp. 1221–1232, aug 2012.

[47] K. El Cheikh, S. Rémond, N. Khalil, and G. Aouad, "Numerical and experimental studies of aggregate blocking in mortar extrusion," *Construction and Building Materials*, vol. 145, pp. 452–463, aug 2017.

[48] Z. Li, M. Hojati, Z. Wu, J. Piasente, N. Ashrafi, J. P. Duarte, S. Nazarian, S. G. Bilén, A. M. Memari, and A. Radlińska, "Fresh and Hardened Properties of Extrusion-Based 3D-Printed Cementitious Materials: A Review," *Sustainability 2020, Vol. 12, Page 5628*, vol. 12, p. 5628, jul 2020.

[49] V. Mechtcherine, F. P. Bos, A. Perrot, W. R. da Silva, V. N. Nerella, S. Fataei, R. J. Wolfs, M. Sonebi, and N. Roussel, "Extrusion-based additive manufacturing with cement-based materials – Production steps, processes, and their underlying physics: A review," *Cement and Concrete Research*, vol. 132, jun 2020.

[50] A. Kazemian, X. Yuan, E. Cochran, and B. Khoshnevis, "Cementitious materials for construction-scale 3D printing: Laboratory testing of fresh printing mixture," *Construction and Building Materials*, vol. 145, pp. 639–647, aug 2017.

[51] H. Liu, T. Ding, J. Xiao, and V. Mechtcherine, "Buildability prediction of 3D–printed concrete at early-ages: A numerical study with Drucker–Prager model," *Additive Manufacturing*, vol. 55, p. 102821, Jul 2022.

[52] Z. Chang, Y. Xu, Y. Chen, Y. Gan, E. Schlangen, and B. Šavija, "A discrete lattice model for assessment of buildability performance of 3D-printed concrete," *Computer-Aided Civil and Infrastructure Engineering*, vol. 36, pp. 638–655, may 2021.

[53] N. Roussel, "A thixotropy model for fresh fluid concretes: Theory, validation and applications," *Cement and Concrete Research*, vol. 36, pp. 1797–1806, oct 2006.

[54] A. Perrot, T. Lecompte, P. Estellé, and S. Amziane, "Structural build-up of rigid fiber reinforced cement-based materials," *Materials and Structures/Materiaux et Constructions*, vol. 46, pp. 1561–1568, sep 2013.

[55] A. Perrot, D. Rangeard, and A. Pierre, "Structural built-up of cement-based materials used for 3D-printing extrusion techniques," *Materials and Structures/-Materiaux et Constructions*, vol. 49, pp. 1213–1220, apr 2016.

[56] A. S. Suiker, "Mechanical performance of wall structures in 3D printing processes: Theory, design tools and experiments," *International Journal of Mechanical Sciences*, vol. 137, pp. 145–170, mar 2018.

[57] L. Yuanming, G. Zhihua, Z. Shujuan, and C. Xiaoxiao, "Stress-Strain Relationships and Nonlinear Mohr Strength Criteria of Frozen Sandy Clay," *Soils and Foundations*, vol. 50, pp. 45–53, feb 2010.

[58] M. Smith, *ABAQUS/Standard User's Manual, Version 6.9*. United States: Dassault Systèmes Simulia Corp, 2009.

[59] B. Panda, J. H. Lim, and M. J. Tan, "Mechanical properties and deformation behaviour of early age concrete in the context of digital construction," *Composites Part B: Engineering*, vol. 165, pp. 563–571, may 2019.

[60] L. Casagrande, L. Esposito, C. Menna, D. Asprone, and F. Auricchio, "Effect of testing procedures on buildability properties of 3D-printable concrete," *Construction and Building Materials*, vol. 245, p. 118286, jun 2020.

[61] R. J. Wolfs, F. P. Bos, and T. A. Salet, "Triaxial compression testing on early age concrete for numerical analysis of 3D concrete printing," *Cement and Concrete Composites*, vol. 104, p. 103344, nov 2019.

[62] L. Reiter, *Structural Build-up for Digital Fabrication with Concrete - Materials, Methods and Processes*. Doctoral thesis, ETH Zurich, Zurich, 2019-07.

[63] F. P. Bos, P. J. Kruger, S. S. Lucas, and G. P. van Zijl, "Juxtaposing fresh material characterisation methods for buildability assessment of 3D printable cementitious mortars," *Cement and Concrete Composites*, vol. 120, jul 2021.

[64] R. J. Wolfs, F. P. Bos, and T. A. Salet, "Correlation between destructive compression tests and non-destructive ultrasonic measurements on early age 3D printed concrete," *Construction and Building Materials*, vol. 181, pp. 447–454, aug 2018.

[65] Z. P. Bažant and B. H. Oh, "Microplane model for fracture analysis of concrete structures," tech. rep., Northwestern Univ Evanston Il Technological Inst, 1983.

[66] I. Carol, M. Jirásek, and Z. Bažant, "A thermodynamically consistent approach to microplane theory. Part I. Free energy and consistent microplane stresses," *International Journal of Solids and Structures*, vol. 38, pp. 2921–2931, apr 2001.

[67] P. C. Prat and Z. P. Bažant, "Microplane Model for Triaxial Deformation of Saturated Cohesive Soils," *Journal of Geotechnical Engineering*, vol. 117, pp. 891–912, jun 1991.

[68] M. Brocca, L. C. Brinson, and Z. P. Bažant, "Three-dimensional constitutive model for shape memory alloys based on microplane model," *Journal of the Mechanics and Physics of Solids*, vol. 50, pp. 1051–1077, may 2002.

[69] X. Chen and Z. P. Bažant, "Microplane damage model for jointed rock masses," *International Journal for Numerical and Analytical Methods in Geomechanics*, vol. 38, pp. 1431–1452, oct 2014.

[70] E. Kuhl, P. Steinmann, and I. Carol, "A thermodynamically consistent approach to microplane theory. Part II. Dissipation and inelastic constitutive modeling," *International Journal of Solids and Structures*, vol. 38, no. 17, pp. 2933–2952, 2001.

[71] E. Kuhl and E. Ramm, "Microplane modeling of cohesive frictional materials," *European Journal of Mechanics - A/Solids*, pp. 121–143, 2000.

[72] M. Leukart and E. Ramm, "Identification and Interpretation of Microplane Material Laws," *Journal of Engineering Mechanics*, vol. 132, pp. 295–305, mar 2006.

[73] I. Zreid and M. Kaliske, "An implicit gradient formulation for microplane Drucker-Prager plasticity," *International Journal of Plasticity*, vol. 83, pp. 252–272, 2016.

[74] T. Berger and ·. M. Kaliske, "A thermo-mechanical material model for rubber curing and tire manufacturing simulation," *Computational Mechanics*, vol. 66, pp. 513–535, 2020.

[75] H. Dal, C. Zopf, and M. Kaliske, "Micro-sphere based viscoplastic constitutive model for uncured green rubber," *International Journal of Solids and Structures*, vol. 132-133, pp. 201–217, feb 2018.

[76] Z. P. Bažant, F. Asce, B. H. Oh, and A. M. Asce, "Microplane Model for Progressive Fracture of Concrete and Rock," *Journal of Engineering Mechanics*, vol. 111, pp. 559–582, apr 1985.

[77] B. P. Zdenek Bažant, P. C. Prat, and S. Member, "Microplane Model for BrittlePlastic Material: I. Theory," *Journal of Engineering Mechanics*, vol. 114, pp. 1672–1688, oct 1988.

[78] P. Bažant and B. H. Oh, "Efficient Numerical Integration on the Surface of a Sphere," *ZAMM - Journal of Applied Mathematics and Mechanics / Zeitschrift für Angewandte Mathematik und Mechanik*, vol. 66, pp. 37–49, jan 1986.

[79] J. C. Simo and J. W. Ju, "Strain- and stress-based continuum damage models—I. Formulation," *International Journal of Solids and Structures*, vol. 23, pp. 821–840, jan 1987.

[80] J. Y. Wu, J. Li, and R. Faria, "An energy release rate-based plastic-damage model for concrete," *International Journal of Solids and Structures*, vol. 43, pp. 583–612, feb 2006.

[81] R. Faria, J. Oliver, and M. Cervera, "A strain-based plastic viscous-damage model for massive concrete structures," *International Journal of Solids and Structures*, vol. 35, no. 14, pp. 1533–1558, 1998.

[82] J. W. Ju, "On energy-based coupled elastoplastic damage theories: Constitutive modeling and computational aspects," *International Journal of Solids and Structures*, vol. 25, no. 7, pp. 803–833, 1989.

[83] J. Li, D.-C. Feng, X. Gao, and Y. Zhang, "Stochastic nonlinear behavior of reinforced concrete frames. i: Experimental investigation," *Journal of Structural Engineering*, vol. 142, no. 3, p. 04015162, 2016.

[84] L. E. Schwer and Y. D. Murray, "A three-invariant smooth cap model with mixed hardening," *International Journal for Numerical and Analytical Methods in Geomechanics*, vol. 18, pp. 657–688, oct 1994.

[85] J. Lee and G. L. Fenves, "Plastic-damage model for cyclic loading of concrete structures," *Journal of Engineering Mechanics*, vol. 124, no. 8, pp. 892–900, 1998.

[86] L. Hien Poh and S. Swaddiwudhipong, "Over-nonlocal gradient enhanced plastic-damage model for concrete," *International Journal of Solids and Structures*, vol. 46, pp. 4369–4378, dec 2009.

[87] P. Grassl and M. Jirásek, "Plastic model with non-local damage applied to concrete," *International Journal for Numerical and Analytical Methods in Geomechanics*, vol. 30, pp. 71–90, jan 2006.

[88] H. Jiang and J. Zhao, "Calibration of the continuous surface cap model for concrete," *Finite Elements in Analysis and Design*, vol. 97, pp. 1–19, May 2015.

[89] W. Liao, X. Sun, A. Kumar, H. Sun, and H. Ma, "Hydration of binary portland cement blends containing silica fume: A decoupling method to estimate degrees of hydration and pozzolanic reaction," *Frontiers in Materials*, vol. 6, 2019.

APPENDIX A

WEIGHTS AND INTEGRATION POINTS IN MICROPLANE THEORY

Table A.1: Weights and integration point coordinates on a unit sphere, according to I. Zreid & M. Kaliske [3].

$Integration\,point\,No.$	x	y	z	$\omega^{n_{mic}}$
1	0.187592474085	0.000000000000	0.982246946377	0.1190476190478
2	0.794654472292	−0.525731112119	0.303530999103	0.1190476190478
3	0.794654472292	0.525731112119	0.303530999103	0.1190476190478
4	0.187592474085	−0.850650808352	−0.491123473188	0.1190476190478
5	0.794654472292	0.000000000000	−0.607061998207	0.1190476190478
6	0.187592474085	0.850650808352	−0.491123473188	0.1190476190478
7	0.577350269190	−0.309016994375	0.755761314076	0.1523809523808
8	0.577350269190	0.309016994375	0.755761314076	0.1523809523808
9	0.934172358963	0.000000000000	0.356822089773	0.1523809523808
10	0.577350269190	−0.809016994375	−0.110264089708	0.1523809523808
11	0.934172358963	−0.309016994375	−0.178411044887	0.1523809523808
12	0.934172358963	0.309016994375	−0.178411044887	0.1523809523808
13	0.577350269190	0.809016994375	−0.110264089708	0.1523809523808
14	0.577350269190	−0.500000000000	−0.645497224368	0.1523809523808
15	0.577350269190	0.500000000000	−0.645497224368	0.1523809523808
16	0.356822089773	−0.809016994375	0.467086179481	0.1523809523808
17	0.356822089773	0.000000000000	−0.934172358963	0.1523809523808
18	0.356822089773	0.809016994375	0.467086179481	0.1523809523808
19	0.000000000000	−0.500000000000	0.866025403784	0.1523809523808
20	0.000000000000	−0.500000000000	−0.866025403784	0.1523809523808
21	0.000000000000	−1.000000000000	0.000000000000	0.1523809523808